OpenFOAM® and μPIV-aided femtosecond irradiation-based etching optimization for applications in microfluidics

Hugo J. da Nóbrega
Mestrado Integrado em Engenharia Física
Departamento de Física e Astronomia
2019

Orientador
Prof. Dr. Paulo Vicente da Silva Marques, INESC-TEC, Faculdade de Ciências da Universidade do Porto

Coorientadores
Dr. Francisco José Galindo-Rosales, CEFT, Faculdade de Engenharia da Universidade do Porto
Prof. Dr. Manuel António Moreira Alves, CEFT, Faculdade de Engenharia da Universidade do Porto

U.PORTO

FACULDADE DE CIÊNCIAS
UNIVERSIDADE DO PORTO

Todas as correções determinadas pelo júri, e só essas, foram efetuadas.

O Presidente do Júri,

Porto, _____/_____/_____

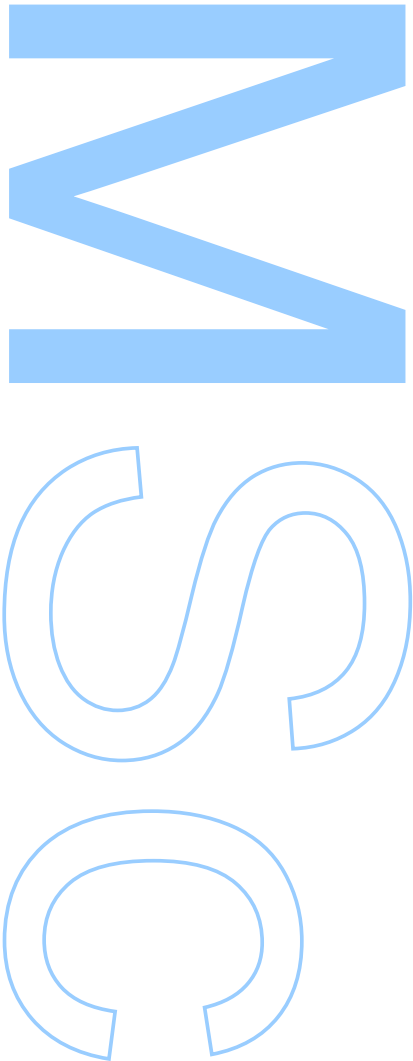

Universidade do Porto

Masters Thesis

OpenFOAM® and μPIV-aided femtosecond irradiation-based etching optimization for applications in microfluidics

Author:
Hugo da Nóbrega

Supervisor:
Paulo Marques

Co-supervisors:
Francisco Galindo-Rosales
Manuel Alves

A thesis submitted in fulfilment of the requirements for the degree of MSc. Engineering Physics

at the

Faculdade de Ciências da Universidade do Porto
Departamento de Física e Astronomia

December 5, 2019

"Clayton Harding: [Meeting with Sidney for the first time in Clayton's corporate office] You think you've arrived, don't you? Hate to break it to you, but you're only in the first room. In about a year, maybe longer, you'll discover a secret doorway at the back of the first room that leads to the second. And in time, if you're lucky, you'll discover another doorway in the back of the second room that leads to the third. There are seven rooms altogether. You're in the first. I'm in the seventh. Don't you forget it.

Sidney Young: [nonchalantly] Can I use the bathroom in the seventh? Because the one in the first really smells. "

Transcript of the film 'How to lose friends and alienate people'

Acknowledgements

The direct contributions to this thesis were immense. The first thank you must go to all my supervisors, Prof. Dr. Paulo Marques, Dr. Francisco Galindo-Rosales, and Prof. Dr. Manuel Alves. It was a great pleasure working and discussing with all of them, and I feel that I have received a lot of knowledge while also contacting with an equal amount of new perspectives.

At FCUP, I would like to thank João Maia, Vitor Amorim and Duarte Viveiros for creating such a nice work environment, especially João, for all the patience and valuable insights. Also thanks to Filipe Silva for all advices.

At FEUP, I thank Dr. José Daniel Araújo for all the help with cfMesh, and Dr. Samir Sadek for all the μPIV tips and tricks.

The present work is the culmination of one intense roller-coaster, and it was very nice to have some company while riding it. So, thank you to all guys (and the demi-girl) in the 2014/15 class, who have been through all this with me.

Last, but not least, I would like to thank a very inspiring bird, which carried me on its dynamic wings, and to my parents, for literally everything, everytime, everywhere.

Oh, and thank you, good old Lenovo X220, to whom I am often inconsiderate enough to insult him, reboot him forcefully, and other sorts of abuse due to his non-compliance with my excessive multitasking and aggressive programming.

This project was developed as part of a BIC (Bolsa de Iniciação Científica) within the project 'Rheologically optimized 2D-material-based inks - RheoOptimized2DInks', supported by FCT/MCTES through national funds (PIDDAC) and by FEDER through COMPETE2020-POCI (reference POCI-01-0145-FEDER-030765), to which I thank.

UNIVERSIDADE DO PORTO

Abstract

Faculdade de Ciências da Universidade do Porto
Departamento de Física e Astronomia

MSc. Engineering Physics

OpenFOAM® and μPIV-aided femtosecond irradiation-based etching optimization for applications in microfluidics

by Hugo da Nóbrega

Non-linear absorption processes triggered by ultrafast, highly focused femtosecond laser radiation are on the basis of structural and chemical changes in fused silica, which are now widely studied and categorized according to the energy at the focal volume. Under certain exposure energy regimes it is observed that wet-etching anisotropy is induced by the ultrafast laser exposure, leading to a much faster fused silica wet-etching rate at the focal volume when compared to unexposed pristine silica. Therefore, the combination of exposure to ultrafast radiation with chemical etching has resulted in a systematic approach for monolithic micro-fabrication of hollow structures, named femtosecond laser-assisted etching, encompassing unique remarkable features such as three-dimensionality and sub-micrometric resolution.

In this work, it is aimed to characterize the quality of the fabrication with a laser writing system, in terms of resolution in all directions after etching, final surface roughness for in-depth fabrication, and further possibilities of application of the aforementioned technique in microfluidics. Specifically, microfluidic channels completely integrated in a fused silica substrate are fabricated, carrying along the possibility of testing at higher pressures without deforming and/or damaging the device, as happens in polydimethylsiloxane-based microchannels, and of fabrication without a controlled environment required by traditional clean-room soft lithography methods.

Numerical simulations using OpenFOAM® assist the design process, both in asserting the influence of fabrication parameters in several designs - by comparison with micro-particle image velocimetry results, as in similar work sequences but with full polydimethylsiloxane fabrication, and with analytic solutions whenever they are known -, and in the determination of optimal geometric parameters to use in conjunction with their fabrication counterparts, aiming for a microfluidic lab-on-a-chip.

UNIVERSIDADE DO PORTO

Resumo

Faculdade de Ciências da Universidade do Porto
Departamento de Física e Astronomia

Mestrado Integrado em Engenharia Física

Otimização de etching seletivo induzido por laser de femtosegundo assistida por OpenFOAM® e μPIV para aplicações em microfluídica

por Hugo da Nóbrega

Os processos de absorção não-linear desencadeados por radiação laser de período ultra-curto, altamente focada, têm a sua base em mudanças estruturais e químicas na sílica fundida, atualmente amplamente estudadas e categorizadas de acordo com a energia no volume focal. Sob certos regimes de energia de exposição, observa-se a anisotropia fotoinduzida em processos de ataque químico, advinda de uma taxa muito mais rápida de ataque de sílica fundida quando comparada à da sílica pura não exposta. Em face do exposto, a combinação da exposição à radiação ultra-rápida com o ataque químico resulta numa abordagem sistemática para a microfabricação monolítica de estruturas lacunares, denominada *etching* assistido por laser de femtosegundo, que engloba aspetos notáveis e distintivos, tais como tridimensionalidade e resolução sub-micrométrica.

Neste trabalho, é caracterizada a qualidade da fabricação com um sistema para exposição controlada de radiação ultra-rápida, em termos de resolução em todas as direcções após a escrita, rugosidade da superfície final para a fabricação em profundidade e demais possibilidades de aplicação da técnica descrita em microfluídica. Especificamente, são fabricados canais microfluídicos completamente integrados num substrato de sílica fundida, possibilitando o teste em pressões mais altas sem deformar e/ou danificar o dispositivo, como acontece nos microcanais baseados em polidimetilsiloxano, e a fabricação sem o requerimento de um ambiente controlado exigido pelos métodos tradicionais de litografia em sala limpa.

Simulações numéricas usando OpenFOAM® auxiliam o processo de escrita, tanto na asserção da influência dos parâmetros de fabricação em vários designs - por comparação com resultados provenientes de velocimetria de imagem de micropartículas, tal como em sequências de trabalho similares embora baseadas totalmente em polidimetilsiloxano, e com soluções analíticas, quando conhecidas -, como na determinação de parâmetros geométricos ótimos para integração com os de escrita, tendo em vista a obtenção de um *lab-on-a-chip* microfluídico.

Contents

Acknowledgements v

Abstract vii

Resumo ix

Contents xi

List of Figures xv

Nomenclature xx

Notation and Conventions xxv

1 Introduction 1
- 1.1 Microfluidics, why and how? . . . 1
  - 1.1.1 'Traditional' processes in microchannel fabrication . . . 3
    - 1.1.1.1 Photolithography and soft lithography . . . 3
    - 1.1.1.2 Joining glass and PDMS: bonding processes . . . 5
  - 1.1.2 Microfluidic fabrication by laser techniques . . . 6
    - 1.1.2.1 The advent of non-linear ultrafast optics . . . 6
    - 1.1.2.2 Non-linear photon absorption . . . 6
    - 1.1.2.3 Femtosecond Laser Assisted Etching . . . 7
    - 1.1.2.4 Water Assisted Femtosecond Laser Drilling . . . 13
- 1.2 Objectives and contributions of this work . . . 15
- 1.3 Contents and structure of the present thesis . . . 15

2 Materials and Methods 19
- 2.1 Experimental realization of FLAE . . . 19
  - 2.1.1 Femtosecond laser irradiation . . . 19
    - 2.1.1.1 Experimental setup . . . 19
    - 2.1.1.2 Experimental method . . . 23
  - 2.1.2 Chemical etching with HF . . . 24
  - 2.1.3 Chemical etching with KOH . . . 25

2.1.4 Substrate polishing . . . 26
2.2 A crash course on OpenFOAM® . . . 29
2.2.1 The finite volume method . . . 29
2.2.2 Preprocessing: the art of meshing . . . 30
2.2.3 A microfluidic problem solved with OpenFOAM® . . . 31
2.2.4 Post processing: simulation results . . . 32
2.3 Experimental realization of microparticle image velocimetry . . . 34
2.3.1 General considerations . . . 35
2.3.2 Experimental method . . . 38

3 The microfluidic channel 41
3.1 Analytic solution . . . 41
3.1.1 Perturbation methods of the channel's cross section . . . 43
3.2 Solution obtained with OpenFOAM® . . . 44
3.2.1 Microfluidic channel with square cross section . . . 44
3.2.2 Incorporation of roughness . . . 45
3.3 Description of the fabrication method . . . 46
3.4 Study of the graded meshing scheme . . . 48
3.5 Study of the uniform meshing scheme . . . 52
3.5.1 Etching from the side optimization . . . 52
3.5.2 Optimization of etching with access ports . . . 56
3.6 Fabrication of channels for tests . . . 60
3.6.1 Effect of the interrogation area in μPIV quality . . . 61
3.7 Conclusions . . . 62

4 Testing the limits of FLAE: the OSCER device 65
4.1 OSCER device description and fabrication . . . 65
4.2 Algorithm for the OSCER device fabrication with FLAE . . . 66
4.3 Implementation of complex trajectories in SCA . . . 69
4.4 Fabrication with SCA hatching and slicing . . . 71
4.5 Fabrications with different meshing schemes . . . 71
4.6 Effect of thermal annealing . . . 75
4.7 OSCER fabrication with and without access ports . . . 77
4.8 Conclusions . . . 84

5 Concluding remarks and future work 87

A The microfluidic contraction: from simulations to fabrication 91
A.1 Case structuring in OpenFOAM® . . . 91
A.2 Preprocessing: generating the mesh and setting the simulation . . . 92
A.2.0.1 Determination of the mesh parameter expansion ratio . . . 94
A.2.0.2 Anatomy of a `blockMeshDict` file . . . 94
A.2.0.3 Setting the `controlDict` file . . . 99
A.3 Fabrication and characterization of a contraction . . . 100

B Computation of graded meshes using `blockMeshDict` 101
B.1 Determination of the ratio of a geometric progression 101
B.2 Determination of the number of cells 104
B.3 Expansion followed by uniform mesh 106

Bibliography 109

List of Figures

1.1 Evolution of MFs' market value until 2018, with projected growth until 2024 (plotted with information from [5]). 2
1.2 PL as a starting point for SL: at the top, indispensable stages in a PL process (PR coating, differential exposure, revealing); at the bottom, the mould produced by PL is used for SL (covering with PDMS, embossing, and plasma bonding with glass) [11]. 4
1.3 Effect of the duty cycle in waveguides fabricated inside fused silica on coupled light's profile and guiding seen from top. Adapted from [44] with images from [33]. 8
1.4 Summary of processes triggered by non-linear absorption of ultrafast laser radiation [48]. 9
1.5 Important results regarding how the fictive temperature of glass influences absorption peaks and etch rate for etching with HF: (A) Infrared central absorption frequency of Si for varying fictive temperature and for several solvents [52]; (B) Chemical etching depths as a function of time with HF for varying fictive temperature [51]. 11
1.6 Selectivity as a function of etching time, with two different etching agents and respective concentrations. The exposure was carried out with 100 nJ per pulse, circularly polarized laser radiation, and with an objective 100x lens with 1.35 numerical aperture. 12
1.7 Following an etching reaction through Bragg resonance detection in waveguide. (B) Transmission peaks of the sensing waveguide, close to the microfluidic channel fabricated with FLAE, for various tested fluids, and respective refractive indices. Both images are reproduced from [59], with permission. 13

1.8 Comparison of the ablation process in the presence and absence of water surrounding the exposed region. (A) Scanning electron microscopy image of the ablation on a silica substrate without a water bath [68]. (B) SEM image of the corner of a microchamber fabricated by water-assisted superficial ablation [69]. 14

2.1 Schematic representation of a FLDWU, where the ray tracing is only accurate from the writing module forward, and where the CCD/PC for monitoring is replaced by a screen (S). Notice the refraction of light inside the sample and the two spots formed by red/black rays (laser focusing off/on the sample surface). 20

2.2 Configuration of input and output polarization for normal incidence in a HWP rotated of β about the normal. Greyed axes are the eigen-directions of vibration of D inside the plate. Greek letters represent angle amplitudes with sign. 21

2.3 Photographies of the etching setups for: (A) HF etching, comprising the ultrasonics bath (UB), goblet with substrate (G), and protective material (gloves, Gl; teflon apron, A; glasses, PG); (B) KOH etching, comprising the gas exhaustion system (E), Allihn condenser (C), temperature control unit (TC), water cooling unit (W) and bath (B), the motor (M), thermometer (T), reactional vessel (V) and substrate holder (H). 25

2.4 Procedure for the alignment of the holder glass and the substrate containing the MF devices (left), and respective placement and clamping to the polishing jig (right). 27

2.5 Sevenfold magnification image of the same transverse region of the silica substrate, taken at the end of each of the polishing stages described in the text: first with an aqueous suspension of carbide 600-grit powder (left), second with calcined aluminium oxide suspension (center) and third with SF1 suspension (right). 28

2.6 Setup used for the analysis of the polishing stages and the removal of material throughout that process. The polishing jig comprises the substrate holder (SH) and the Z-screw (ZS) for lowering and lifting. The substrate (S) is observed via the Leica Microscope (LM). 28

2.7 Schematic of the MF contraction (the drawing is not to scale), with the numbering of vertices used in the `blockMeshDict` file. 31

2.8 Representation of the computational mesh and important lengths of the planar 4:1 microfluidic contraction, with a detail of the corner region (top) and flow lines for the case of Re=1 after reaching the steady state. 33

2.9 Moffatt vortices side (left) and top (right) lengths normalized to the narrow channel half-width as a function of time measured in units of the convective time. 34
2.10 Experimental setup for a PIV experiment [78]: tracer particles are mixed with the test fluid, which then is injected into the device, flowing through the examination region, which is illuminated with laser light at specific time intervals, for image capture, followed by mathematical treatment for velocity extraction. 35
2.11 Scheme of the acquisition process in a μPIV experiment, where t_E represents the time associated with one exposure, t_S the time between consecutive exposures within the same frame, F_n^t represents a set of frames starting at time t, and E represents an exposure. In general, $t_S = \mathrm{ME}t_F$, that is, when the exposures reach the defined number of exposures per frame, the software 'opens' a new one immediately. 37
2.12 Workflow and synergy between the three techniques used in this work. . . 39

3.1 Representations of (A) analytic solution for the flow in a channel with square cross section with $W = 50\,\mu\mathrm{m}$, first (B) and second (C) order corrections using perturbation theory on one side of the boundary, with the perturbation function $h(x) = \sin(2\pi/0.005x[\mu\mathrm{m}])$, and perturbation magnitude $\epsilon_r = 0.1$. 42
3.2 Simulation results for the simulated micro-channel, showing the velocity profile in a fully developed flow zone superimposed to the computational mesh (left), and the variation, with the streamwise coordinate, of the velocity at the centre of the microchannel, normalized to the average velocity (right). 45
3.3 Experimental points measured by Nikuradse [84], showing the lifted degeneracy of the friction factor $f = H/\left(\frac{L}{d}\frac{|\mathbf{U}|^2}{2d}\right)$ dependence on the relative roughness by the increase in the Re defined from the pipe diameter d. . . . 46
3.4 Mechanisms for the variation of the etch rate with the linear polarization angle: (A) Photograph of a voxel and nanogratings [85] oriented perpendicularly to $\mathbf{E}$ (left) and respective SEM image (d), along with structures formed after scanning along $\mathbf{e}_\mathrm{w}$ for several polarization angles (a)-(c) and 20 min in 0.05 % mass concentration HF [86] (arrow darkness proportional to respective etch rate); (B) experimental verification of etch rate dependence on the angle between $\mathbf{E}$ and $\mathbf{e}_\mathrm{w}$ (courtesy of J. Maia [47]). 47

3.5 Sequence of methods of which the FLAE technique is comprised: (A) Simple outline of a micro-channel by laser exposure along the axes of the cylinders, which represent the focal volume (after [87]); (B) Three different types of etching, considering the position of the channel inside the silica substrate – etching from the top facet (I), from the side facet (II) and through access ports connected to the surface (III). 48
3.6 Comparison of graded and uniform writing schemes. $\mathbf{k}_{\text{in}}$ represents incident wave-vector. 49
3.7 Filled contour plot of the dependence of the etch rate of laser scans on the distance to the left and right neighbour scans. 50
3.8 Determination of the threshold fluence per unit length (represented by the dashed black line) for the triggering of optical damage due to internal stress in channels with graded mesh etched with HF. 51
3.9 (A) Influence of depth and writing velocity in the etching evolution of a $\epsilon = 60\,\text{nJ}$ per pulse, $\delta = 4\,\mu\text{m}$ MF channel. $\mathbf{k}_{\text{in}}$ defines the direction of the laser beam. (B) Etch rates as a function of ϵ for different values of the writing velocity and depth (channels from first and second sets). 54
3.10 Transverse sections of channels etched from the top with KOH, taken immediately after writing (left), after 80 minutes of etching (centre) and 450 minutes of etching (right) as a function of writing energy and mesh spacing. $\mathbf{k}_{\text{in}}$ defines the direction of the laser beam. 55
3.11 Dependence of etch rates on the writing energy, depth, and scan separation, for channels produced with KOH-based FLAE, with (A) $v_{\text{w}} = 500\,\mu\text{m}\,\text{s}^{-1}$, and (B) $v_{\text{w}} = 800\,\mu\text{m}\,\text{s}^{-1}$. Red cubes represent channels where the combination of parameters resulted in visible fractures. 56
3.12 Fluences for the various micro-channels etched with KOH, where spheres represent damaged channels, and cubes represent undamaged ones, as a function of fabrication parameters. 57
3.13 Representation of the procedure for fabrication of a buried micro-channel with access ports to the surface, with all relevant geometric parameters. The inset represents a top view of simple access ports (left) and access ports all across the channel (right). 57
3.14 (A) Images composed by joining images of micro-channels etched with access ports, for various values of the separation between ports (distance between channels not to scale), after 360 min in HF. (B) Asymmetry parameter and tapering angle for the etched channels after the same time. . . 58

3.15 Visualization of the access ports and KOH penetration after 453 minutes for ports spanning the full width of the micro-channel with $\Lambda = 500\,\mu m$ (at the left) and for square ports with $\Lambda = 200\,\mu m$ (at the right). 59
3.16 Microscope images of a defect occuring in a etched from top microchannel after using a spatula for cleaning of PDMS debris on the surface. 60
3.17 Representation of the experimental error in obtaining the velocity profile for a fully developed Newtonian fluid flow using different IA lengths (values in pixels). 62

4.1 Sketch of one cross slot device, comprising two inlets and two outlets meeting at 90°. L_{ext} means the extensional length discussed in the text [58]. . . 65
4.2 Representation, using 4.1, of the mapping of the $y = 0.5x^2$ parabola into other lines, the correspondence being characterized by the associated offsets δ_r. 67
4.3 Characteristic parameters and preview of a hybrid slicing inwards (lower right) method and of a SCA uniform method (upper left). 71
4.4 Images composed from photographs of quadrants of the four different devices described in Table 4.1, taken ater laser engraving (left) and after 5 h of etching with KOH (right). 73
4.5 Top and side views of microfracture in sample `uni2_cteps` after polishing (arrows indicate the laser beam's wave-vector). 74
4.6 Microscope images of the `SCAuni2` after 345 min KOH etching (left) and after subsequent thermal annealing and cleaning with ultrasonics (right). Right image was manipulated to overlap perfectly with another post-annealing image. 75
4.7 Profilometer scans along the paths shown in the lower left corner insets of the `SCAuni2` device (left) after 480 minutes of etching, and (right) after 480 minutes of etching plus thermal annealing. 76
4.8 Profilometer scanning results for the OSCERs etched from the top with HF (top figures) and KOH (bottom figures). To the right of each plot, a microscope image of the respective device is shown, along with the scanning line. 77
4.9 Microscope images of two OSCER devices etched from the top with HF after 90 min (top images) and with KOH after 22 h (bottom images). . . . 78

4.10 Application of the processing algorithm provided by Dynamic Studio for the masking of data near the micro-channel walls (left, vectors in red), and of our algorithm for the determination of the centre stream line in the outlet (right, vectors in black). Vector sizes are normalized to the maximum magnitude in both images. 80
4.11 Velocity profiles for the central region of the cross-slot, obtained after data processing (see text), with an average correlation area length of (A) 16 pixels and (B) 32 pixels. Dashed lines represent the fitted function of Equation 4.3. 82
4.12 Influence of a slight defocus off the middle plane of the cross-slot, and of masking data frames containing bubbles and foam, on computed strain rate (triangles represent masked frames, MP means middle plane measurement, * represents a failure in the computation algorithm). 83
4.13 Comparison between PDMS based cross slot (data provided by the authors of [58], and FLAE based cross-slot. 84

A.1 Structure of a typical OF case, prior to (left) and after (right) the numerical simulation. 91
A.2 Mesh generation (right) from a ribbon (left), using the `cartesian2DMesh` utility of `cfMesh`. 93

Nomenclature

Roman Characters

$\mathbf{e_i}$	Unit vector in the i direction	Equation 2.6.
f_r	Laser repetition frequencys	Section 2.1.1.1
H, W, L	Height, width, and length, respectively	Section 3.1
$\dot{\ell}$	Etch rate	Section 3.4
p	Pressure	Section 2.2.3
P_{av}	Period-averaged laser power	Equation 2.1
Q	Flow rate	Section 3.1
$U_{x,y,z}$	Components of the velocity $\mathbf{U}$ along $\mathbf{e_x}, \mathbf{e_y}, \mathbf{e_z}$, respectively	Section 2.2.3
v_{w}	Velocity of the stage in the writing process	
Re	Reynolds number	Equation 2.4

Greek Characters

Γ	Laser fluence	Equation 1.1
γ	Laser fluence per unit length	Section 3.4
$\delta_{x,y,z}$	Separation between laser scans, when using line hatching, in the subscripted direction	Figure 3.5a
$\delta^{(i)}$	Separation between laser scans, when using contour hatching	Figure 4.3
ϵ	Energy contained in one laser pulse	Section 2.1.1.1
ϵ_r	Roughness amplitude measured in the characteristic length scale	Equation 3.4
$\Delta_{p/x}$	Pressure gradient along the x direction	Equation 3.1

ζ	Ratio between final and initial value in a geometric series	Equation B.3
κ	Proportionality factor relating attenuator percentage to P_{av}	Section 2.1.1.1
λ	Wavelength	Section 2.1.1.1
Λ	Spatial periodicity of access ports	Figure 3.13
μ	Kinematic viscosity	Section 2.2.3
ν	Dynamic viscosity	Section 2.2.3

Operators and subscripts

$\partial\square$	Boundary of $\square$	Equation 3.1
$\partial_i\square$	Partial derivative with respect to the variable i	Section 2.2.3
$\triangle\square$	Scalar Laplacian	Equation 3.1
$\nabla^2\square$	Vector Laplacian, defined as $\nabla\times\nabla\times\square-\nabla(\nabla\cdot\square)$	Equation 2.3
$\bar{\square}$	Average value	Section 3.1
$\square_{\text{th}}$	Threshold value	Section 3.4
$\square_{\text{ac}}$	Parameter referring to access port	Figure 3.13

Most relevant acronyms

DXF	Drawing Exchange Format
FLAE	Femtosecond Laser Assisted Etching
FLDWU	Femtosecond Laser Direct Writing Unit
FVM	Finite Volume Method
FVC	Finite Volume Cell
IA	Interrogation Area
LoC	Lab-on-a-Chip
μPIV	MicroParticle Image Velocimetry
MFD	Microfluidic Device
MF(s)	Microfluidic(s)
MNF	Micro and Nano Fabrication

NA	Numerical Aperture
MPA	Multiple Photon Absorption
NUO	Non-linear and Ultrafast Optics
OF	OpenFOAM®
OSCER	Optimized-Shape Cross-Slot Extensional Rheometer
PDMS	Polydimethylsiloxane
SCA	System Control Application
SDS	Sodium Dodecyl Sulfate
SHG	Second Harmonic Generation
STL	Stereolithography
THG	Third Harmonic Generation
WAFLD	Water-Assisted Femtosecond Laser Drilling

Notation and Conventions

Unless specifically stated next to an equation or a parameter, the natural units for all physical constants and variables are the ones in the *Système International (d'Unités)* [1].

The use of quotation marks is reserved to the explanation of acronyms and the inclusion of terms *ipsis verbis*, whereas the italic slant will be used for terms from other languages, enhancement of expressions and figurative meanings.

In order to mitigate any ambiguity, the three dimensions of a microfluidic structure which will be mentioned throughout this text are to be understood as, unless explicitly stated: *height* – the size alongside the direction, perpendicular to the flow, whose perpendicular planes section the structure into the same geometric figure; *width* – the size alongside the direction perpendicular to the flow, and to that which defines the height; *length* – the size alongside the direction of the flow.

Considering a slab-like substrate, laying horizontally while supported by its largest face, the following applies: the 'top' of the substrate is used to refer to the face opposing the support face and the 'side' face is used to refer to either of the four faces other than the top one and the support one.

To all owls and dogs.

Chapter 1

Introduction

1.1 Microfluidics, why and how?

Microfluidics (MFs) [2] gathers all investigation and accurate control of fluid flows in devices with at least one sub-millimetric length scale, and represents the entering in a new area in fluid mechanics, where surface, traditionally overlooked, forces and effects, like capillarity, act with a larger magnitude than bulk, inertial forces.

The inherently necessary miniaturization of devices establishes a contact point between fluid analysis and length scales compatible with both extremely small volumes and biochemical structures, whilst demanding a set of techniques which permit accurate and reproducible fabrication. These techniques, comprising micro and nanofabrication (MNF), have already been developing in the past century by means of the also miniaturization-dependent industry of microelectronics [2], thus creating a safe niche for the installation of MFs.

Nevertheless, the ever increasing necessity to accurately produce devices from highly precise theoretical optimized sketches, now demands rapid development from MNF in order to mitigate the limitations typical of its techniques' variate palette.

The connection between academy and industry is of paramount importance in the forward motion of the progress in MF, having the eternal dream concept of a mini-laboratory fitting in the palm of one's hand – an authentic lab-on-a-chip (LoC) – always in line of sight, motivated by the theoretical interest and, especially, the demands of a society rapidly growing in number and needing an appropriate scaling of the time it takes to carry out tasks, such as simple blood analysis.

By gathering a variety of interesting advantages, such as the possibility of performing fluid analysis having only a few drops at disposal, the LoC concept has found a number of enthusiasts all around physics, chemistry, molecular biology, and so on, granting MF a safe spot in those research areas in order to fully grow and develop.

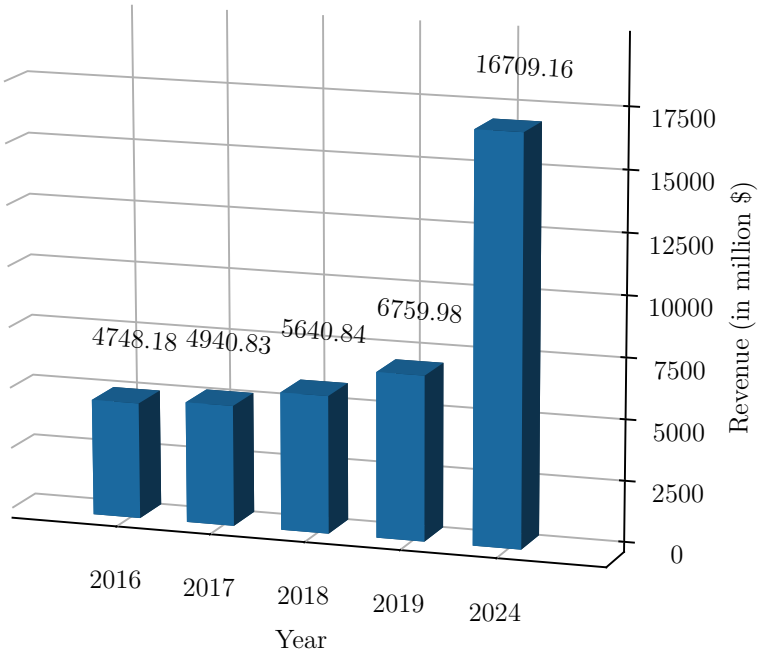

Figure 1.1: Evolution of MFs' market value until 2018, with projected growth until 2024 (plotted with information from [5]).

The approximation to biochemical species' length scales takes MF to the stage in many scientific areas, ranging from Medicine to Metrology, while showing a remarkable synergy with the Physics of materials. With sensing, cell analysis, separation and mixture of fluids in direct line of sight, the doors to replicating reactions occuring inside blood vessels, providing biological trials with a rapid diagnosis [3], mixture separation using electrophoresis or chromatography, are finally open to investigation, outputted to large scale applications like preterm birth diagnosis [4].

This level of impact in society is predicted to increase, elevating the economic status of MFs' market, which was valued at 5640.84 million dollars by the end of 2018, and is predicted to grow at a compound average growth rate of 19.84% until the projected value of 16 709.16 million dollars by 2024, according to Mordor Intelligence [5]. The growth of this relatively recent market is undeniable, as represented in Figure 1.1.

The combined action of increasing fiduciary valuation with the partnership with developing MNF has caused MFs' path to peak in the golden age we can witness today, as new processes arose in the field, with an important contribution coming from the advent of ultrafast laser and inherent processes of non-linear interaction between light and matter. The possibilities introduced by non-linear and ultrafast optics (NUO) translate into machining with unprecedented resolution and three-dimensionality, which allows to overcome some known obstacles, while implying costs which, so far, preclude large scale production. Nevertheless, these novel techniques have emerged and have been consolidating as

extremely attractive options for high precision production of MF devices, circumventing historical limitations of traditional techniques, as will be seen in the next section.

1.1.1 'Traditional' processes in microchannel fabrication

1.1.1.1 Photolithography and soft lithography

Rather imaginative, viable, medium-to-high fidelity fabrication methods have been suggested recently for inexpensive, mass producible LoCs, by exploiting new materials while (re)implementing manufacturing techniques for microscale applications. These efforts have culminated in the advent of paper [3], cellulose [6], and stainless steel [7] devices, three-dimensionsal (3D) printable mould resins [8], quasi-3D printing of CAD patterns to copper-coated films prior to etching [9], and even the use of thermoplastics as common as 'shrinky dinks' [10].

Despite these new methodologies, the pioneering mechanism for micro-pattern transfer, denominated photolithography (PL), still finds its use in most modern clean rooms, due to its high fidelity and established optimization. The principle of application is the exposure of a photosensitive substance (photoresist, PR), followed by the contact with a removal agent (developer) for the detachment of the unwanted material volumes.

In a photolithographic process, the substrate is initially cleaned via physical (compressed air), chemical (ethanol or piranha, a mixture of sulphuric acid and hydrogen peroxide) or hybrid (reactive ion etching) methods, covered by PR via rotational spreading and pre-baked for PR byproduct removal. Upon aligning with a mask, the set is exposed to an appropriate light source (when the pattern transfer itself occurs). The behaviour of the PR upon exposure defines its classification as positive (if exposed areas are removed by development) or negative (if exposed areas are instead what remains in the final structure).

The developing stage, similarly to what occurs with photographies, requires a developing agent, and an appropriate recipe, which is the object of important multivariate – development time, concentration of pre-polymer and curing agent within the PR, and temperature – optimization for the maximization of similitude. Finally, the substrate is cleaned with compressed air and/or deionized water. Post-baking is also an option whenever hardening and stabilization of the PR is a requirement, but dispensable and even undesired if there is an intention to further use MNF techniques on the unfinished structure[1].

[1]For instance, a lift off process, through which the substrate is further covered in target material and the PR is removed once more, in order to obtain a 'photographic negative' of the mask coated with the target material.

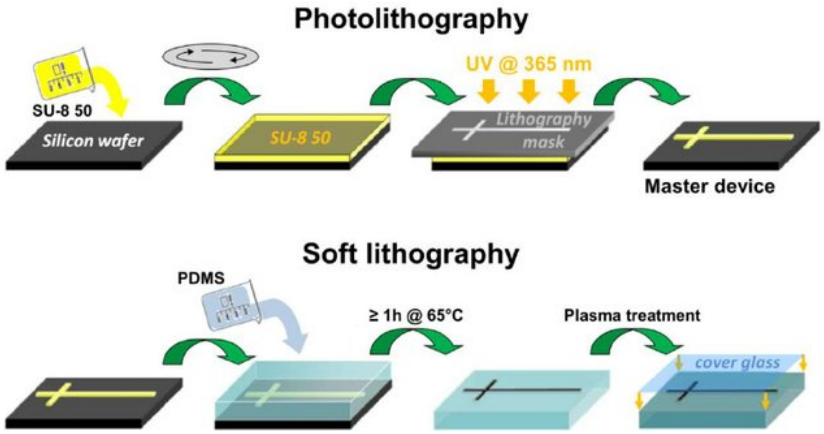

Figure 1.2: PL as a starting point for SL: at the top, indispensable stages in a PL process (PR coating, differential exposure, revealing); at the bottom, the mould produced by PL is used for SL (covering with PDMS, embossing, and plasma bonding with glass) [11].

Regarding soft lithography (SL), it consists of a set of techniques whose goal is to build functional micro and nanostructures by obtaining negative patterns from photolithographic ones. By filling patterns obtained via photolithography with the desired chemical compound, it is possible to make it acquire the desired shape, by the negative of the mould.

SL is the final step between a mould – which is often, but not exclusively, obtained by PL – and most of nowadays' large scale LoC applications. While not being exclusively connected to it, polydimethylsiloxane (PDMS) plays a preponderant role in those applications. PDMS is an elastomer with low complexity and cost production, and various applications in MF, due to its hydrophobicity, alongside the possibility of being rendered hydrophilic by plasma treatment. Its elastic nature allows for accessing tubes to be drilled with ease, and filled with a rigid fluid-guiding structure, such as aluminium tips or polytetrafluoroethylene (PTFE, commercially known as teflon) pipes, posteriorly kept in place by elastic forces, whilst also guaranteeing leak-tightness.

Furthermore, and most importantly, the transparency of PDMS is especially suited in visually inspecting the fluid-flow, thus enabling the use of optical microscopy techniques as a basis for several experimental methodologies, required in fluid-flow research [12], metrology [13, 14] and devices' performance analysis [15, 16], among others.

The curing of PDMS ensures that the pattern is permanently marked in the solid, gelatine-like structure, which can then be peeled-off from the mould. The PDMS stamps thus obtained are highly biocompatible, reusable and possess an adequate rigidity for most applications in MF.

The peeling from the mould is an indispensable critical stage of the process, and limits the range of microchannel geometries that can be produced with high fidelity. This

translates to a aspect ratio range of operability for PDMS-based SL (0.2 to 2) [17, 18], representing a limitation in many applications for sensing [19], cell growth studies [20, 21], micromixing and -pumping [22], and to produce 3D-patterns inside the channel itself, as investigated in [23].

Another limitation is the fact that the input pressure must be adequately kept below a maximum limit, given the risk of disintegration of the PDMS channel. This can result in a hindrance in applications such as clinical trials, and represents an impediment in continuing size reduction towards the nanoscale, since pressure grows with the inverse squared length scale.

1.1.1.2 Joining glass and PDMS: bonding processes

Bonding processes play an important role in obtaining final devices composed of different materials, which has been a recent tendency in microfluidic LoCs. The preparation of the surfaces prior to bonding constitutes an important procedure, since the presence of physical defects or chemical inhomogeneities may result in regions with higher fragility and prone to debonding.

Fusion bonding consists of an adhesion that is established by means of Van der Waals interactions between molecules in both surfaces [24]. These binding forces may be thermally enhanced, with high temperature annealing (about 800 °C for the case of silicon (Si). The activation of the contacting surfaces, by means of, for instance, HF or oxygen (O) plasma, results in a lowering of the annealing temperature threshold for an adequate bonding, which enables the use of this process in electronics and microbiology, which are areas in which temperature control is essential.

The most versatile alternative to fusion bonding is, by far, anodic bonding. It is a much less complex process, requiring lesser preparation of the bonding surfaces, as well as lower temperatures [25]. The bonding is mediated by applying a voltage difference between two electrodes (one placed in each of the interfaces). In general, the bonding forces are more intense in this process, as long as there is a sufficiently high concentration of alkaline ions in at least one of the surfaces – hence the recurrent use in bonding materials to glass.

The two substrates are made to come into contact at a high enough temperature, to which follows the establishment of a potential difference (with the glass acting as a cathode), which results in the electrolysis of alkaline ions inside the glass. Then occurs the migration of these ions towards the cathode and of the O ions towards the anode, where the Si atoms are oxidated, forming oxides whose bonding forces sustain the connection [11].

It is particularly interesting to mention that PDMS' physical-chemical properties also make it a valid candidate for spin coating, acting as an interfacial agent in glass/glass, PDMS/PDMS [26], and PDMS/glass. The first two alternatives conserved integrity with

input pressures of up to 400 kPa, in comparison with the 20 kPa threshold for PDMS/PDMS conformal contact. For the PDMS/glass bonding, the reported [27] burst pressures, ranging from 0.2 to 0.7 kPa, reflect the weakness of the adhesion provided, in addition to the increased protocol difficulty of requiring the curing of the PDMS membrane at high temperature (80 to 90 °C). Furthermore, these adhesive bonding methods are prone to channel geometry physical alteration and clogging due to the adhesive's thermal response during the required time for curing [28].

1.1.2 Microfluidic fabrication by laser techniques

It is difficult to believe that Theodore Maiman, back in 1960, could have ever imagined that his first ever implementation of a laser would carry so much significance and would be reminded today as the beginning of a whole new research area. Ever since, the laser has had a remarkable technological impact in many different areas and, within only a few decades, the possibility of generating ultrashort pulses represented a decisive change of gear in terms of the possibility of reaching optical intensities as high as ever, and 'writing' microfluidic devices in all three dimensions.

1.1.2.1 The advent of non-linear ultrafast optics

The progress in laser technology has been the work of numerous physicists, and has resulted in many Nobel prizes being awarded over the present and past centuries. A remarkable step forward was the discovery of mode locking [29], the technique through which the longitudinal stable modes in a laser cavity are made interfere constructively around a common peak, yielding the shortest laser pulses known to mankind, and unravelling ultrafast optics.

Ultrafast optics concerns the study of laser light emitted as pulses with typical durations of the order of the femtosecond, which trigger non-linear effects due to the high focal volume intensities of the order of $10^{19}\,\mathrm{W\,m^{-2}}$ – about 10^{11} times greater than that of light emitted by the Sun! This aspect means that nonlinear optics and ultrafast optics have walked side by side throughout the last quarter of the XXth century, meandering through discoveries such as femtosecond optical frequency combs [30] and chirped pulse amplification [31], which contributed decisively to the role that lasers play nowadays, through spectroscopy [32], microfabrication [33, 34], winding through applications as diverse as metrology [35], cancer treatments, and so forth.

1.1.2.2 Non-linear photon absorption

Non-linear optics, while being a relatively well established branch in Optics, bears exotic phenomena such as the production of new spectral content at frequencies obtained from the

originals by sums and subtractions, and non-linear photon absorption by matter. In fact, what occurs within material exposed to femtosecond laser radiation is quite different from linear photon absorption, which is only possible if the energy carried by that particle is greater than or equal to the bandgap energy of a certain material – which is a consequence of how the electronic states fill energy bands interleaved by gaps [36, 37].

The condition that one photon carries less energy than that required to overcome the bandgap is not an impediment for another sort of absorption, non-linear absorption, provided the intensity (proportional to the surface density of photons) within the focal volume is so high that the arrival of more than one of these underenergized photons is almost simultaneous, resulting in a cumulative effect responsible for the ionization [38]. Depending on the number of photons absorbed by one single atom, this phenomenon is referred to as 2PA, 3PA, or, in general, multiple photon absorption (MPA).

Non-linear absorption is associated with an intensity threshold, which is reached by femtosecond lasers, due to the cumulative effect of their characteristic short period, and the decrease in beam waist due to Kerr self-focusing [39] – a non-linear third-order [40] effect characterized by the dependence of the effective refractive index on the intensity of the beam itself.

The most distinctive aspect, in terms of possibilities for micromachining, of non-linear absorption is the fact that it occurs without the thermal damage typical of high intensities in linear absorption [41], by happening after the pulse's temporal duration, and allowing higher energies to be reached, provided the duration is sufficiently small so that intensity overcomes the threshold for the transition to non-linearity.

1.1.2.3 Femtosecond Laser Assisted Etching

The first contribution of NUO to microfabrication dates back to 2001, when Marcinkevičius *et al.* reported [42] silica substrates' micro-machining using ultrashort period radiation pulses, by using a technique later baptized as femtosecond laser assisted etching (FLAE) or femtosecond laser irradiation followed by chemical etching (FLICE).

Consisting of a two-staged process, where a selective chemical etching follows a substrate's irradiation with femtosecond laser light, FLAE is the only monolithic, truly 3D, sub-micrometric resolution process for the fabrication of hollow structures inside substrates.

Following the first steps, the technique has grown due to improvements on both stages of the process. Original works used hydrofluoric acid (HF) as the etching agent, while already predicting a future application of the assembled hollow structures in MF experiments, which can now be said to have been quite the keen prediction of a very extensive line of sight for this relatively recent area in fluid mechanics.

Key parameters in the writing process are the writing velocity and the energy involved in the process. Not all energies produce the material changes as desired, and even amongst the range that does, the uniformity of the final structures is affected, especially if the energy control is performed by altering the duration of laser bursts. In fact, energy can arrive to the substrate in single pulses or in bursts, which is proven to be more effective [33]. The duration of these bursts, each comprising multiple laser pulses, can be controlled with the duty cycle of an acousto-optic modulator (AOM). This mechanism allows, therefore, for the production of structures like gratings [43].

The AOM principle of operation is the alteration of refractive index of a material as an acoustic wave propagates through it, and the consequent deflexion of light that traverses such medium [45]. Light then diffracts, constructively interfering in preferencial directions, thus splitting the initial power with a controlable ratio. This mechanism allows for power control, by inputting femtosecond pulses and selecting the appropriate beam from the AOM output. Further, the AOM can temporally sample a femtosecond laser beam, acting as a shutter that is opened a percentage of time in a period of modulation, that percentage being the duty cycle. It is widely documented that duty cycles [46] affect the quality of produced gratings, as suggested in Figure 1.3.

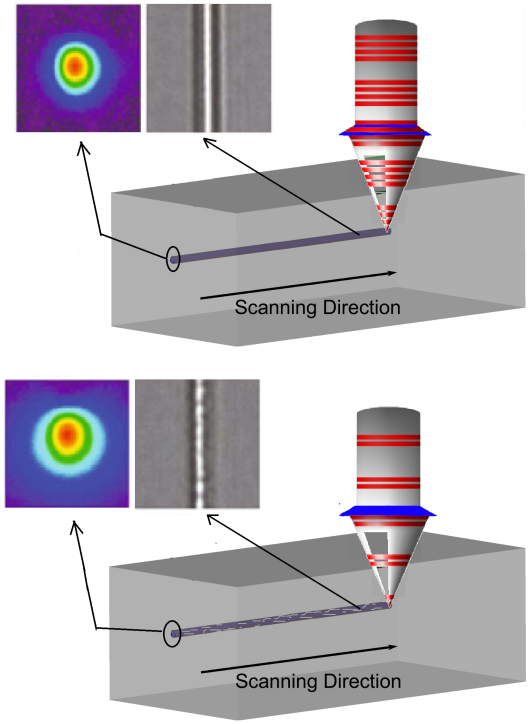

Figure 1.3: Effect of the duty cycle in waveguides fabricated inside fused silica on coupled light's profile and guiding seen from top. Adapted from [44] with images from [33].

Modifications in photo-exposed material. For a full understanding of the processes by which silica is affected chemically and structurally through exposure to ultrafast radiation, it is recommended the reading of the introductory chapter in [47] and references therein. In what follows, it is intended to summarize especially those concerning the fabrication of microchannels.

When ultrashort light pulses are focused inside an homogeneous material, non-linear absorption phenomena are likely to occur, which comprise impact ionizations due to avalanche phenomena or regular field ionizations. These phenomena locally raise the energy of electrons, which are now in the conduction band, and results in a localized alteration of the substrate's composition, as summarized in Figure 1.4.

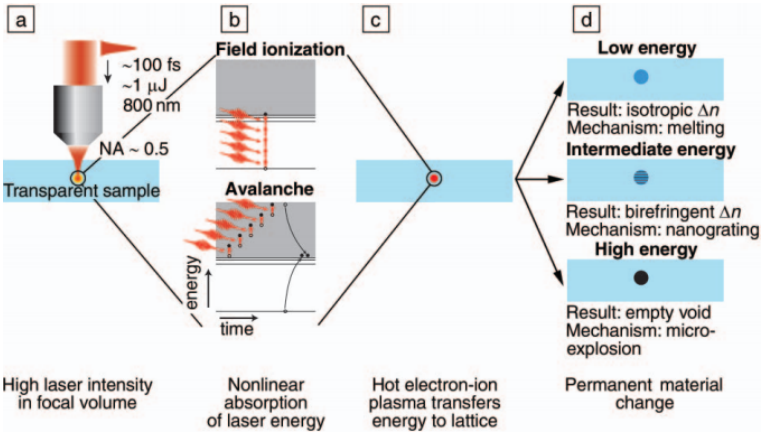

Figure 1.4: Summary of processes triggered by non-linear absorption of ultrafast laser radiation [48].

Due to the characteristic time scale of femtosecond laser radiation being at least three orders of magnitude lower to that of thermal phenomena, such as photon-phonon interactions, the question of the optical damage threshold being crossed has no direct answer in how fast energy is provided (because dissipation will always occur at a slower rate), rather in how much it is provided, per unit area. Therefore, it is the laser fluence,

$$\Gamma(t) = \int_0^t I(\tau)\,\mathrm{d}\tau, \tag{1.1}$$

which dictates the separation of the non-linear absorption into three regimes, each exhibiting its own characteristics, albeit sharing the irreversibility typical of crossing the optical damage fluence threshold. These regimes, represented in Figure 1.4, can be stated as follows [41]:

- type I, especially suited for writing waveguides, is characterized by a laser fluence range just above the threshold for optical damage, causing a refractive index change in the focal volume;
- type II, which is exploited for the fabrication of hollow structures through FLAE, occurs for intermediate laser fluencies, with nano-gratings being formed with a sub-wavelength characteristic period, oriented parallelly to $\mathbf{E} \times \mathrm{d}\mathbf{r}$, where $\mathrm{d}\mathbf{r}$ is tangent to the path followed by the stage when writing;
- type III, where voids and micro-explosions occur, stemming from the vaporization and incorporation of material into the surroundings of the focal volume, densified as a result.

Concerning the nature and role of the type-II modifications at the very core of the FLAE technique, initial studies [42, 38] pointed out second ionization mechanisms via the

plasma formed upon primary absorption as evidence of the coupling between silica and incident light. In the type-III regime, the densification of the surrounding area is associated with an alteration of the bonding angle between Si and O bonding angle, $\theta_{\mathrm{O-Si-O}}$, which results in greater reactivity of the O radicals and greater etching velocities.

More recently, other Si densification processes, even within type-II processes, were suggested by Raman spectroscopy data to be a result of a higher fictive temperature [49] T_{f} in exposed areas. That can be understood themodynamically as a dislocation of the typical glass phase transition to other ranges of temperatures, alongside chemical structural changes in molecular orbitals, resulting in quartz rings in these modified areas with less molecular weight than those in unexposed regions – three and four element rings become more predominant, as opposed to six element ones [50] –, which may be thought of as a reduction of chemical endurance.

The modelling of these modifications was advanced by Agarwal *et al.* [51], who studied the relation between shifts in the Raman response of silicon and the increase of its fictive temperature, T_{f}, at which the configurational entropies of the liquid and glassy states are the same. In fact, experimental data in Figure 1.5b evidence that ressonance peaks are red-shifted as T_{f} and the subsequent etch rate both increase; as the direct linkage between ressonant frequency and the mean bond angle $\theta_{\mathrm{O-Si-O}}$ had already been established [52], it was hypothesized that a decreasing $\theta_{\mathrm{O-Si-O}}$ could be the cause of the increase in etch rate.

Simultaneously, the formation of structures with high percentage of Si and of defects in the crystal lattice (designated colour centres) can be modelled by a Sellmaier summation for the refractive index variation with the wavelength, exhibiting fotoinduced absorption peaks, in order to explain the densification of silica, which is also attributed [53] to the formation of permanent dipoles in glass.

Although the formation of colour centres help explain the silica densification, the disagreement with established data regarding the influence of polarization [54] led to studies on densification induced by internal tensions in the material [55].

Finally, the reader is referred to a relatively recent discussion of the type-II modifications forming the basis of microchannel fabrication, where Hnatovsky *et al.* [56] study beyond linear polarization–induced self-ordered and oriented nanocracks, reporting disordered nanostructures with circular writing polarization.

Just like a photograph: chemical etching as a developer. The family of etching processes refers to physical-chemical processes aiming for selective removal of material from a substrate.

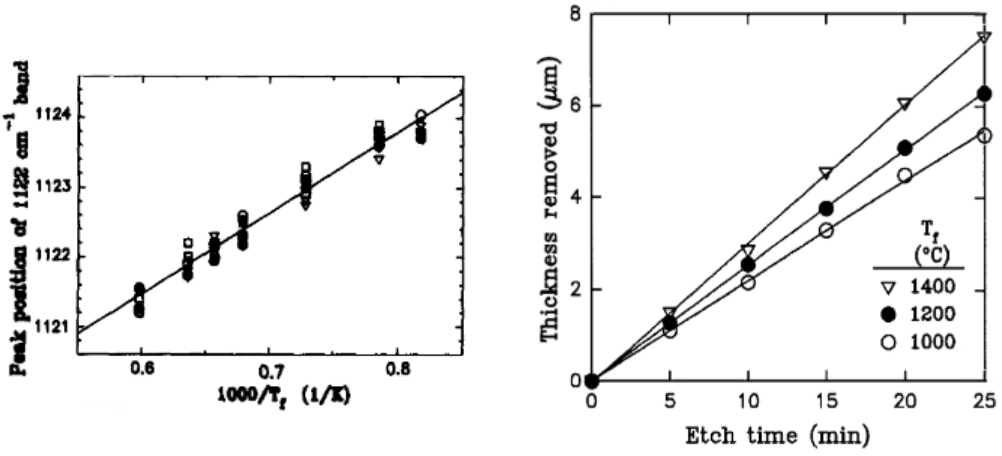

(A) (B)

Figure 1.5: Important results regarding how the fictive temperature of glass influences absorption peaks and etch rate for etching with HF: (A) Infrared central absorption frequency of Si for varying fictive temperature and for several solvents [52]; (B) Chemical etching depths as a function of time with HF for varying fictive temperature [51].

In order for that to happen, a chemical or structural modification must occur inside the material prior to the exposure to this developing agent, which may act through physical, chemical, or both processes. The ratio between the rates at which desired and undesired material removal occur is termed selectivity, and is one or two orders of magnitude above unity.

The most common etchants in the context of FLAE are HF [42] and potassium hydroxide (KOH) [57]. In spite of HF's historical relevance in MF applications, the associated etching has a few negative points, namely, its high corrosiveness, the limited selectivity due to the high etch rate of pristine silica, and the (mostly) isotropic nature of the etching, which has a consequence a discrepancy between the final structure and the initial design.

Kiyama *et al.* [50] have studied comparatively the chemical attack with KOH and HF. Although 2% HF has limited the aspect ratio to 21, regardless of the etching time, KOH, despite of inferior etching velocities, allowed for a globally superior selectivity, which is represented in Figure 1.6. This inconvenient in the etching velocity may be mitigated by an increase in KOH etching temperature, with the objective of reducing the etching time.

Also in Figure 1.6, it is possible to observe the saturation of the etching selectivity depending on the etching agent. This occurs mostly due to limitations in the access of the 'fresh' etchant to the wavefront of the etching process, usually further and further away from the etchant reservoir. KOH also offers an advantage regarding this saturation, which makes it preferable for the fabrication of very precise structures by the FLAE technique. The cycling of the etching process and a comprehensive study of its saturation are proposed in literature [56] to circumvent the diffusion-wise limitations of the process.

The detailed investigation of the etching process, after exposure to ultrafast laser radiation, is relevant for the determination of the set of writing and etching-controlled parameters which result in the absence of fractures and similitude/reproducibility of the process for the production of microfluidic structures. Amongst the features that it is advised to monitor, one may state the uniformity of the channel in terms of transverse section, either in one of these, and along the length, the ability to perform curves with several degrees of sharpness and the ability of fabricating sharp corners in intersecting channels, for instance, as required in every cross-slot–based geometry [58].

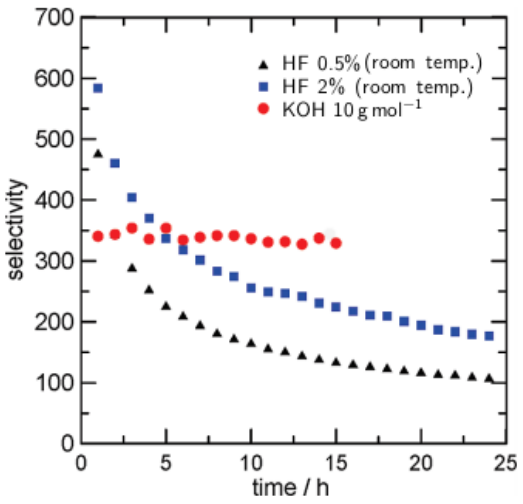

Figure 1.6: Selectivity as a function of etching time, with two different etching agents and respective concentrations. The exposure was carried out with 100 nJ per pulse, circularly polarized laser radiation, and with an objective 100x lens with 1.35 numerical aperture.

Recently, monitoring processes for the etching reaction have been developed, with the objective of determining the ideal time to initiate the removal of the sample from the etchant solution. One of those processes [59] is based on the measurement of the variation of birefringence of a Bragg grating waveguide (BGW). Materials which exhibit birefringence show an anisotropy regarding the phase velocity of electromagnetic waves, which is intrinsically connected to the existence of eigenmodes – that is, well defined modes of vibration – for the electric displacement inside them [60].

The BGW typically possesses a transmission peak, which in fact is a small plateau centred around the resonant frequency, with a length connected to the limit in interference possible in a device with finite length. The effect of birefringence translates in an unfolding of the transmission peak into two peaks at $\lambda^{\mathrm{B}}_{1,2} = 2\, n^{\mathrm{eff}}_{1,2}\, \Lambda$, where Λ is the BGW period, $n^{\mathrm{eff}}_{1,2}$ are the effective indices for different incident polarizations and $\Delta n = |n^{\mathrm{eff}}_2 - n^{\mathrm{eff}}_1|$ is the birrefringence, separated of $\Delta\lambda = 2\,\Delta n\,\Lambda$. Therefore, the characterization of the spectrum of light which leaves the BGW informs about birefringence, hence, about the amount of removed material, given that this removal reduces the material stress in the BGW, which is responsible by the birefringent optical behaviour [61].

As the etching reaction is monitored, like in Figure 1.7b, the interruption becomes possible once the optimal stage is reached, that is, the resonating wavelength starts to decrease, notwithstanding the latency in measurement, which does not occur in real time, but between defined time intervals.

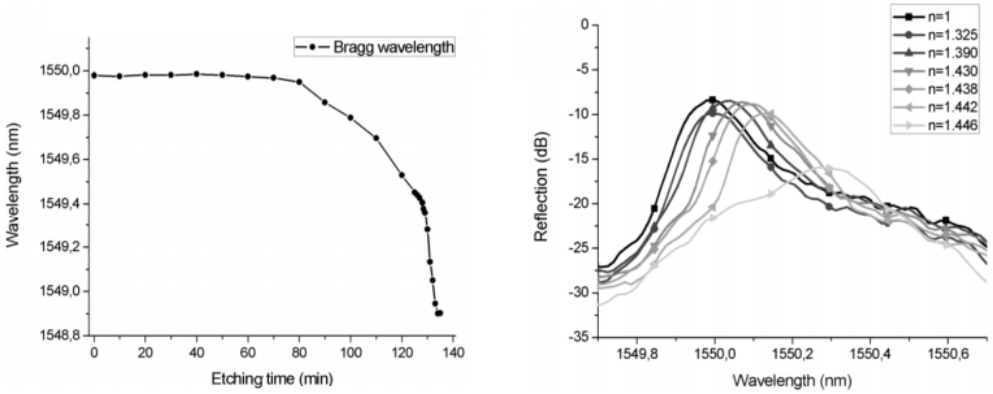

(A) (B)

Figure 1.7: Following an etching reaction through Bragg resonance detection in waveguide. (B) Transmission peaks of the sensing waveguide, close to the microfluidic channel fabricated with FLAE, for various tested fluids, and respective refractive indices. Both images are reproduced from [59], with permission.

This procedure is, however, dependent on light's ability to sense the presence and the properties of the material around it, whether pristine or modified by the laser pulses. Therefore, the propagating mode must be sufficiently spread around the BGW, that is, the intensity profile must extend itself to the periphery of the waveguide. This spreading is inversely linked to the refractive index difference between the BGW and the fluid flowing in the sensing microfluidic channel [59] – this relation is evidenced in Figure 1.7b. Future applications in real-time monitoring for adequate etching interruption must necessarily take these considerations into account.

1.1.2.4 Water Assisted Femtosecond Laser Drilling

Even though FLAE is compatible, in principle, the fabrication of three-dimensional structures with submicrometric precision, it carries along additional difficulty due to the two steps in which the process is based [62]. Another way for ultrafast optics-based substrate micromachining, originally proposed by Li *et al.* [63], back in 2001, includes bathing the substrate with distilled water while it is exposed to radiation. This water assisted femtosecond laser drilling (WAFLD) technique exploits the possibility of instantaneous removal of residues, while the ablation process' efficiency is enhanced by the increase in pressure due to confinement, as well as the temperature's control – which ensures the sample's integrity.

On the other hand, the laser efficiency is lower in an aqueous medium, due to the associated absorption mechanisms and photon diffusion both in depth and at the water's surface, which results in a superior optical destruction threshold and energy spending in the writing process, in comparison to FLAE. The writing process itself is formally identical

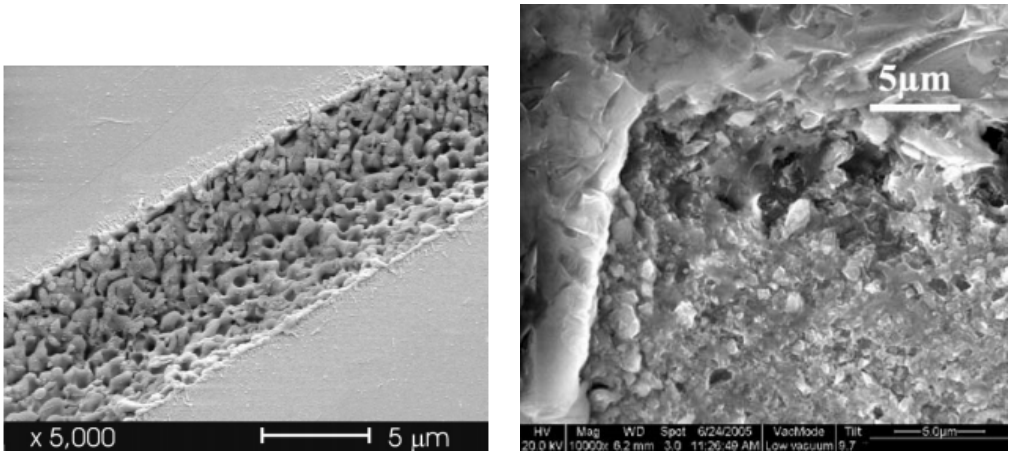

(A) (B)

Figure 1.8: Comparison of the ablation process in the presence and absence of water surrounding the exposed region. (A) Scanning electron microscopy image of the ablation on a silica substrate without a water bath [68]. (B) SEM image of the corner of a microchamber fabricated by water-assisted superficial ablation [69].

to that used for FLAE, and further explained in Chapter 2, aside from the contact with the aqueous medium via either the exterior facet of the sample [63, 62] or around it [64, 65].

Subsequent optimization of WAFLD has followed, and resulting in high precision applications, some of which requiring a much harder fabrication if by FLAE [65]. Since the technique was originally proposed, relevant microfluidic devices have been produced (microdivider and micromixer [65]), channels have been produced with smaller ablation fluency thresholds [66], high aspect ratio and curvy geometries [67], as well as microchambers connected to the outside through microtrenches (Figure 1.8b) and bridges connecting two channels from above a third one [64], among others.

The velocity at which the ablation occurs must be limited inferiorly – where the bubble formation precludes the effective removal of debris – and superiorly – where the exposure is insufficient and no quality structures can be produced [69]. On another matter, the smaller roughness associated to ablation with the WAFLD technique, represented in Figures 1.8a and 1.8b, may be attributed to a lower debris deposition and lower cyclic effect of fusions and solidifications of the substrate's material imposed by the successive laser pulses.

Liquid-assisted techniques for femtosecond laser drilling have benefited, recently, from the introduction of a novel porous glass, providing an alternative to the accumulation of ablation debris and subsequent clogging of the micro-channels [70]. The length scale of the pores, which is of $\approx 10\,\text{nm}$, enables connectivity between voids in the glass, amounting to about 40 % of its volume, facilitating liquid penetration throughout the material. The

pores can then be sealed, upon fabrication, by a thermal treatment of the glass substrate, constituting a novel sub-diffraction limit fabrication technique for MF channels.

1.2 Objectives and contributions of this work

PDMS-based fabrication of microchannels is a widely disseminated pathway for microfluidic research. However, it faces a number of inconvenients, either related to the nature of the soft lithographic process (such as the impossibility of fabricating devices with aspect ratios larger than 2, due to the risk of destruction in the peeling off the original mask, and the difficulty in the bonding of the cover PDMS/glass, while controlling accurately the inlets' and outlets' location by superposition), or to the limited range of input pressures that these microchannels can be subjected to without leakage occurring.

Channels and structures fabricated in silica substrates offer the possibility of overcoming these limitations, and, if fabrication occurs perfectly integrated in the glassy medium, the bonding of PDMS with a substrate can occur in separate turns for each inlet or outlet, unlike for superficial channels, where the PDMS holds the accessory job of covering the excavated micro-volume.

With these considerations in mind, it is intended to explore MF in silica substrates, by characterizing FLAE in terms of comparing the final devices obtained by KOH and HF etching, and optimizing the writing process itself. The produced channels, either at the surface or embedded in the substrate, are validated for microfluidic applications, with μPIV measurements compared with numerical simulations developed in OpenFOAM®. It is intended to confront the predicted impact of several fabrication-wise features of the technique with their true impact on the fluid flow.

In addition, possibilities of performing size reductions towards the border between the micro and the nanoscale are explored, whilst evaluating both the resolution of FLAE in terms of the writing and etching stages individually and the experimental feasibility of near nano-channels in terms of fluid coupling and characterization viability through μPIV.

1.3 Contents and structure of the present thesis

The work developed between February and October 2019 has culminated in the writing of this thesis, which is divided into five chapters, including the present (introductory) one, and two appendices.

Chapters 2 to 5 share their global structure, beginning with an abstract, where the principal methods that were developed are mentioned, and the principal conclusions that

can be taken are highlighted. Following the abstract, come a variable number of subchapters, with the aim of, sequentially, demonstrating the utility and relevance of the studies which were conducted, explaining the basic, theoretical concepts which back up the computational and/or experimental work developed – with a much narrower and chapter-oriented scope –, and, finally, showing the results that arose from experiments, alongside the necessary comments and attempts of explanations based on theoretical qualitative and quantitative models, whenever suitable.

In Chapter 2, the reader finds a description of the concepts, tools, and equations, – especially in terms of Fluid Mechanics, Nonlinear, Ultrafast Optics, and Discretization and Numerical Simulation – which are essential for an adequate comprehension of the present work, alongside the three techniques it is based on: finite volume method (FVM), FLAE, and micro-particle image velocimetry (μPIV). Meanwhile, one typical, widely studied example is presented through all all these techniques, as a first approach: the case of the MF 4:1 contraction.

In Chapter 3, the detailed study of the microfluidic channel, which forms the basis of more complex devices is proposed. Firstly, the FLAE technique was implemented with HF and KOH, and an experimental comparison is presented, together with the optimization of the writing process for KOH, which was undocumented thus far, with the present laser system. Then, it was verified, either by theoretical and numerical predictions, and by fabricating the devices and testing experimentally, the impact of roughness in the laminar flow through a square cross section pipe, and compared numerical, ideal flow through those pipes to that which was studied with the aid of μPIV. In this final experimental stage, comments are made concerning the viability in characterizing devices with smallest characteristic dimension progressively closer to the nanoscale than to the microscale. These studies were carried out for channels fabricated at the surface of the glass, and embedded in the same medium, by accounting numerically for the influence of access channels in the fluid flow, while a comparative analysis is carried out between the two methods, regarding possibilities for MF applications.

In Chapter 4, the possible limitations of the FLAE technique in terms of spacial resolution are verified. For that, an optimized shape cross-slot extensional rheometer (OSCER) was fabricated and characterized in terms of mismatch between final pattern and intended pattern. Several meshing schemes are tested and compared in terms of the final verisimilitude, and one of these devices is tested with μPIV, and compared to profiles obtained with other fabrication processes, and numerical simulations.

In Chapter 5, conclusions to all these studies are presented, alongside a confrontation with the objectives of the present thesis, commenting on new, or incomplete, questions, to

be pursued in the scope of the experimental work developed so far, as part of the future work.

In Appendix A, the case of a microfluidic contraction is presented alongside OpenFOAM® code, for the simulation of that structure for several values of the Reynolds number.

In Appendix B, mathematics referring to grading mesh automated generation are presented.

Chapter 2

Materials and Methods

This chapter presents a theoretical description of the methods used in this work. The reader will find technical details regarding the setups used in the context of the FLAE method, a starting guide to OpenFOAM® and the implications for pre- and post-processing of the finite volume method, as well as a description of the microparticle image velocimetry system for the experimental characterization of flows, with the associated context in terms of possible uncertainties.

Additionally, an introduction to fluid mechanics is given, inasmuch as it provides context to the work developed. Finally, the case of the microfluidic contraction is studied numerically and experimentally, as a means to directly apply OpenFOAM® and microparticle image velocimetry to a benchmark microfluidic case study.

2.1 Experimental realization of FLAE

2.1.1 Femtosecond laser irradiation

2.1.1.1 Experimental setup

The realization of a system which allows for a controlled irradiation of a substrate, with tunable characteristics, is essential for a reproducible, and optimised application of FLAE to engrave microchannels. Hereinafter, the process of exposing a substrate alongside a predetermined path will be referred to as writing, and the system capable of performing such a task will be referred to as a femtosecond laser direct writing unit (FLDWU).

The fabrication of microchannels was carried out at the Centre for Applied Photonics (CAP), based at Faculdade de Ciências da Universidade do Porto (FCUP). A recently (January 2019) installed fabrication unit, is able to provide state-of-the-art micro-machining possibilities by including a friendly user interface, which encompasses also the input format for the geometries one wishes to fabricate, and a rather complete and self-contained

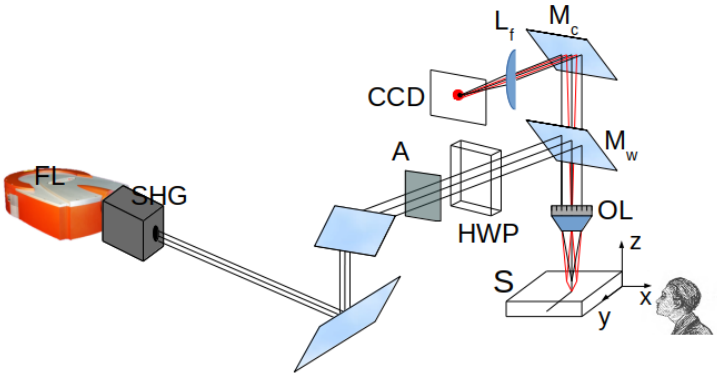

Figure 2.1: Schematic representation of a FLDWU, where the ray tracing is only accurate from the writing module forward, and where the CCD/PC for monitoring is replaced by a screen (S). Notice the refraction of light inside the sample and the two spots formed by red/black rays (laser focusing off/on the sample surface).

setup providing a more complete set of degrees of freedom in the asymptotic path to reproducibility and similitude to the intended geometry.

A beam of ultrafast radiation is manipulated within a FLDWU, in order to concentrate its energy in a microscopic focal volume inside a sample, triggering non-linear absorption. The FLDWU is composed of several main blocks: power control, polarization conditioning, visualization/alignment, sample scanning stages, galvanometric beam scanning, and focusing head. In the context of the laser system available at FCUP, here it follows a brief description of the key modules of our experimental setup:

Laser. The femtosecond laser is a fibre-amplified diode-pumped Amplitude Systèmes Satsuma HP2+, lasing at $\lambda_0 = 1030\,\text{nm}$, fitted with an harmonic generation module allowing second (515 nm) and third (343.3 nm) harmonic generation..

Throughout this work, the second harmonic wavelength was used, which is justified by the material composing the substrates for writing, which is SiO_2 (silicon dioxide or silica), whose relatively small bandgap of 8.9 eV is compatible with multiphoton absorption at that wavelength, so much so that its usage for micromachining is ubiquitious in literature [44, 61].

The pulses, as characterized in the user manual, show a 250 fs duration, and maximum average power of 5.5 W (at λ_{SHG}). It is possible to change the repetition rate, f_r, provided $f_r \in [0.5, 2]\text{MHz}$.

The effect of the f_r in the quality of the produced channels was not assessed, since it was set to 0.5 MHz and kept unchanged. The energy contained in one laser pulse, ϵ, will be varied between two to three orders of magnitude below ϵ_{max}, situating the modifications

within type II anisotropic index changes (Section 1.1.2.3). Bearing in mind the definition of the average power, P_{av}, it is straightforward to relate it to ϵ:

$$P_{\text{av}} = f_r \epsilon. \tag{2.1}$$

Finally, the control of the laser is performed, in a first instance, by a LabView application. The laser works independently from the FLDWU, unless the control is handed to the system control application (SCA), by setting the laser trigger to external. However, f_r control is only possible via the LabView application, as is the control of the laser frequency, and the control of the modulator percentage. An internal AOM permits a first mechanism of power control, through a non-linear dependence of power which exits the laser on the AOM efficiency – for reference, all fabrications were performed while keeping the modulator efficiency at 60%.

Entrance. Light is driven through the air from the non-linear frequency transformation black-box to a periscope, elevating it from the plane of the workbench to the plane where all optical components are.

Control. Light transverses two important optical components: an attenuator, for power control, and a polarization rotator, for polarization control.

In order to rotate polarization, the writing system includes a half-wave plate (HWP), which is composed of an optically anisotropic material (crystalline quartz), that selectively slows one propagation eigenmode relatively to the other, due to a lattice-originated anisotropy in the distribution of the velocity of propagating modes. The direction-dependent refractive index translates into the imposition of a phase shift between eigen-components, which, for an adequate length of the crystal, equals 180°, that is, the polarization tilting angle is inverted relatively to the so-called fast axis of the plate. By rotating the plate of β, so does the optical axis within the same plane, and the transformation is now depicted with generality, in Figure 2.2. If the device is placed so that the fast axis is initially parallel to the vibration direction of the incident electric field, a rotation of β of the HWP translates to a twice as large change in the tilting

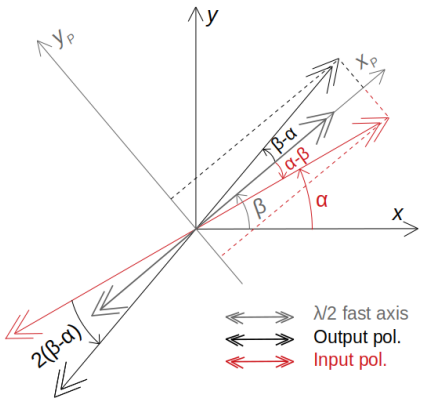

Figure 2.2: Configuration of input and output polarization for normal incidence in a HWP rotated of β about the normal. Greyed axes are the eigen-directions of vibration of D inside the plate. Greek letters represent angle amplitudes with sign.

angle of the polarization. When interacting with the `Polarizator Rotator` available in SCA's GUI, one must input half the angle that the polarization is required to rotate.

The polarization calibration before writing is performed with an analyser and with the `Polarization Rotator` command in SCA. It is possible to rotate the direction along which lies the polarization of the beam, in order to align it with the axis of the analyser, which can, in turn, be aligned with the x direction in the stage. In practice, the minimum of transmission is found instead – because the visual inspection is more sensitive to the large relative variations near that minimum, – and the maximum can be found by further rotating, within SCA, of another extra 45°.

The writing energy must be set adequately, following a calibration of the relation between the Attenuator percentage variable and the power before and after the objective. By measuring the power before and after the objective, for different values of the attenuator percentage (AP), a calibration line can be plotted, and a calibration factor κ, can be computed, for later use in SCA.

The change in writing energy is straightforward, and can be understood as follows: suppose incident radiation characterized by f_r and ϵ, and whose associated power used for writing – that is, after all losses in the optical system –, is given as a linear function of the AP. The total energy per unit time is, then, $\epsilon f_r = \kappa \cdot \mathrm{AP}$, where κ is the proportionality factor. The dependence can be solved for AP, and writing energy can be controlled in this manner.

For power control, a watt pilot is employed, consisting of two Brewster thin film polarisers and a HWP. The thin films are placed at an angle relatively to the incident beam, so that the component of polarization parallel to the plane of incidence is extinguished upon reflection. In such a configuration, the rotation of the HWP permits the control of the fraction of polarization which arrives at the thin films parallelly to the plane of incidence, thus the fraction which will be transmitted.

Writing. The substrate is placed in a xyz motorized stage, and light reaches it after being focused by a converging objective lens. The positioning system features an in-plane resolution of 5 nm, and a z resolution of 2 nm, and respective accuracies of ± 300 nm and ± 200 nm. Being mounted on a granite base, the impact of external vibrations such as doors opening, outside traffic, or moving chairs is minimized. Three different focusing optics are available for writing. However, all the works were carried using a 50x magnification objective lens, with a numerical aperture (NA) of 0.42, working distance of 17 mm, and a resolving power of 0.7 µm.

Visualization and tracking. The substrate is illuminated, reflecting light back into a camera, which produces live imaging for locating important points prior to fabrication.

The imaging device consists of a coupled charge device (CCD), and operates with 590 nm coaxial illumination from a light emission diode source. The images are sent to the laboratory's computer, thus allowing the operator to visualize the substrate, and to superimpose to that image the intended laser paths.

2.1.1.2 Experimental method

The presence of dust and other contaminants in the substrate can cause deviation of the beam, loss of optical power, and optical aberrations, contributing to an unsuccessful writing process. This issue is addressed by inspecting the substrate in a clean-room environment, cleaning when necessary with a sequence of ethanol, acetone, and isopropyl alcohol, followed by deionized water and a jet of compressed air.

Relatively to optical control prior to starting laser irradiation, it is necessary to set ϵ, and the orientation of the linear polarization relatively to the scanning direction, θ_{P}, and to locate the substrate in the frame of reference of the stage.

First, the laser incidence must be as normal as possible to the substrate. This ensures that the writing process occurs with minimal optical aberrations, and with minimal error in the definition of the beam's polarization (because the eigenmodes of propagation inside the substrate do not necessarily coincide with those of free propagation in air).

For the verification of quasi-normal incidence of the beam relatively to the stage, a mirror is placed on it, and the reflection analysed with the aid of a pierced piece of cardboard, in order to check deviations from the incidence angle.

The polarization is chosen by taking into consideration the direction of writing. Recalling Section 1.1.2.3, the orientation of the nano-gratings formed in type II regime is as a function of the angle between the beam's polarization direction and the writing direction, $\theta_{P,W}$. When such angle is 90°, the nano-gratings are oriented in a configuration which facilitates the subsequent acid penetration, as opposed to when the direction of writing and beam's polarization are collinear. In fact, it was verified that the etch rate shows a maximum for $\theta_{P,W} = 90°$. The theoretical dependence predicts a divergent behaviour at this angle, which is in fact an increment of 1000% relatively to the case of colinearity [47].

The control of the polarization angle was performed with an analyser placed on top of a viewing card, by varying the rotation angle of the HWP and visually inspecting the occurrence of a minimum in intensity of transmitted light.

The laser profile is then inspected with a viewing card, with the objective lens in place. Using an iris, the beam diameter is reduced, and the visualization of diffraction rings is employed to verify that the beam profile is centred in the objective lens. If that is not the case, or if the beam is entering sideways, consequently showing an inhomogeneous profile,

the tilting is fixed with screws, until the beam shows uniformity relatively to its radial coordinate.

After the substrate is placed on the stage, the substrate's tilt needs to be checked, both of the substrate's sides relatively to those of the stage (in-plane), and of its own horizontality (tilting angle calibration). The former is relevant in etching from the side, and the latter is important so that every z-plane within the substrate is at the same distance from its surface.

In-plane calibration is done by visual inspection, using the guides in the stage, whereas tilting angle calibration is performed with the aid of the software's dedicated tool [71]. It should be noted that both tilts are generally of the order of the decimal degree, and not zero, due to inhomogeneities within the substrate itself, but that is negligible for most devices to be fabricated.

At this point, it is necessary to determine the effective writing power. Two series of measurements are taken, for different values of the AP: optical power before and after the objective lens. The correlation between these two quantities yields the optical losses induced by the objective, and the correlation between AP and the power after the objective (or effective writing power, P_{W}) provides a calibration factor for the conversion between attenuator programming and ϵ.

In order to determine the position of the stage such that the laser beam is focused on the substrate's surface, the camera's viewing window is activated, along with the coaxial illumination. To be sure that the surface is focused, the laser is momentarily switched on, and the stage is moved along y direction, while varying z until a clear ablation path is viewed. After the surface is found, in terms of the stage's coordinates, the writing may begin, after the area of the substrate has been marked in the viewing window, for an accurate tracking of the laser position.

Finally, after locating all the corners of the substrate, in terms of coordinates in the SCA's frame of reference, the fabrication file can be written/imported in order to start the fabrication.

2.1.2 Chemical etching with HF

Etching with HF is performed at an ISO-5 clean room environment at FCUP.

Being a particularly hazardous chemical species, HF requires special care in handling. Protective gloves, Teflon apron, and protective glasses are essential security measures. The acid is kept at a 10 % concentration in a polyethylene vessel.

The acid is poured into a polyethylene goblet, placed inside another larger goblet for security reasons and to add weight to the system, hence stabilizing it after placing inside an ultrasonics bath at room temperature. It is documented [72] that ultrasounds

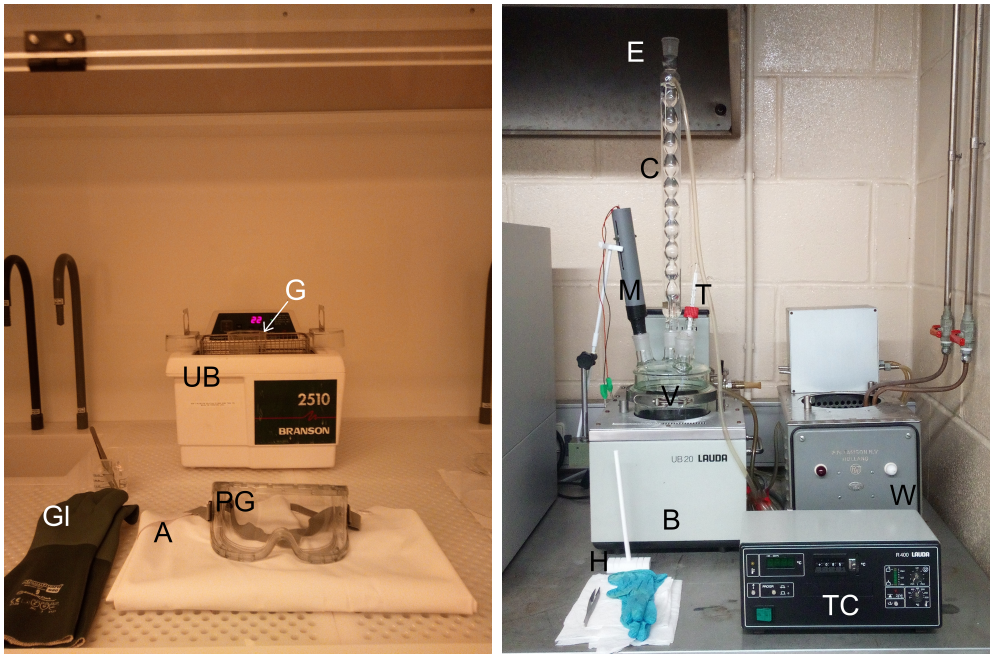

(A) (B)

Figure 2.3: Photographies of the etching setups for: (A) HF etching, comprising the ultrasonics bath (UB), goblet with substrate (G), and protective material (gloves, Gl; teflon apron, A; glasses, PG); (B) KOH etching, comprising the gas exhaustion system (E), Allihn condenser (C), temperature control unit (TC), water cooling unit (W) and bath (B), the motor (M), thermometer (T), reactional vessel (V) and substrate holder (H).

are responsible for the removal of debris, also mitigating the formation of bubbles inside micro-channels [47].

The Branson 2510 ultrasound machine has a timer which is used to set ultrasonics for a predetermined time interval, which is set before placing the substrate in the acid. After an etching period, the substrate is immediately placed in a goblet with deionized water in order to stop the etching reaction, and cleaned with a jet of compressed air before any further processing.

The setup used is shown in Figure 2.3a.

2.1.3 Chemical etching with KOH

As discussed in Chapter 1, the use of KOH as an alternative etching agent provides greater selectivity by increasing the etch rate of modified silica, as well as decreasing the etch rate of pristine silica, when compared to HF [57]. With much lower etch rates than HF, the reaction must be thermally enhanced, by occurring at a higher temperature, usually within the interval .

In spite of the fact that KOH is not as hazardous as HF, special care is required to handle it, in terms of safety and experimental method.

The temperature control was achieved experimentally with an electronically controlled water bath. Inside the water bath, a reactional vessel was placed containing a controlled amount of KOH aqueous solution with an initial concentration of $10\,\mathrm{mol\,dm^{-3}}$. The water's heating is controlled with a feedback circuit that allows to set the final temperature of the bath. An Allihn condenser closes the reactional vessel, serving the purpose of condensing the KOH vapours, thus minimizing any loss of etching agent, while maintaining its concentration. Cooling fluid (water) circulates inside the condenser, from bottom to top, countering the gas' temperature drop with height, and indirectly contacting the hot gas through a glass wall. The cooling water must also be adequately controlled, since a sufficiently low temperature can cause thermal shock and damage to the condenser. Therefore, a water cooling unit is used to cool down room temperature water using the water from the laboratory's plumbing, which is too cool for the condenser to be operated safely.

The temperature gradient in the bath along the direction perpendicular to the laboratory bench was quantified, in order to predict possible consequences in terms of etching inhomogeneity, having been concluded that the maximum variation of temperature from several points at different heights inside the vessel does not exceed $1\,^{\circ}\mathrm{C}$.

The insertion and removal of the substrate holder containing the substrates, from the reactional vessel was performed without switching the system off. This can be done, provided the reactional vessel is made of a material with sufficiently high heat capacity. After removing the holder, the substrate is submerged in a goblet with water, in order to stop the etching reaction.

2.1.4 Substrate polishing

The visualization of transverse sections of micro-channels provides valuable information about the processes through which the etchant penetrates modified silica regions. This visualization can occur directly, with the acid entering through the transverse section, or by focusing through unmodified silica to find the transverse section a couple of tens of micrometres below the surface, a distance which is determined, and limited, by the depth of focus of the optical instrument.

Regardless of the type of visualization, a polishing treatment is always required prior to microscopy, which intends to allow light to penetrate the substrate and/or be focused at its surface. The polishing techniques that were used involve three different polishing suspensions, with successively smaller dimension of the suspended particles. A comprehensive detailing of the steps followed can be found in [73].

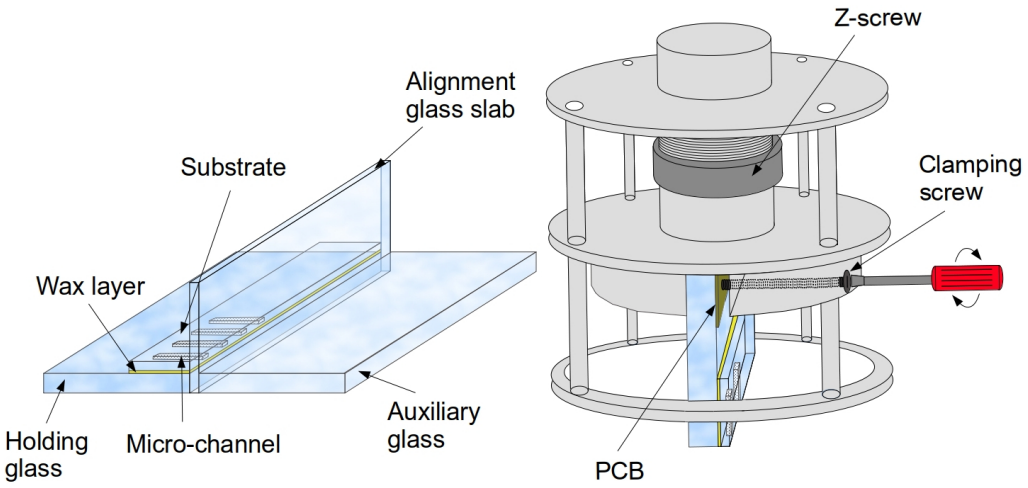

Figure 2.4: Procedure for the alignment of the holder glass and the substrate containing the MF devices (left), and respective placement and clamping to the polishing jig (right).

Firstly, the substrate had to be temporarily glued with a sacrificial layer of previously polished and rectified glass, providing consistency to the whole and avoiding damage to the substrate when clamping it to the polishing jig. After the bonding with molten wax, and subsequent alignment of the surfaces to polish, with the aid of an auxiliary piece of glass and a glass slab in a wedge configuration, the set was mounted on the jig and tightly clamped with a screw using a printed circuit board (PCB) for substrate protection. This procedure for alignment and placement in the polishing jig is schematically represented in Figure 2.4.

The first polishing suspension consists of an aqueous medium and silicon carbide 600-grit powder, with an average particle size of 9 µm. It is the most critical stage in the whole process, due to the risk of the substrate being released from the auxiliary glass and of rupture of either one due to unsatisfactory rectification, and consequent misalignment and tilting of the bottom glass in the jig. After the first stage, lasting about one hour, the section must be inspected for uniformity in the region of interest. Using a 7x magnification microscope, it should be possible to observe some grain in the substrate's section, but the dark gray colouration should be predominant, since incident light is mainly scattered and penetrates poorly into the substrate, as shown in Figure 2.5.

As the substrate is cleared for the second stage, a calcined aluminium oxide suspension is now used, whose suspended particles have an average size of 5.1 µm, computed from the cumulative distribution function for the particle sizes, which is available for consultation in [74], for higher resolution polishing. By the end of the second stage, a higher percentage of light transverses the substrate, and the aspect is still granulous but with a thinner grain.

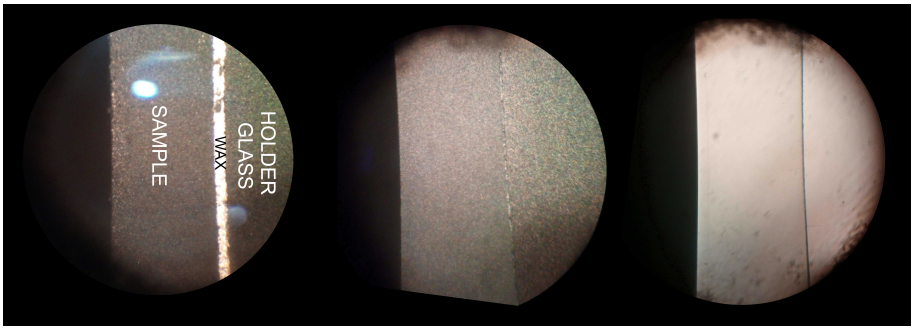

Figure 2.5: Sevenfold magnification image of the same transverse region of the silica substrate, taken at the end of each of the polishing stages described in the text: first with an aqueous suspension of carbide 600-grit powder (left), second with calcined aluminium oxide suspension (center) and third with SF1 suspension (right).

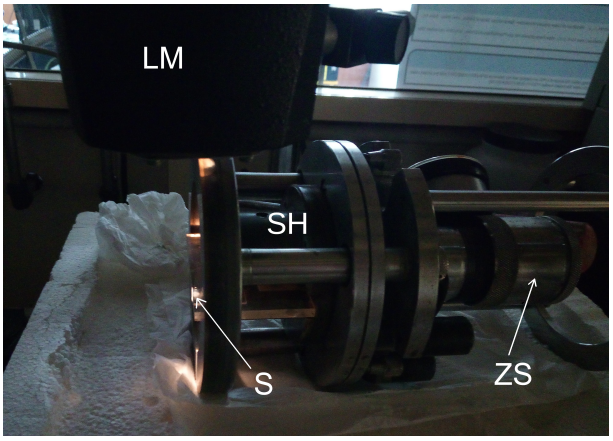

Figure 2.6: Setup used for the analysis of the polishing stages and the removal of material throughout that process. The polishing jig comprises the substrate holder (SH) and the Z-screw (ZS) for lowering and lifting. The substrate (S) is observed via the Leica Microscope (LM).

Finally, in the third plate, the sample is polished with the SF1 suspension, which contains suspended silica particles, removing roughness to the point where the glass becomes polished and fully transparent.

Using the polishing apparatus already described, it was possible to remove material from the silica substrate in order to achieve both a distance of the structures to the section reduced enough to allow microscopic visualization and a sufficiently polished transverse section so as to allow light penetration for the same purpose. The removal of material was monitored by photographing the image from a binocular microscope of the silica substrate upon several times and stages of polishing. Considering that removing the substrate from the jig was not an option until the polishing was finished, due to the extreme position sensitivity of the process, the jig had to be lifted toward the focal plane of the optical instrument, as shown in Figure 2.6.

2.2 A crash course on OpenFOAM®

OpenFOAM® (OF), meaning 'Open-source Field Operation and Manipulation', refers to an open-source computational project comprising a set of numerical solvers, pre- and post-processing utilities, written in C++ and especially dedicated to solving sets of non-linear partial differential equations which govern fluid flows in the context of computational fluid dynamics.

The origins of the project may be traced back to 1989, the date FOAMv1 was presented by two Imperial College researchers, Henry Weller and Hrvoje Jasak, who parallelly published several articles explaining the advantages of 'object-oriented techniques' in computing solutions for hydrodynamic flows. This partnership would, however, be terminated by a dispute regarding the free access condition of the FOAM software, giving rise to the two major project forks: OF by the ESI group and OF by the OF Foundation, each available online with its own elucidative internet domain, .com and .org, and closely related to H. Jasak and H. Weller, respectively.

In what follows, the method on which OF is based will be briefly described, as well as how to set up a case for numerical simulation, and what pre- and post-processing mean in this context.

2.2.1 The finite volume method

Having as predecessors the finite difference method and the finite element method, the finite volume method (FVM) joins them as a valid and widely disseminated alternative for fluid flows' numerical simulation. It owes its existence to the group of Patankar and Spalding, at the Imperial College, back in the 1970s [75].

In FVM, the region of interest is partitioned into a finite number of control volumes, hereinafter referred to as finite volume cells (FVCs) and, as is usual in numerical methods, a discretization scheme is applied to the governing differential equations, while respecting the prescribed conditions for the initial fields and for the boundaries of the computational domain. Additionally, following Gauss-Green theorem, quantities in the conservation equations are turned into fluxes which satisfy algebraic constrains expressing continuity at interfaces between FVCs, and the resulting matrix problem is then solved numerically [76]. Being an inherently conservative method, by enforcing the verification of

$$\partial_t \iiint_{\mathrm{FVC}} q(\mathbf{r},t)\,\mathrm{d}V + \oiint_{\partial\mathrm{FVC}} \phi(\mathbf{r},t)\cdot\mathbf{e_n}\,\mathrm{d}S = \sum_{\substack{\text{sinks}\\ \text{sources}}} \iiint_{\mathrm{FVC}} s_i(\mathbf{r},t)\,\mathrm{d}V \tag{2.2}$$

for flow quantities q, whose flux is ϕ, and whose sources and sinks are identified in the right hand side, it is the preferred alternative nowadays in the computational fluid dynamics field.

2.2.2 Preprocessing: the art of meshing

While FVM is a very powerful method, it heavily relies on some expertise by the operator, both in adequately posing the computation problem, and in defining an 'adequate' computational domain representing the physical volume to be simulated. This conversion is designated as meshing, and the computational representation is called the mesh.

The appropriate design of the computational mesh is of paramount importance in any computational method for physical modelling and problem solving; as such, several checks have to be made in order to obtain an accurate solution. The key aspects concerning the mesh are essentially of two types: internal consistency and case-wise consistency.

The internal consistency checks are deeply dependent on the code structure behind the mesh definition from user defined parameters, as algorithms for the proper evaluation of consistency may be present or not, and these checks can be performed automatically, leaving no room for mistake at the expense of limiting the user's freedom in the mesh generation. In the case of OF, the user must define the geometry by means of listing relevant points in a Cartesian co-ordinate system, which can be used to define computational simulation blocks and areas upon which boundary value conditions will be set. Some of the problems arising from this required pre-processing procedures include the definition of blocks and regions with no regard for the handedness in the definition of the cell's outward pointing normal vector, the mesh mismatch between contiguous regions, the merging of patch pairs that do not share common surface(s), and other specificities of OF meshing.

The case-wise consistency checks ought to be performed by the user, who should be fully aware of the key aspects in computational methods – in the OF case, especially the ones concerning the FVM – and their consequences for the problem in hands. These checks may, thus, be related to an incorrect categorization of faces – for instance, setting a face as a wall when it should be subdivided into three areas, each of a different type –, an inadequacy of the boundary conditions related to unphysical modelling – such as the use of the no-slip boundary condition and the continuum hypothesis in nanofluidic flows [77] –, the definition of computational cells with a significant aspect ratio – which can be the result of uniform gradings' expansion ratio, and which introduces error on the estimation of the velocity field in the directions closer to the plane containing the largest face of the cell –, significant discontinuity in the size of cells in the immediate vicinity of the interface between two neighbouring blocks, in the direction closer to the normal vector of the interface, among others.

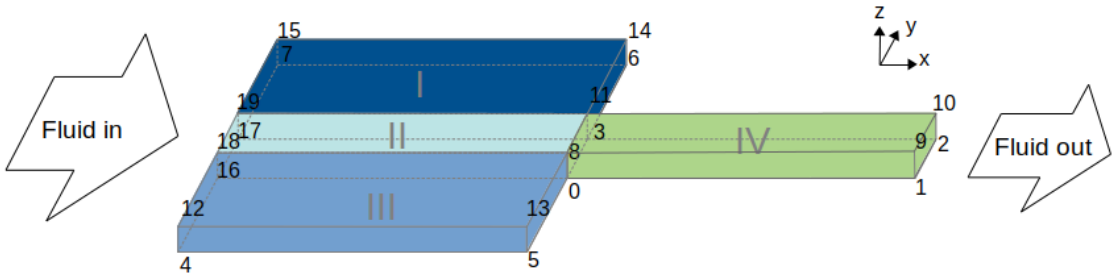

Figure 2.7: Schematic of the MF contraction (the drawing is not to scale), with the numbering of vertices used in the `blockMeshDict` file.

2.2.3 A microfluidic problem solved with OpenFOAM®

The MF contraction is an extensively studied fluid-flow problem. As suggested in Figure 2.7, it consists of a MF channel whose width is variable alongside the coordinate of the flow. Firstly, the height of the channel will be the largest characteristic dimension, mimicking a two dimensional system up as close as possible considering microfabrication achievable dimensions. As will be seen, in OF, the size of the structure is irrelevant if the simulation is 2D. The geometry is represented in Figure 2.7.

In order to pose the problem, from a mathematical point of view, the boundary conditions must be provided alongside the set of partial differential equations. The boundary conditions are provided for the velocity $\mathbf{U}$ and pressure p as follows:

$$\begin{cases} \mathbf{U}|_{t=0} = v_0 \mathbf{e_x} & \text{at the inlet} \\ \mathbf{U}|_{\forall t} = \mathbf{0} & \text{at the outlet and walls} \end{cases} \qquad \begin{cases} p = 0 & \text{at the outlet} \\ \partial_n p = 0 & \text{at the inlet and walls} \end{cases}$$

For the velocity vector field, it is assumed that the momentum relaxation between wall and the fluid in its immediate vicinity imposes the solidarity in the relative motion, which is inexistent if the wall is fixed, hence the designation of no-slip boundary condition, whereas the condition for the inlet results from the statement of the problem. For the pressure scalar field, the zero gradient condition arises naturally from the Navier-Stokes vector equation,

$$\partial_t \mathbf{U} + \mathbf{U} \cdot \nabla \mathbf{U} = -\frac{\nabla p}{\rho} + \nu \nabla^2 \mathbf{U}, \tag{2.3}$$

if one considers an incompressible flow of a fluid with dynamic viscosity ν and density ρ, which must be fully developed in the direction of the flow, and neglecting viscous forces next to the boundaries of the channel. The pressure in the outlet is set by convenience, since only the relative pressure is of interest in this study.

It is now useful to introduce now the Reynolds number, originally suggested by George Gabriel Stokes but made famous by Osborne Reynolds in the end of the nineteenth century. By definition, the Reynolds (Re) number, is defined as

$$\mathrm{Re} = \frac{\text{inertial forces}}{\text{viscosity forces}} = \frac{\rho|\mathbf{U}|L}{\mu}, \tag{2.4}$$

where L and $|\mathbf{U}|$ represent characteristic values for the fluid flow. The importance of Re is the information it contains only by taking average values of those quantities, permitting an insight over the nature of the fluid flow without *a priori* knowledge.

Since the context of Re is historically connected to flows in pipes, the following reasoning provides a consistent definition of Re, while relating it to the convection and diffusive driving phenomena. Supposing a flow with characteristic length L and velocity $\mathbf{U}$, the convective characteristic time t_C corresponds to the time the average particle takes to travel along the pipe: $t_C = L/|\mathbf{U}|$. The diffusive characteristic time t_D is related to the diffusion partial term, which encompasses a relation of the sort $\partial_t\psi = D\nabla^2\psi$. It can be understood as the time that the average particle takes to be diffused from the source to a point L away, in a fluid with density ρ and dynamic viscosity μ (or, alternatively, with kinematic viscosity $\nu = \mu/\rho$): $t_D = \rho L^2/\mu$).

The ratio t_D/t_C equals Re, indicating that low and high Re flows, by comparison with unity, are limited by diffusive and convective mass transfer, respectively, in the sense that those are the processes that dictate the minimum time resolution that is required to evolve a flow from initial conditions.

Re also marks the transition between laminar and turbulent flow, which signify two very distinct regimes: one where fluid streamlines are parallel, well behaved, and another where kinetic energy is transferred from larger length scales to smaller length scales, where it is dissipated onto the fluid internal energy, forming the characteristic whirlwind picture.

2.2.4 Post processing: simulation results

In order to simulate the driving of a viscoelastic fluid, a variation of the uniform velocity profile was used as a boundary condition to start the simulation. Particularly, it was considered that $u(t) = 1/8(1 - \cos(\pi t))\mathrm{m\,s^{-1}}$, for $t < 1$, and $u(t) = 0.25\,\mathrm{m\,s^{-1}}$ for $t \geq 1$. The viscoelasticity admitted was small, characterized by a time constant of $\lambda_{\mathrm{VE}} = 1 \times 10^{-5}\,\mathrm{s}$, and the constitutive properties used were selected in order to achieve the desired Re.

The computational mesh is found in Figure 2.8. The visualization of the pressure and velocity fields provide only a part of the picture related to the fluid flow. Using the Stream Tracer tool provided by Paraview, it is possible to simulate the seeding of a

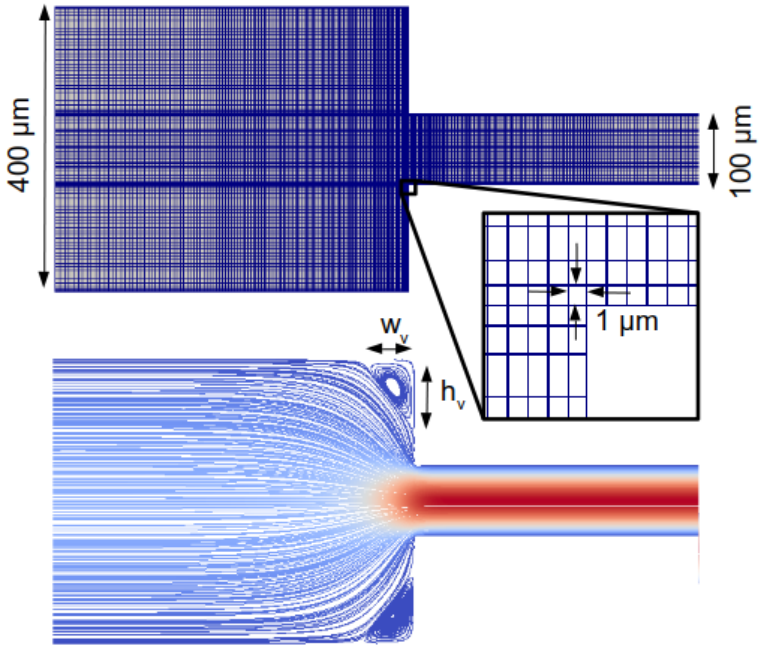

Figure 2.8: Representation of the computational mesh and important lengths of the planar 4:1 microfluidic contraction, with a detail of the corner region (top) and flow lines for the case of Re=1 after reaching the steady state.

defined number of particles in a volume of the computational domain, and follow their path by numerically integrating with Runge-Kutta methods the motion equations: the paths generated this way correspond to the stream lines of the fluid flow. What occurs with the microfluidic contraction is the appearance of vortices, designated by Moffatt vortices, in the corner regions (depicted in Figure 2.8), with associated lengths w_v and h_v (side and top lengths, respectively).

Using a routine written in the `controlDict` file, it is possible to access mesh data as the simulation is carried out. In particular, one may access the velocity profile at the two walls with which the Moffatt top vortex contacts (the bottom vortex could also have been used), and compute the point at which the u component changes sign, thus associating with it its streamwise and normal lengths. To illustrate the change in the length of these vortices over time, five simulations were carried out, with $\mathrm{Re} \in \{0.001, 0.01, 0.1, 1, 10\}$. The density, instead of the average velocity, was what was changed between simulations. The results for these simulations are shown in Figure 2.9. It can be observed the asymptotic al tendency for the stabilization of the vortices lengths, albeit for values depending on the Re. With increasing Re, since the flow is simulated from the large to the small channel, as long as the regime is far from turbulence, it is expected that the residence time of the fluid near the corners of the contraction should increase, due to the necessary change in direction required in an inertia dominated regime.

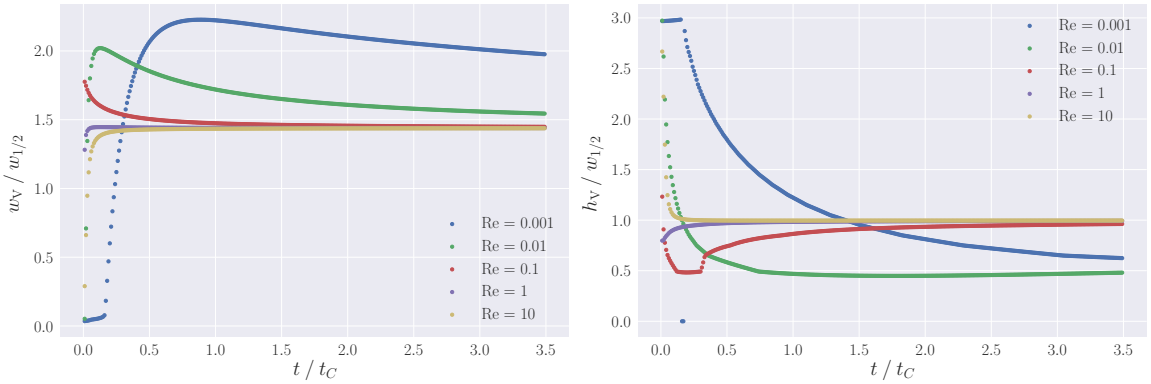

Figure 2.9: Moffatt vortices side (left) and top (right) lengths normalized to the narrow channel half-width as a function of time measured in units of the convective time.

Further details relatively to the meshing of the contraction for simulations and to the fabrication of the device with the FLAE technique are accessory to the main work developed, and are thus left for Appendix A.

2.3 Experimental realization of microparticle image velocimetry

The verification of the numerical (and analytical, whenever possible) solutions of the fluid flow in microfluidic devices (MFDs) is heavily dependent on the existence and reliability of an experimental method for the determination of some of the fields representing characteristic physical quantities. The Navier-Stokes (NS) equation relates the material derivative of the velocity field to all the forces present in the fluid, and has an explicit dependence on the pressure and velocity fields, for instance.

Therefore, it would be natural to try to evaluate the pressure field at certain positions in the fluid, but those are complicated measurements, and the repeatability throughout the fluid quickly becomes a tedious, unpracticable task. Fortunately, the most interesting field in the NS equations is the velocity field, which is usually measured via particle image velocimetry. In as early as 1904, Ludwig Prandtl, possibly inspired by how electromagnetic field lines can be visualized with iron fillings, was experimenting with mica particles on the surface of the water, in order to visualize streamlines in his water tunnel.

This qualitative technique is the basis for what happens nowadays with microparticle image velocimetry (μPIV). The sophistication lies in the word 'Velocimetry', that is, the post processing that can be performed in order to recover the velocity field of the particles in a MFD. This post-processing consists of correlating pairs of pictures taken at consecutive time instants (in fact, up to the time step δt) of the tracer particles' positions, in order to

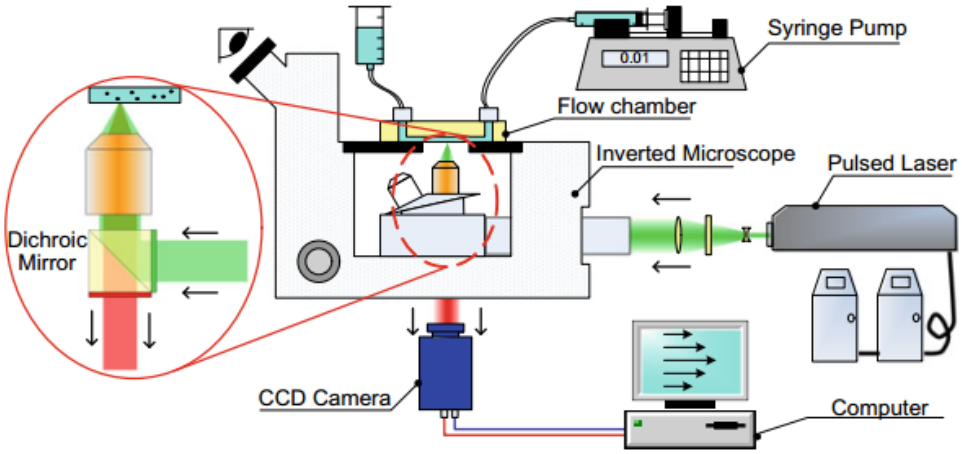

Figure 2.10: Experimental setup for a PIV experiment [78]: tracer particles are mixed with the test fluid, which then is injected into the device, flowing through the examination region, which is illuminated with laser light at specific time intervals, for image capture, followed by mathematical treatment for velocity extraction.

extract the displacement vectors, to which a differentiation scheme is applied in order to recover **U**.

The stages of a simple μPIV experiment are depicted in Figure 2.10, and will now be further detailed below.

2.3.1 General considerations

In order to reduce the adhesion of tracer particles to the PDMS top wall of MFDs, sodium dodecyl sulfate (SDS), an anionic surfactant, can be added to the solution with the tracer particles. The use of this compound is documented with non-Newtonian fluids for μPIV experiments, with mass concentrations of 0.05 %, with no significant effect in the shear viscosity of polyacrylamide solutions with 1% of sodium chloride [79].

μPIV experiments with water as a Newtonian fluid will also benefit from the addition of SDS, especially if the tested micro-channels are prone to particle aggregation and clogging due to their almost nanometric size. Based on Niraula *et al.* [80], no rheological alteration is predicted on the aqueous solution for SDS weight percentages in the range between 0.18 and 0.38. It was chosen to use the weight percentage of 0.38 %.

The operation modes that are frequently used in μPIV will now be defined, regarding how frequently and in what manner pictures of the tracer particles are taken. First of all, two distinct reasons contribute to the importance of a good understanding of the image acquisition part: firstly, limitations regarding the optical system are to be expected and must be accounted for, and secondly, the very possibility of a successful cross-correlation relies on the choice of an appropriate time lag between acquired frames.

The microscale flow requires both a microscope for magnification and a camera for image acquisition. Both these optical devices are subject to the laws of Optics, which predict the occurrence of optical aberrations and of a depth of field in the image formation process.

Ideally, light should be focused in a thin plane, the object plane, and the image one sees in the microscope corresponds to that same plane. However, due to diffractive phenomena which cause the focal plane to degenerate into a focal region of height equal to twice the so-called depth of field, particles at a distance from that plane are imaged with a certain (albeit lower) intensity, contributing to the velocimetry. The depth of correlation δ_z^{corr} is, thus, the radius of the planar neighbourhood of the focal plane inside which the particles' intensity is sufficient (that is, larger than a given threshold fraction ϵ of the object-plane intensity) to be (erroneously) accounted for, by the algorithm, just like truly focused particles. Within paraxial optics, an expression can be derived [78] for the depth of correlation,

$$\delta_z^{\text{corr}} = \sqrt{(\epsilon^{-1/2}-1)\left[\frac{d^2((n/\text{NA})^2-1)}{4}+\frac{1.49(M+1)^2\lambda^2((n/\text{NA})^2-1)^2}{4M^2}\right]}, \tag{2.5}$$

admitting that $\delta_z^{\text{corr}}/s_o \ll 1$, where s_o is the object plane's distance to the lens, d is the diameter of the spherically-modelled tracer particles, and M is the total magnification.

Regarding the choice of the time between frames, δt, there is an intimate relation that must be obeyed by both this quantity, and the length of the interrogation area (IA) in a certain direction. Considering that the unit interrogation cell has a length of δx_i along $\mathbf{e}_{\mathbf{x_i}}$, the time between pictures must be chosen in a way such that the maximum displacement of a particle in the fluid does not exceed $c\,\delta x_i$, where $0 \leq c \leq 1$ (for the current μPIV system, $c = 0.25$). Mathematically, one must require that

$$t_F \leq \min_i \left\{ \frac{0.25\,\delta x_i}{U_i^{\max}} \right\}. \tag{2.6}$$

This estimate ensures that the algorithm used for the computation of the cross-correlation between successive frames is successful, and that velocity profiles can be extracted *a posteriori*.

Finally, the operation of photographing the flow must be addressed, since there is not one method for this acquisition, but a combination of the multiplicity in frame acquisition (MFA) with the multiplicity in exposure (ME). As is known, the PIV is performed by repeating the acquisition procedure with a certain periodicity δt in time, in order to capture the tracer particle's motion. What differentiates these modes is the way a single acquisition is performed (see Figure 2.11):

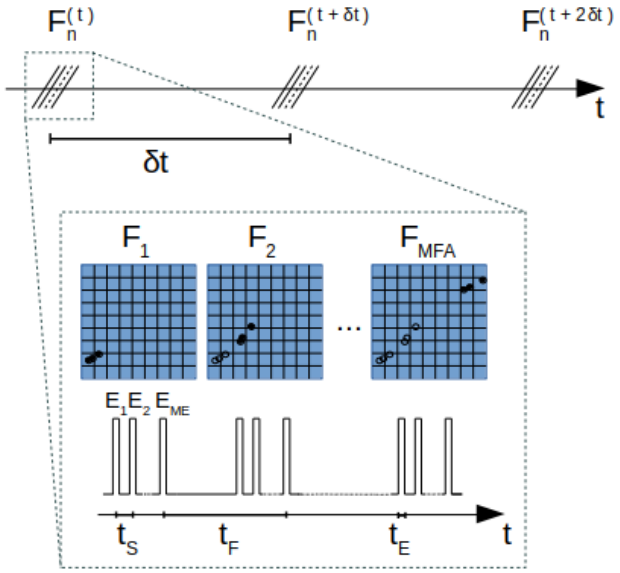

Figure 2.11: Scheme of the acquisition process in a μPIV experiment, where t_E represents the time associated with one exposure, t_S the time between consecutive exposures within the same frame, F_n^t represents a set of frames starting at time t, and E represents an exposure. In general, $t_S = \mathrm{ME}t_F$, that is, when the exposures reach the defined number of exposures per frame, the software 'opens' a new one immediately.

- MFA corresponds to the number of frames that are used in this acquisition: either MFA=1 (single frame mode, where the same picture contains all information acquired within the individual measurement, that is) or MFA>1 (multi frame mode, where information is split through several pictures, taken with a time separation of t_F);

- ME corresponds to the number of times that the camera's shutter is opened, allowing for the capture of images: either ME=1 (in single frame, the picture lasts for a certain $\delta t_S F$, and the particle's trace is visible just like moving cars seen from above at night, and in multi frame, the shutter is opened MFA times) or ME>1 and the shutter is opened MFA times per frame, resulting in the same particle being depicted in the same frame.

Generally speaking, $t_E < t_S < t_F < \delta t$. A double frame configuration is extremely helpful in the detection of transient behaviour, especially as the time between exposures[1] turns to one millionth of a second, the exposure time to a hundreds of nanoseconds, and it becomes possible to obtain a velocity profile which is itself changing rapidly with time.

[1]It is worth mentioning that the photographer's frame rate, and its reciprocal, the time between frames, are in this text referred to as exposure rate and time, respectively, the designation frame rate being reserved to the PIV frames, which in fact are collections of frames with multiplicity ME.

2.3.2 Experimental method

In what follows, the adopted methodology and devices used to extract μPIV data is presented. Firstly, the device is manually filled with the test fluid using a plastic syringe and a Tygon connection pipe, which is connected to the device and to the plastic syringe using inner diameter/outer diameter equal to 0.41 / 0.72 mm Nordson Optimum® stainless steel general purpose tips.

Polystyrene fluorescent tracer particles are available for μPIV with three different average sizes: 0.5, 1, and 2 μm. Those particles are Nile Red by Invitrogen Molecular Probes. Throughout this work the 2 μm particles were used. A glass syringe (or syringes, if the device has more than one inlet) is also filled with the test fluid and connected to the empty side of the Tygon pipe. Finally, it is placed in the syringe pump and locked in place. Using the graphical user interface (GUI) provided by Cetoni, the syringe is selected from an available list or user inputted (its stroke, capacity, and radius), the desired flow rate is programmed and the pump becomes ready to start.

The MFD is placed in the stage of the microscope and, after being placed in an adequate position for flow visualization, fixed with tape, and the camera is rotated until the desired alignment is obtained and afterwards screwed in that position.

In the software Dynamic Studio, the MFD is visualized and, at first, a mask is defined. The mask serves the purpose of removing areas of the fluid flow which are prone to degrade the quality of the cross-correlation for the computation of the velocity map. These areas are typically the side walls of the microchannel.

The operation mode is defined, along with the time interval between pairs of frames and between frames. The possible modes of operation with the available system are single frame mode and double frame mode, both with ME =1. A preview is then generated, in order to verify if the flow is indeed occurring as predicted and if there are visibility conditions for a good cross-correlation (namely, if the particles are not moving too fast for the IAs used, as discussed above).

The number of pairs of frames (or of frames, if in single frame mode) to be taken is decided by the user. All light sources are either shut, kept occluded or far away from the μPIV experiment area, since they act as a source of contamination. In order to mitigate the occurrence of reflections in the sample, from the white light source, the microscope is tilted back. Finally, the temperature must be set in the air conditioning system, and measured if it is possible (next to the test fluid) in order to have accurate control over all rheological properties.

The laser system is enabled, and so is the pump, and finally the shutter. The use of protective goggles is mandatory during this stage. The syringe pump is then activated, and the acquisition may begin.

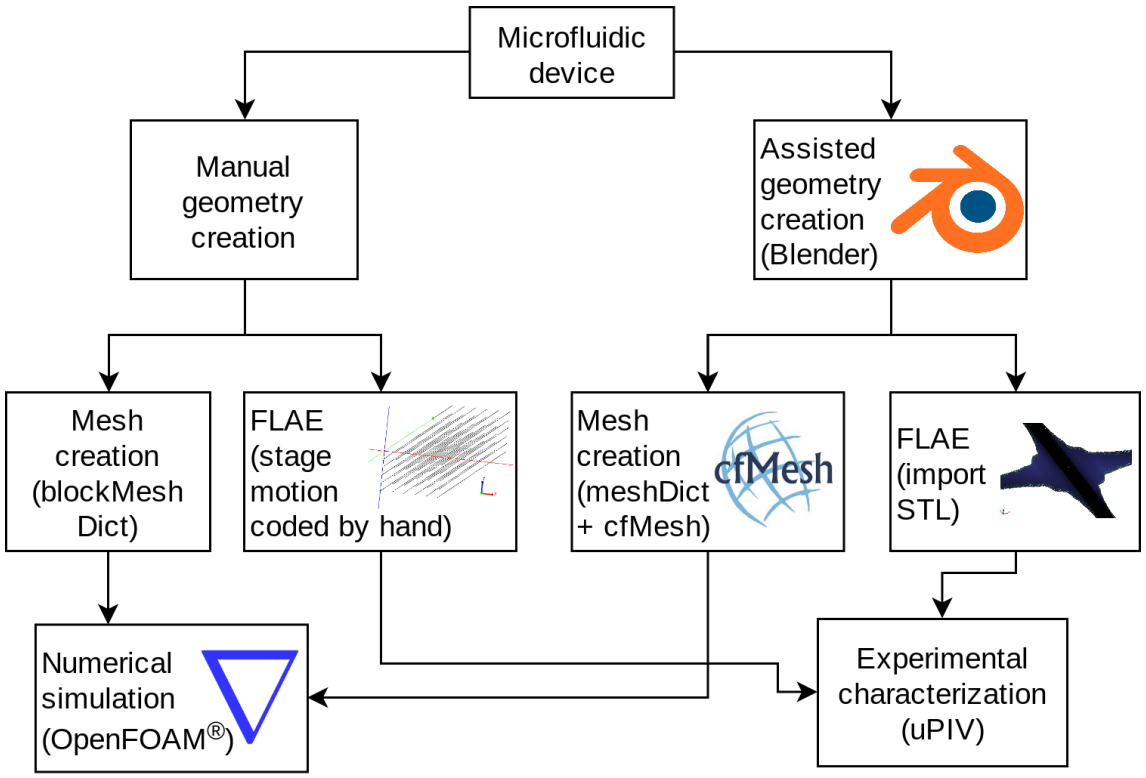

Figure 2.12: Workflow and synergy between the three techniques used in this work.

Recapitulating, this chapter is focused on the exposition of the theoretical background and experimental methods employed in this work. The finite volume method was presented as an inherently conservative method for computational fluid dynamics, and contextualized in terms of OpenFOAM®. Femtosecond laser assisted etching is further detailed relatively, featuring a brief explanation of the optical components required for localized laser irradiation and stage control, and of the setups used for etching with HF and KOH. Finally, the microparticle image velocimetry is presented as an Eulerian measurement based technique for the interrogation of the particle's subsequent position through an optimized average correlation of the restriction of an ensemble to an interrogation area, and the procedures and generally accepted rules of thumb for its successful application are discussed.

This work exploits the synergy between the three methods discussed above, one numerical method, one microfabrication method and one experimental characterization method. Figure 2.12 represents this idea in the form of a diagram, where the path in the left side was taken in Chapter 3, and the path in the right side in Chapters 3 and 4.

Chapter 3

The microfluidic channel

This chapter is concerned with simulations, fabrication procedure, and experimental characterization of the fluid flow in simple microfluidic channels. Using OpenFOAM®, the flow in straight microchannels is simulated and compared with the known analytic solution for a pressure driven flow with no slip boundary conditions.

The simulated channel is fabricated using the FLAE technique, and writing parameters such as writing depth, velocity, scan spacing, type of meshing, and energy per pulse are characterized and optimized to ensure fidelity of the process. Threshold fluences for optical damage are also determined. Finally, the numerical solutions are compared with μPIV data.

3.1 Analytic solution

Under no slip boundary conditions, the flow in a stationary regime inside a duct of an arbitrary shape can be reduced to a Dirichlet problem, for which analogous solutions are found in electromagnetic theory, for instance. Some of those results are stated in White's reference book [81] and references therein, namely the steady state velocity profile and flow rate for the case of the paralellepipedic channel with transverse section dimensions of W and H (for convenience, we assume a frame of reference such that the origin is one of the vertices of the transverse section, which is fully contained in the first quadrant).

The exact, analytic solution to the differential problem

$$\begin{cases} \triangle U(x,y) = \frac{\Delta_{p/x}}{\mu} & \text{, in } \Omega = \{(x,y) \in \mathbb{R}^2 : 0 < x < W \wedge 0 < y < H\} \\ U(x,y) = 0 & \text{, in } \partial\Omega \end{cases} \tag{3.1}$$

is given by the power series presented in Equation 3.2. The flow rate Q is obtained by integration of the velocity profile in the control area, the transverse section Ω.

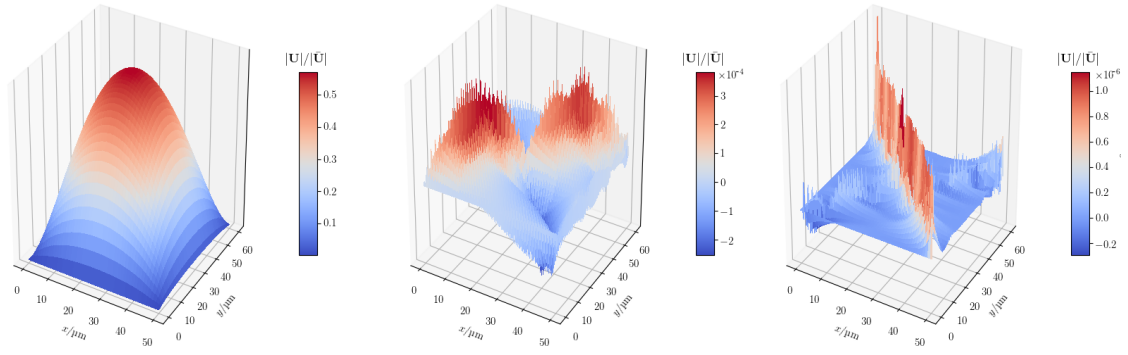

(A) (B) (C)

Figure 3.1: Representations of (A) analytic solution for the flow in a channel with square cross section with $W = 50\,\mu\text{m}$, first (B) and second (C) order corrections using perturbation theory on one side of the boundary, with the perturbation function $h(x) = \sin(2\pi/0.005x[\mu\text{m}])$, and perturbation magnitude $\epsilon_r = 0.1$.

$$U(x,y) = \frac{4W^2}{\mu\pi^3}\Delta_{p/x}\sum_{n\text{ odd}}(-1)^{(n-1)/2}\left[1 - \frac{\cosh(n\pi(y-H/2)/W)}{\cosh(n\pi H/2W)}\right] \times \frac{\cos(n\pi(x-W/2)/W)}{n^3} \tag{3.2}$$

$$Q = \frac{HW^3}{12\mu}\Delta_{p/x}\left[1 - \frac{192W}{\pi^5 H}\sum_{n\text{ odd}}\frac{\tanh(n\pi H/2W)}{n^5}\right] \tag{3.3}$$

The solution above, which is valid only if the fluid is Newtonian, is a function of position (only for the magnitude of velocity, though!) and of geometric and constitutive parameters, apart from $\Delta_{p/x} = -\,\mathrm{d}p/\,\mathrm{d}x$, which is imposed by the analytic separation of variables method to be a constant. The series converges rapidly, and it poses no difficulty to obtain a truncation which satisfies a predefined relative accuracy.

The flow rate can be imposed at the beginning of the duct, whether computationally, in OF, or in real experiments, which permits the determination of the pressure gradient. On the other hand, by accessing the velocity profile, namely along a central streamline, it is possible to determine, empirically, the value of the pressure gradient.

The relation between $\Delta_{p/x}$ and the flow rate is linear, and so is the relation between the velocity at any given point, and $\Delta_{p/x}$. Therefore, the analytic solution can be normalized by the average velocity, which is related to the flow rate by $|\bar{\mathbf{U}}| = Q/(LW)$. Figure 3.1a represents a plot of the normalized velocity magnitude in the cross section of a $50\,\mu\text{m}$ wide micro-channel. The velocity norm is always greater in the centre of any constant x or constant y plane, and the largest velocity occurs at the centre of the micro-channel. Numerical calculations show that this global maximum velocity $|\mathbf{U}_\text{M}| = U(W/2, H/2)$ is always 2.096 times greater than $|\bar{\mathbf{U}}|$.

3.1.1 Perturbation methods of the channel's cross section

In order to take into account the effect of channel roughness, a first attempt consists of using perturbation theory in order to relate a small perturbation in one of the boundaries of the channel, with a characteristic amplitude of ϵ, to its effects on the velocity profile of the steady-state flow then established. We begin by modelling the roughness in one of the sides of the rectangular domain with a sinusoidal perturbation of amplitude ϵ.

Following the approach suggested in [82], the differential problem expressed in Equations 3.5 is solved, only with a slight alteration to include the perturbation function h:

$$\begin{cases} \triangle U(x,y) = \frac{\Delta_{p/x}}{\mu} & \text{, in } \Omega_{\epsilon_r} = \{(x,y) \in \mathbb{R}^2 : 0 < x < W \wedge 0 < y < H(1 - \epsilon_r h(x))\} \\ U(x,y) = 0 & \text{, in } \partial\Omega_{\epsilon_r} \end{cases} \tag{3.4}$$

In the determination of the analytic solution to the problem stated in Equations 3.4, by using the theoretical calculations presented in the referenced paper, it was necessary to solve a different Laplace differential problem for each correction term to the unperturbed problem, after which the solution is accurate up to a larger integer power of ϵ (just like a regular power series expansion). In order to solve a differential Laplace problem of the sort of

$$\begin{cases} \triangle U(x,y) = -\phi(x,y) & \text{, in } \Omega_R =]0, W[\times]0, H[\\ U(x,y) = 0 & \text{, in } \partial\Omega_R, \end{cases} \tag{3.5}$$

we recall the Fourier expansion of a two-variable function ϕ, which decomposes the source function into its sinusoidal components in both variables, with weights B_{nm} for the n-th harmonic in x and m-th harmonic in y. It can be shown [83] that to the problem in Equations 3.5 is

$$U(x,y) = -\pi^{-2} \sum_{n\geq 1} \sum_{m \geq 1} \frac{B_{nm}}{(n/W)^2 + (m/H)^2} \sin(\frac{n\pi x}{W}) \sin(\frac{m\pi y}{H}), \text{ where} \tag{3.6}$$

$$B_{nm} \equiv \frac{4}{HW} \int_0^W \mathrm{d}x \int_0^H \mathrm{d}y \, \phi(x,y) \sin(\frac{n\pi x}{W}) \sin(\frac{m\pi y}{H}). \tag{3.7}$$

Using Mathematica, it was possible to circumvent the need to compute cumbersome integrals symbolically. The results thus obtained were adapted into Python and the series in Equations 3.2, 3.3, and 3.6 could then be truncated at an appropriately defined number of terms.

Considering that the inspected roughness was repeated at the bottom of the MF channel, it was modelled as a sinusoidal perturbation of period and amplitude both equal to 5 µm, which resulted in $\epsilon_r = 0.1$. Finally, upon having an adequate model, and using the method described above, we obtained first and second order corrections to the velocity profile, which are represented in Figures 3.1b and 3.1c, respectively.

3.2 Solution obtained with OpenFOAM®

3.2.1 Microfluidic channel with square cross section

This test with OpenFOAM® consisted of the simulation of an unperturbed flow through a perfectly rectangular cross-section duct.

The same principles applied in the discretization of the MF contraction described in Appendix A were adapted for this discretization, namely, the tighter mesh near the corner regions of the cross section, and looser next to the core of the section. However, a different approach was followed: instead of defining the mesh size next to the corner regions, l_{min}, along with the geometrical parameter total length L of the cross section and the numerical parameter number of cells N, we decided, instead, to set the length of the channel to be used with the compressed mesh L_{cp}, as well as the number mesh size in the center and corner regions, in order not to have very accentuated differences between these quantities, for the sake of the numerical method's accuracy.

If l_{max} represents the length of the final cell, l_{min}, the length of the initial cell, L corresponds to the length spanned by all the N cells in the grading region, and $0 < r < 1$ to the ratio of the geometric progression, closed expressions can easily be derived for r and N. Further details about the derivation can be found in Appendix B. The geometry parametrization block is pretty straightforward, just like the vertices definition, which describe one single FVC.

In the longitudinal direction, we chose to expand the FVCs' length in a fraction of the full length of the channel, followed by an uniform mesh with the spacing as close as possible to the latest in the geometric progression. As about the mesh parameters, we define a fraction of the width (y direction), which will correspond to a length of expansion, where a graded mesh will be used, and compute the corresponding length by multiplying it by the width. With the aid of a coded function, we obtain the number of cells in expansion `Nc*`, the corrected expansion length `L*corr` and the expansion ratio required by OF `er*` – the asterisk is to represent both directions y and z.

Furthermore, the length of the uniform portion is computed considering one wishes for an expansion, followed by uniform meshing and a contraction towards the opposite wall. The total number of cells in each direction `N*` is found by adding twice the number of cells

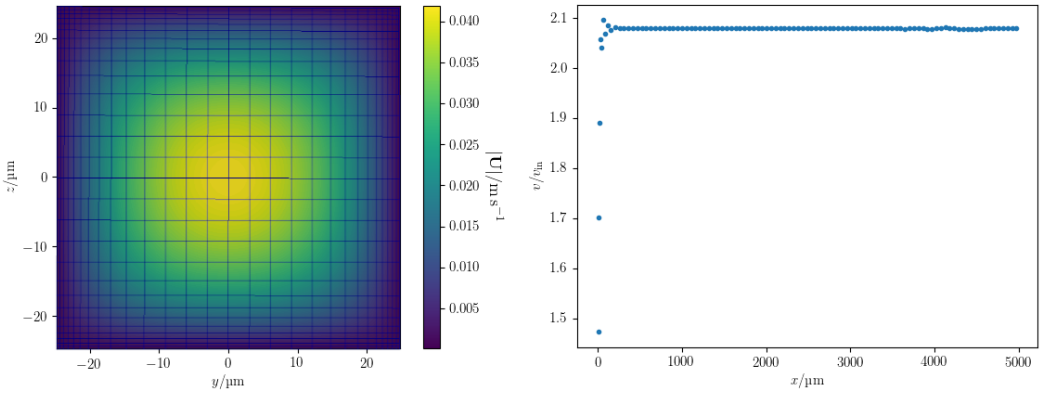

Figure 3.2: Simulation results for the simulated micro-channel, showing the velocity profile in a fully developed flow zone superimposed to the computational mesh (left), and the variation, with the streamwise coordinate, of the velocity at the centre of the microchannel, normalized to the average velocity (right).

in the compression/expansion region to the number of cells in the uniform region. The latter is computed by rounding the ratio of the length of the uniform region to the corrected maximum length of the last cell in the expansion region. The definition of boundaries is identical to the case of the contraction, discussed in Appendix A, but for a slight change in two of the channel's boundaries, which are now treated with the keyword `wall` instead of `empty`. This means that the simulation will now be treated as three dimensional, or, in other words, the y and x dimensions will be of appreciable magnitude compared to the height of the channel.

Considering the analytic solutions for this problem, already described, the simulation was carried out with the adequate boundary condition using the OpenFOAM® solver for Newtonian, incompressible fluids (`icoFoam`). The simulated fluid is water, with the constitutive parameters taken from table values at a temperature of 22 °C, and the initial and boundary conditions were the same as for the contraction, except for the velocity at the inlet which was set as $0.02\,\mathrm{m\,s^{-1}}$. The simulation results are presented in Figure 3.2.

From comparison with the known analytic solution, it is verified that there is an agreement between the velocity profiles, and that the relation between the centre velocity and the maximum velocity is as prescribed in Section 3.1.

3.2.2 Incorporation of roughness

The impact of roughness in pipe flows is given by the Moody diagram, which relates the friction factor, relative roughness ϵ_r, and Re. The existence of areas in Moody's chart suggests that the impact of roughness in null up until $\mathrm{Re} = \mathrm{Re_c}$, the critical transitional Re between fully laminar and conjoint flow. Moody's chart is the extension, in terms of Re number, of the pioneer work of Johann Nikuradse's with circular pipes to whose

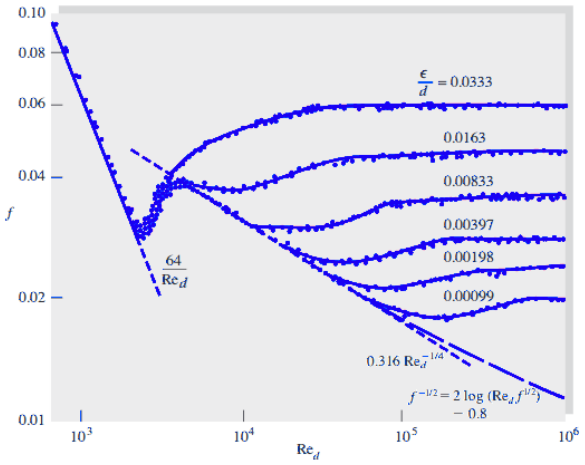

Figure 3.3: Experimental points measured by Nikuradse [84], showing the lifted degeneracy of the friction factor $f = H/\left(\frac{L}{d}\frac{|\mathbf{U}|^2}{2d}\right)$ dependence on the relative roughness by the increase in the Re defined from the pipe diameter d.

walls he glued sand grain of different sizes, before studying laminar and turbulent flow inside them. His results are shown in Figure 3.3. The possibilities of simulating sand-grain roughness in OpenFOAM® were explored, by using a k-ω modelling of viscoelasticity, and varying the parameter corresponding to the relative roughness in the boundary layer patch `nutKRoughWallFunction`. Since the simulation was set for creeping flow at a sufficiently low Re number (of below unity), it was verified that no alteration was produced in the numeric simulation.

3.3 Description of the fabrication method

The volumetric objects to be written inside the glass substrate are obtained by moving the substrate in each of the three main directions an arbitrary distance limited by the stage resolution. The fabrication files must contain instructions to move the xyz linear stages where the substrate is placed, and so, for instance, focusing on the substrate surface and moving the stage upwards is equal to writing below the initial position. Furthermore, due to refraction of light in the interface between air and the substrate, the stage displacement in z, h_s, and the corresponding displacement of the focal volume, h_fp, are not the same; in fact, they are related by $h_\mathrm{s} = h_\mathrm{fp}/n_{\mathrm{SiO}_2}$, where n_{SiO_2} is silica's refractive index. This means that if a h_fp is meant to be the spacing between layers of scans parallel to the xOy plane, the stage should be programmed to be elevated of h_s.

Figure 3.4a represents the orientation of nano-gratings formed in fused silica as a function of the scanning direction, electric field (polarization), and incident wave-vector. When etching occurs in the direction represented by the green arrow, the nano-gratings are

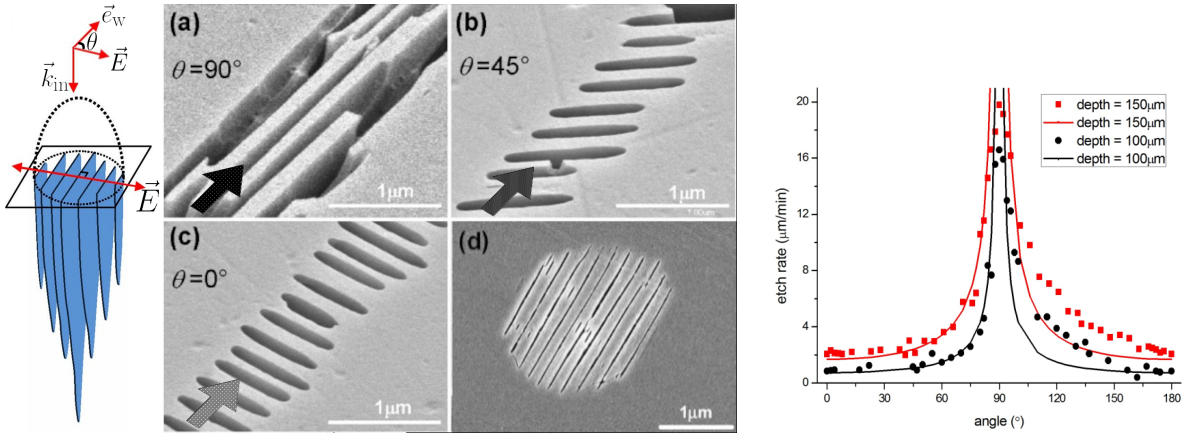

(A) (B)

Figure 3.4: Mechanisms for the variation of the etch rate with the linear polarization angle: (A) Photograph of a voxel and nanogratings [85] oriented perpendicularly to **E** (left) and respective SEM image (d), along with structures formed after scanning along $\mathbf{e}_w$ for several polarization angles (a)-(c) and 20 min in 0.05 % mass concentration HF [86] (arrow darkness proportional to respective etch rate); (B) experimental verification of etch rate dependence on the angle between **E** and $\mathbf{e}_w$ (courtesy of J. Maia [47]).

oriented favourably to etching penetration, thus etch rate is high, whereas when occurring in the direction represented by the red arrow, the etchant finds layers of modified material interleaved by layers of pristine material, thus etch rate is low.

Throughout the fabrications described in this Chapter, the polarization was kept linear and oriented perpendicularly to the direction of writing, leading to the maximization of the etch rate when the etchant enters alongside the writing direction. In fact, the theoretical dependence predicts a divergent behaviour, typical of a pure resonance, to which is added damping, in practice, due to the quantum nature and uncertainty in polarization. For all practical purposes, we assume that there is a non-diverging maximum, as Maia [47] verified and quantified with an increment of 1000% relatively to the case of collinearity between polarization and scanning direction, represented in the plot of Figure 3.4b.

If writing in all three dimensions, it is preferable to do so by starting from the lowest part in the structure and lowering progressively the stage, so as to avoid laser exposure through the already exposed material to prevent distortions. In Figure 3.5b, a channel is outlined with the preview generated by SCA. Each black line represents one laser scan. Between consecutive lines in the routine, a jump occurs with the laser firing interrupted. Each plane parallel to xOy is written before moving to the one below (lowering the stage means writing above the current position), and, within one plane, the scans follow in sequence, from left to right, with unidirectional writing, that is, with only one laser pass per scan – in the same figure, along the positive x axis.

If writing is successful, the final laser z position should be the one corresponding to the

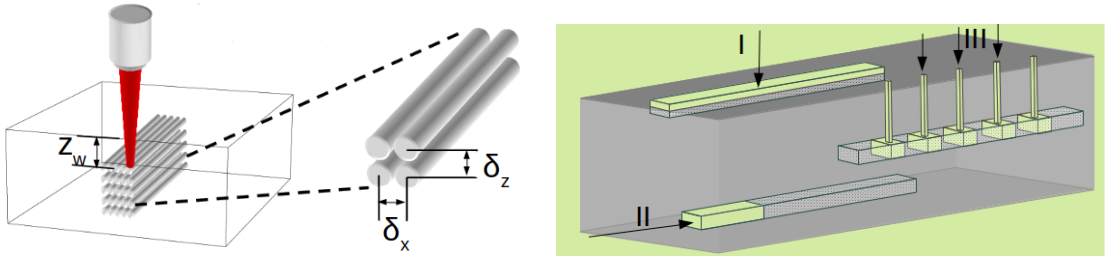

(A) (B)

Figure 3.5: Sequence of methods of which the FLAE technique is comprised: (A) Simple outline of a micro-channel by laser exposure along the axes of the cylinders, which represent the focal volume (after [87]); (B) Three different types of etching, considering the position of the channel inside the silica substrate – etching from the top facet (I), from the side facet (II) and through access ports connected to the surface (III).

substrate's surface, so that laser ablation can occur. This is important since, if the etchant is not in direct contact with modified areas, it must etch through pristine silica, and the associated etch rates are of about $7.8\,\mu m\,h^{-1}$ (HF) and $400\,nm\,h^{-1}$ (KOH), resulting in long waiting times for the selective etching to start.

Two types of etching were performed in the course of this thesis, etching with and without access ports. Etching without access ports requires that one of the fabricated structure's facets is fabricated in direct contact with one of the substrate's facets, in order for the acid to be able to penetrate the modified silica region. In this case, the facet of the substrate used was either the surface (top face) or the side. On the other hand, etching with access ports occurs when the structure is completely integrated in the substrate, and much smaller access channels are fabricated from it to one of the substrate's facets. These etching procedures are represented schematically in Figure 3.5a.

3.4 Study of the graded meshing scheme

A graded meshing scheme, as opposed to a uniform meshing scheme, consists of laser scans which are not equidistant. Figure 3.6 represents the difference between the configurations of eleven laser beams using a graded and a uniform writing scheme. In order to assess the influence of the writing scheme in the etching process, and consequently, in the fidelity of produced microchannels, twelve micro-channels were fabricated.

The graded schemes fabricated consist of three regions (see Figure 3.6): first, laser scans are engraved with progressively larger spacing (region 1), then follows a region of evenly spaced scans (region 2), and finally, follows the mirror image of the first region, with laser scans progressively closer to each other (region 3). These regions are uniquely defined by three parameters, L_m (smallest scan spacing in regions 1 and 3), L_M (largest

scan spacing in regions 1 and 3), and L_e/W (ratio of the expansion/contraction region to the channel width), while trying to keep the laser spacing in the uniform region as close to L_M as possible (this determines the total number of scans).

These channels were fabricated with $\epsilon = 100\,\text{nJ}$ per pulse, writing velocity of $v_\text{w} = 500\,\mu\text{m}\,\text{s}^{-1}$, and the laser polarization perpendicular to the scanning direction. All channels feature a height equal to the width and equal to 20 µm (four channels) and 50 µm (eight channels). The geometric parameters L_e/W, L_m, and L_M were varied, with the test values being

- for the four $W = 20\,\mu\text{m}$ micro-channels, $L_e/W = 0.45$, $L_m \in \{1, 3\}\mu\text{m}$, and $L_M \in \{4, 5\}\mu\text{m}$;
- for the eight $W = 50\,\mu\text{m}$ micro-channels, $L_e/W \in \{0.3, 0.4\}$, $L_m \in \{2, 4\}\mu\text{m}$, and $L_M \in \{5, 8\}\mu\text{m}$.

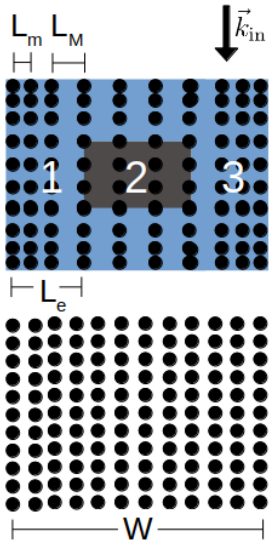

Figure 3.6: Comparison of graded and uniform writing schemes. $\mathbf{k}_\text{in}$ represents incident wave-vector.

Among these, three channels were approximately uniformly meshed, that is, $L_\text{min} \approx L_\text{max}$, hence serve as control channels. These channels feature $(L_e/W, L_m, L_M)$ equal to $(0.45, 3, 4)$, $(0.3, 4, 5)$, and $(0.4, 4, 5)$.

This characterization was performed with HF with a 10 % mass concentration. Subsequent to writing, the channels were examined with an optical microscope, and the side facet was polished. By controlling the length of acid penetrating each of the channels, the average etch rate was computed for each meshing scheme.

FLAE is responsible for the existence of regions between laser scans where acid takes longer to penetrate, and this differential behaviour is directly linked to the selectivity of the chemical species used as etchant. Under these considerations and this type of experiment, two different characteristic rates for the process may be defined,

$$\dot{\ell}_\perp = \frac{\text{etched length perpendicular to the laser scans}}{\text{measurement time}} \tag{3.8}$$

$$\dot{\ell}_\parallel = \frac{\text{etched length along the direction of laser scans}}{\text{measurement time}}, \tag{3.9}$$

where the parallel etch rate will be significantly larger than the perpendicular one. In what follows, we will refer to etch rate when meaning $\dot{\ell}_\parallel$.

It is possible to perform a correspondence between the distances at which neighbouring laser scans are, and the resulting etch rate. These results are shown in Figure 3.7. Firstly, the contour plot exhibits the expected symmetry about the line of equidistance between

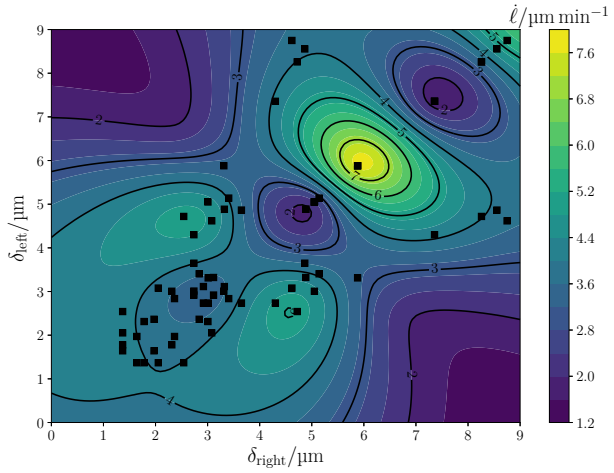

Figure 3.7: Filled contour plot of the dependence of the etch rate of laser scans on the distance to the left and right neighbour scans.

neighbouring scans. Secondly, it can be verified that the etch rate does not necessarily increase by the presence of relatively close neighbour scans, as would be expected in the case of a uniform hatching scheme. This fact points towards the dynamics of the etching process in an attempt to explain why these discrepancies are observed between different meshing schemes.

In other words, the presence of laser scans that are further apart but near the middle of the channel may result in a greater estimated etch rate than near-wall tightly spaced scans simply due to the availability of a larger neighbourhood of modified silica, in comparison to interfacial regions.

Another possible analysis is that of material damage caused by the crossing of a threshold in laser fluence Γ. As described in the introductory chapter, Γ is responsible for the nature of modifications is fused silica. In what follows, using the information from the laser beam profile, it is possible to write the intensity reaching the substrate as

$$I(x,y,t) = I_0 c \left[\frac{1}{1 + \left(\frac{t}{\tau/2\sqrt{\sqrt{2}-1}} \right)} \right]^2 \exp(-2\frac{x^2+y^2}{w_\perp^2}), \tag{3.10}$$

where c is a normalization constant, $w_\perp$ is the $1/e^2$ beam radius, and τ is the full width at half maximum temporal duration of the femtosecond pulses. According to the laser parameters given by the supplier, the laser system features $\tau = 250\,\text{fs}$, and a $1/e^2$ beam width of 2.02 mm; however, due to the optical focusing components in the writing setup, the spot which is focused inside the substrate is much smaller than this latter value. By visually inspecting fabricated devices, $w_\perp$ was estimated to be about 0.65 µm.

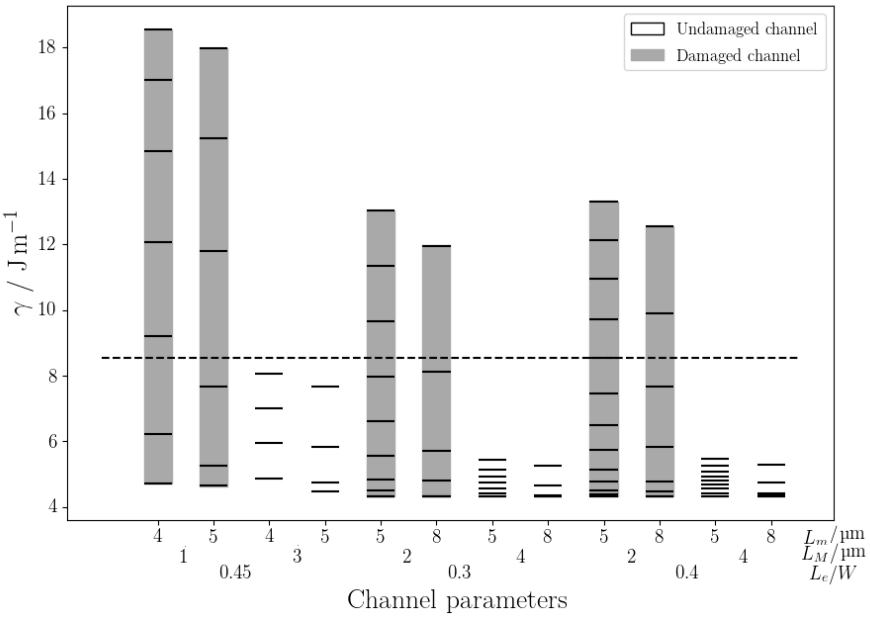

Figure 3.8: Determination of the threshold fluence per unit length (represented by the dashed black line) for the triggering of optical damage due to internal stress in channels with graded mesh etched with HF.

If the focusing were ideal, the laser power would be concentrated in an infinitesimal volume. Instead, it is verified that the profile of one laser shot, in z, is not uniform. By examination of the cross sections of laser scans in fused silica, it is possible to modify Equation 3.10, adding another gaussian factor in z with a different characteristic standard deviation, $w_{\parallel} \approx 2w_{\perp}$. The total intensity within one laser pulse can be estimated by distributing the energy reaching the substrate over an ellipse with axis lengths of $w_{\parallel}$ and $w_{\perp}$.

Armed with these considerations, one may determine the laser fluence within each of the regions inside the photo-exposed area. For that, one laser scan is considered to be a cylinder with cross section of radius $w_{\perp}$, and three intensity profiles are integrated in that cross-section (the one due to the laser scan itself and two from the first neighbours). Finally, since the laser fluence requires an integration time in its definition, a fluence per unit length, γ, was computed, integrating over the time the laser takes to travel one micron. During that time, equal to the reciprocal of the stage movement speed, the laser output consists of f_r/v_{w} pulses, with a cumulative energy of $\epsilon f_r/v_{\mathrm{w}}$.

Following the described procedure, a threshold for optical damage γ_{th} was found to be $8.5\,\mathrm{J\,m^{-1}}$. Each channel was associated to multiple laser fluencies corresponding to each of its comprising laser scans. The optical threshold is defined as the smallest laser fluence per unit length that does not cause damage, and is represented alongside the various determined γ for each micro-channel, in Figure 3.8. Since etching with HF is performed

at room temperature, probably the damage verified upon etching was entirely due to that process.

3.5 Study of the uniform meshing scheme

3.5.1 Etching from the side optimization

The work presented in [47] concerns a multi-parametric writing optimization using HF as etchant. In what follows, a similar approach was followed in order to characterize etching with KOH. For that, 96 channels with a length of 1 cm were fabricated, each with one specific set of optimization variables selected from Table 3.1. The effect of four parameters in the fabrication was tested, namely writing parameters (writing energy per pulse and velocity), and slicing parameters (separation between laser scans and depth, z_w, which corresponds to the distance between the centre of the channel cross section and the substrate surface). The number of scans in both directions was kept unchanged and equal to five; this was chosen in order to have the same number of inter-scans interactions, resulting in a channel width and height equal to 5δ. These 96 channels constitute what is designated hereinafter as first set.

These channels, having been written in depth, were etched with the etchant entering through the side of the substrate. In order to visualize the transverse section as the etching occurs, the substrate side facet was polished using the procedure described in Section 2.1.4. For determining the etch rates, the substrate surface was focused in the microscope, following the alignment of the image with the edge, and focusing on the mid-plane for subsequent photographing. The measurement was aided by the software Image J, and is based in pixel counting upon length calibration. Whenever possible, the etch rates along each of the laser scans was measured, and the etch rate of the micro-channel was taken as the average, with uncertainty equal to one standard deviation.

The results obtained are represented in Figures 3.11a and 3.11b. It is noted that the key analysis feature employed was the presence or absence of fractures in the micro-channel, whether having occurred during the writing or etching stage. As noted before, these fractures tend to develop near the corner regions, probably due to accumulated stress during the writing stage.

Figure 3.9a represents the transverse profile of a number of channels from the first set, written with the same parameters apart from v_w and z_w (namely, $\delta = 4\,\mu m$, and $\epsilon = 60\,nJ$ per pulse. The time evolution of the profile is a valid indicator of etching efficiency depending on the two variables; therefore, it can be concluded that neither of these parameters, in the tested range, was particularly influential in the etch rate or in damage in the material. This is further evidenced in the respective etch rates' variations,

Parameter	First set		Second set		Unit
	Pr.	Test values	Pr.	Test values	
z_w	1	$\{100, 50\}$	1	$\{100, 50\}$	µm
δ	2	$\{1, 2, 3, 4, 6, 15\}$	3	$\{1, 2, 3, 4\}$	µm
ϵ	3	$\{60, 80, 100, 120\}$	2	$\{30, 37.5, 45, 52.5\}$	nJ per pulse
v_w	4	$\{500, 800\}$	–	$\{500\}$	µm s^{-1}

Table 3.1: Fabrication parameters for etching optimization with KOH. Parameters are varied with for loops, and Pr. means the priority order in which, inside these loops, the parameter is varied (for instance, considering the first set, channels 1 and 2 differ only in v_w, and channels 1 and 49 differ only in z_w).

depicted in Figure 3.9b, which are much more influenced by the variation in the scans, particularly in the transition between writing at 60 and 80 nJ per pulse.

The dependence on the writing velocity is directly connected to the possibility of writing mass-producible devices with the FLAE technique, whereas the dependence on the writing depth is a consequence of optical aberrations causing elongation of the beam profile in the z direction, and may hinder high aspect ratio microstructure fabrication. As such, the weak dependence is a good indicator of the possibilities of using the FLAE technique in microchannel fabrication expeditiously.

The energy threshold, ϵ_{th}, for optical damage is most heavily correlated with δ, resulting in smaller ϵ_{th} for smaller δ. Fabrications with very small spacing between laser scans are inviable due to either the crossing of the threshold for fractures or a too small etch rate. Nonetheless, fracture free channels were obtained with the smallest mesh spacing tested by lowering the energy per pulse. This resulted in a second set of tests, with smaller values of the energy per pulse, comprising 32 channels. This second set of parameter variations is also detailed in Table 3.1. It was opted not to vary the writing velocity in the second set.

The number of scans in the second set was not kept constant. Instead, the channel width and height was kept equal to the minimum common multiple of the tested δ, $W = H = 12\,\mu m$. The polishing procedure was the same as described for the first set.

Figure 3.10 represents the temporal evolution some of the second set microchannels sections for several writing parameters, while keeping $z_w = 100\,\mu m$.

It is possible to observe the occurrence of cracks in the section for $\delta = 1\,\mu m$, right after the writing, which are aggravated by the presence of the etchant in the subsequent frames. The smallest energy tested did not cause any fracture even for this smallest

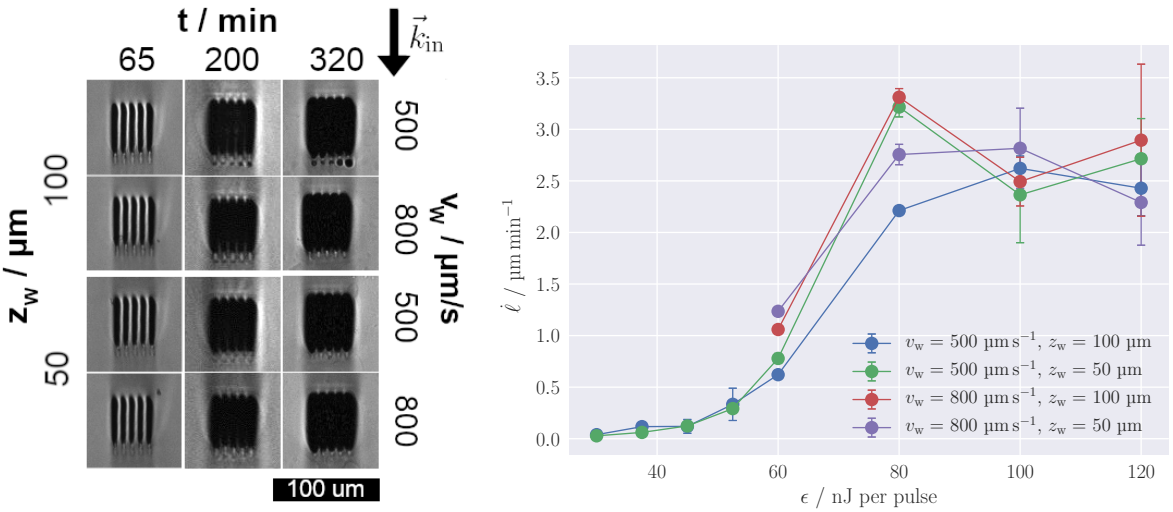

(A) (B)

Figure 3.9: (A) Influence of depth and writing velocity in the etching evolution of a $\epsilon = 60$ nJ per pulse, $\delta = 4$ μm MF channel. $\mathbf{k}_{in}$ defines the direction of the laser beam. (B) Etch rates as a function of ϵ for different values of the writing velocity and depth (channels from first and second sets).

separation; nevertheless, the associated etch rate is too small for expedited fabrication. This constitutes a hindrance in the attempt to reduce the spacing between scans near regions of larger intended resolution and detail. Fortunately, it is also verified that simply increasing δ to 2 μm is sufficient to circumvent this limitation, which may be interpreted as a configuration of larger optical stress released due to the presence of smaller laser fluences.

Interestingly, there are also cases where no crack is visible after the writing, but still it is possible to observe its presence after the beginning of the etching, as evidenced by the images of channel $(\epsilon, \delta) = (45, 2)$. This phenomenon occurs near corner regions and was observed also in subsequent fabrications (the reader is referred to Section 4.5 for a more detailed discussion).

When analysing specifically the section after writing, the most evident feature is the asymmetry between the two principal directions (alongside the height and width of the channel). Since the beam is focused by an objective lens placed with its axis orthogonal to the substrate, the focal volume is more elongated alongside z than alongside in-plane directions x and y. This results in the superposition of laser scans centred at points with the same z coordinate, which creates the anisotropy in the acid penetration due to increased refractive index modifications that results in the vertical lines visible in the left and middle images. These lines are not perfectly vertical, which suggests that the wave-vector of the laser light, $\mathbf{k}_{in}$ is not along $\mathbf{e_z}$, as a consequence of a possible tilt in the substrate when writing (due to the presence of dust, for instance).

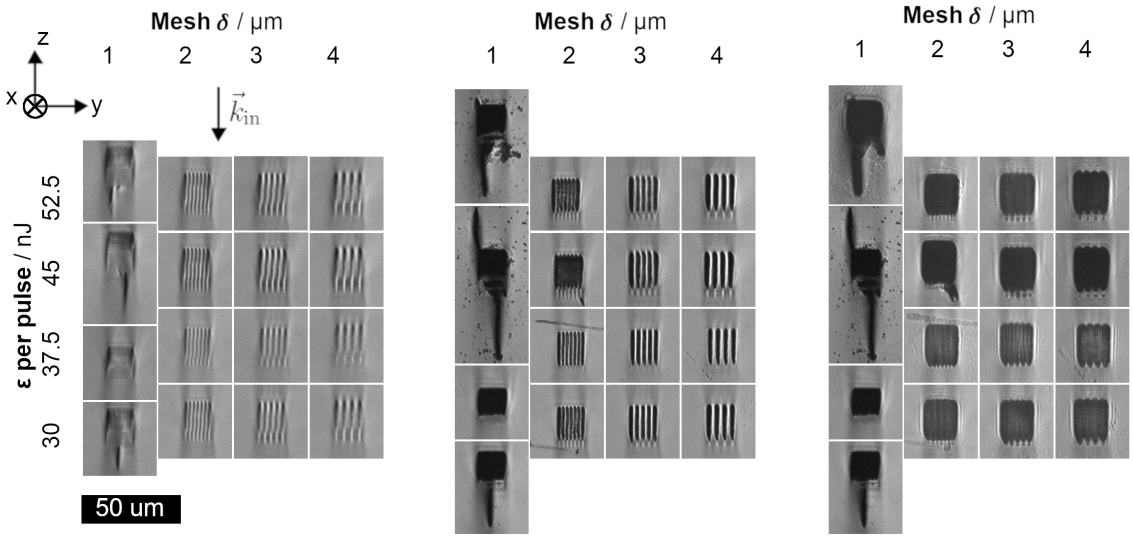

Figure 3.10: Transverse sections of channels etched from the top with KOH, taken immediately after writing (left), after 80 minutes of etching (centre) and 450 minutes of etching (right) as a function of writing energy and mesh spacing. $\mathbf{k}_{\text{in}}$ defines the direction of the laser beam.

The principal consequence of this asymmetry is the existence of a periodic roughness in the top and bottom of the microchannels, as opposed to the side walls. There is even a difference between the top and bottom walls, and the reader may verify that it is the bottom wall where the roughness is more evident: this is a result of the occurrence of optical aberrations that cause the beam profile to appear droplet-like, thinning towards the bottom.

Another aspect concerns the residence time of the etchant inside the channels. Two simultaneous phenomena occur after the initial etchant penetration: the continuation of the etching process along the direction of the channel, and the evolution of etching the entrance region. The etch rate starts to stabilize, accompanied by a change in the tonality of the etched region (cases of microchannels $(\delta, \epsilon) \in \{2, 3, 4\}\mu\text{m} \times \{30, 37.5\}\text{nJ}$ per pulse). This indicates that the etching saturates first if a lower ϵ is used, resulting in a smaller etch rate verified in Figure 3.11.

Finally, following the approach detailed for graded meshes, the optical fluence threshold γ_{th} was determined, by computing the fluence arriving at the substrate (disregarding border effects) for each of the micro-channels in the first and second sets. Since it is admitted that z_{w} does not contribute to the fluence, we plot the dependence on the remaining parameters in Figure 3.12, recalling that the second set (with lower ϵ) was not tested for v_{w} variations, hence the lack of data in the upper horizontal plane.

In the Figure, spheres identify micro-channels where the threshold for optical damage

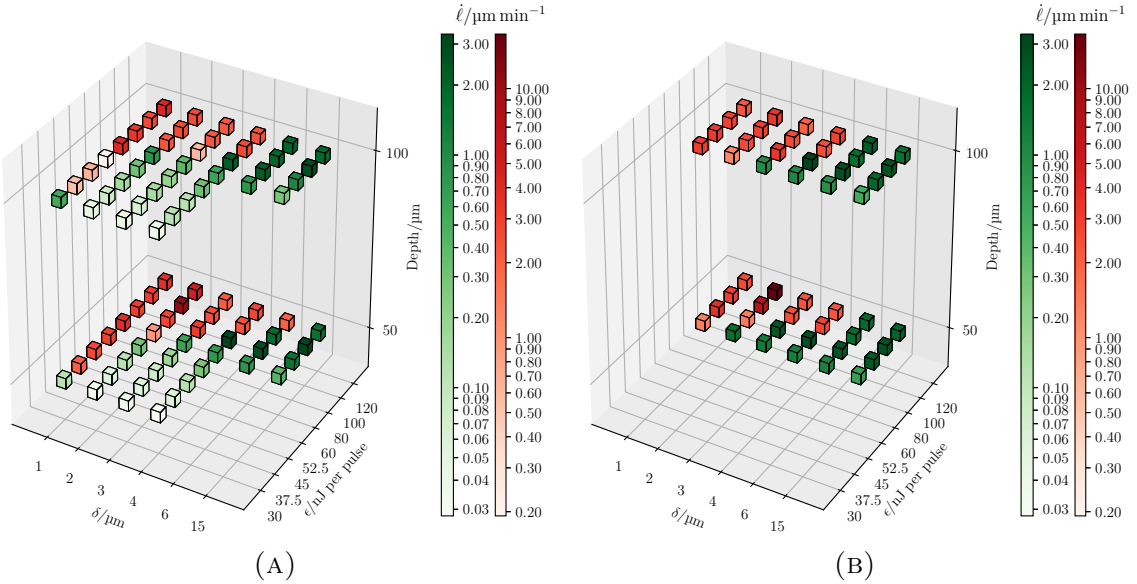

FIGURE 3.11: Dependence of etch rates on the writing energy, depth, and scan separation, for channels produced with KOH-based FLAE, with (A) $v_w = 500\,\mu m\,s^{-1}$, and (B) $v_w = 800\,\mu m\,s^{-1}$. Red cubes represent channels where the combination of parameters resulted in visible fractures.

was crossed, whereas cubes represent undamaged samples. As expected, larger fluences occur when the spacing between laser scans is smaller, and for larger ϵ. Figure 3.12 evidences that γ_{th} is not perfectly determined, meaning that in a given region for γ, damaged and undamaged channels coexisted, with no obvious correlation. That region is estimated visually to be between 3 and $8\,J\,m^{-1}$, with the lower limit taken to be the threshold for triggering random cracks in the substrate.

This interval shows agreement with the data presented for the nonuniform meshing scheme, indicating that this analysis is reproducible and self-consistent.

3.5.2 Optimization of etching with access ports

Recalling that another sort of etching is possible, etching with access ports (depicted in Figure 3.5a), another objective of this work was the determination of the possibilities of writing completely embedded channels in the silica substrate.

Using $\epsilon = 100\,nJ$ per pulse, polarization perpendicular to the writing direction, and $\delta_{x,z} = 2\,\mu m$, 10 embedded channels were written, following the method outlined for channels without access ports. The access ports were written afterwards, consisting of two laser scans of size L_{ac} separated of W_{ac}, repeated in z every H_{ac}, as is represented in the SCA preview of Figure 3.13. The access ports were programmed in SCA just like regular micro-channels, by specifying the stage movements (that is why they are below the channel in the preview generated by SCA).

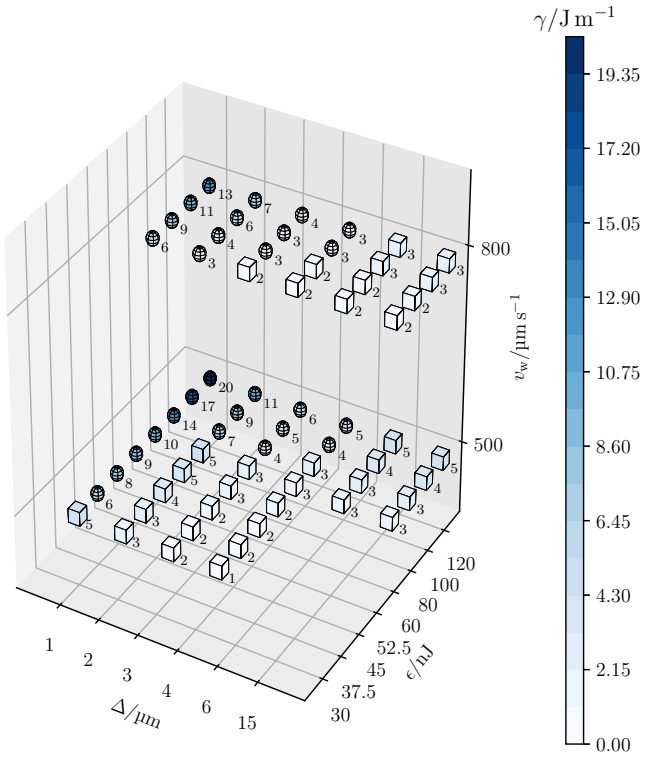

Figure 3.12: Fluences for the various micro-channels etched with KOH, where spheres represent damaged channels, and cubes represent undamaged ones, as a function of fabrication parameters.

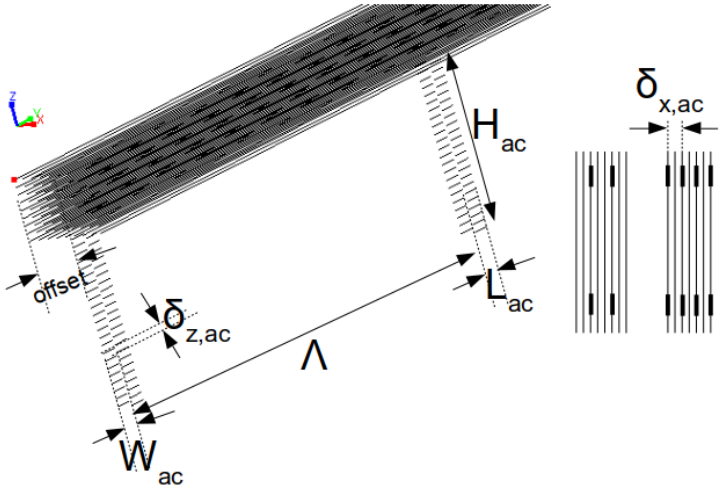

Figure 3.13: Representation of the procedure for fabrication of a buried micro-channel with access ports to the surface, with all relevant geometric parameters. The inset represents a top view of simple access ports (left) and access ports all across the channel (right).

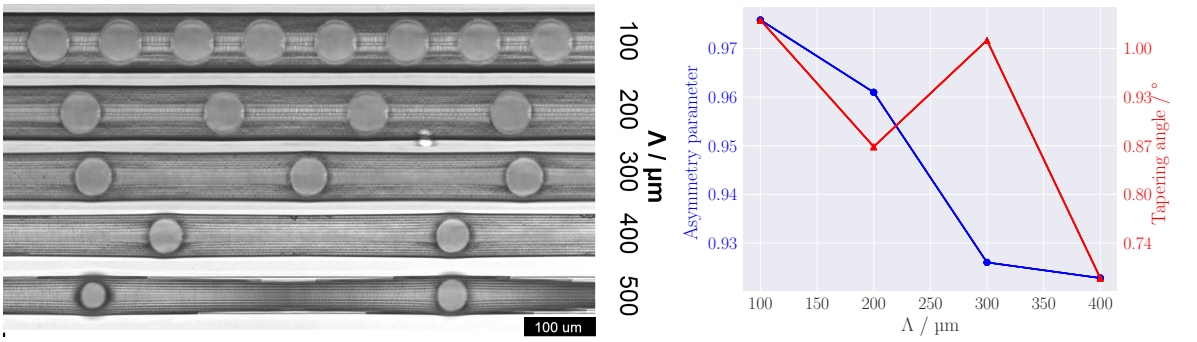

(A) (B)

Figure 3.14: (A) Images composed by joining images of micro-channels etched with access ports, for various values of the separation between ports (distance between channels not to scale), after 360 min in HF. (B) Asymmetry parameter and tapering angle for the etched channels after the same time.

The 10 channels differ only in the variable δ_{ac}, the space between consecutive access ports, which was tested in intervals of 10 µm starting with 100 µm. The geometric parameters of the channels, following notation in Figure 3.13, were: $H_{ac} = 100\,\mu m$, $L_{ac} = W_{ac} = 10\,\mu m$. After writing, the samples were inspected, and subsequently etched with HF. It was observed that an non-negligible tilt in the substrate at the time of writing was responsible for the absence of superficial ablation in some of the micro-channels, whose etching time was thus increased. In order to perform a more accurate comparison, it was decide to repeat the fabrication, and ensure surface ablation.

The sample was then etched with HF and visualized at regular intervals with a microscope. By doing so, we concluded that the etching started simultaneously in every micro-channel, reaching the bottom of the access ports also simultaneously. Further, the asymmetry resulting from the placement of access ports was assessed. Figure 3.14a represents the top view of the channels with the five smallest Λ tested. By analysing the tapering effect due to the diffusion of the acid and differential availability throughout the channel, the channel widths in the midpoint between access ports and in the access ports were measured and are presented in Figure 3.14b, concluding that access ports separated of more than 400 µm represent a non-negligible tapering effect. This constitutes the access limitation for etching with HF.

In contrast, KOH can also be used as an etchant for embedded fabrications. Following the same fabrication protocol, another set of micro-channels was fabricated, ensuring surface ablation for the validity of comparison. Upon a larger etching time, and again verifying my microscopy if the etching was complete, pictures were taken of the etched micro-channels after 10 h.

It was verified that the greater selectivity of KOH results in a hindrance for the fabrication of embedded devices. In fact, whereas with HF etchant diffusion results in penetration

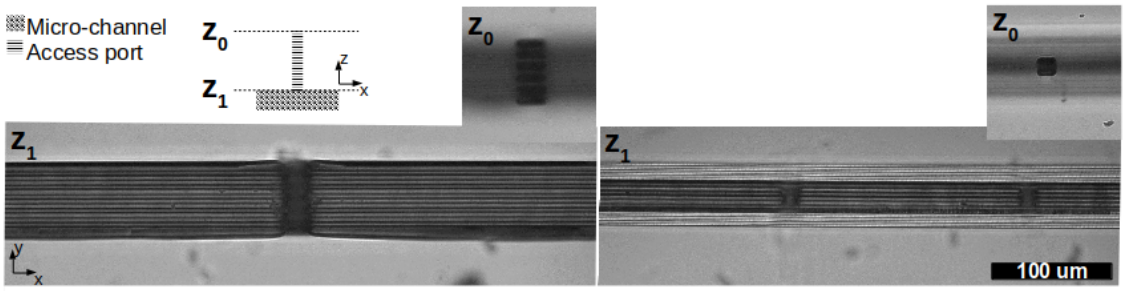

Figure 3.15: Visualization of the access ports and KOH penetration after 453 minutes for ports spanning the full width of the micro-channel with $\Lambda = 500\,\mu\text{m}$ (at the left) and for square ports with $\Lambda = 200\,\mu\text{m}$ (at the right).

in z, followed by saturation due to reaching pristine material, only then following penetration in x, and finally in y (intermediated by the respective etching rates $\dot{\ell}_{\parallel}$ and $\dot{\ell}_{\perp}$), with KOH another etching dynamics occur.

With KOH, the etchant penetrates rapidly along the scanning direction, due to the large selectivity resulting in the contrast between $\dot{\ell}_{\parallel}$ and $\dot{\ell}_{\perp}$, as is evidenced by Figure 3.6, to the left. The access ports, seen at the surface level, are still approximately square, contrarily to what occurs with HF. Merging at the midpoint between ports is the primary phenomenon, only then following penetration along the other coordinates. This results in a much faster etching saturation, visible in the right in Figure 3.15, which can be circumvented by employing larger ϵ or smaller δ, as discussed in Section 3.5; this, however, is directly connected to reaching the critical fluence, thus requires special care when implementing.

Another alternative, depicted in Figure 3.13 (inset, at the right) consists in modifying the very geometry of the access ports, in order to have them span the full width of the micro-channel. This was implemented by fabricating three micro-channels, with the following geometrical parameters: $\delta = 5\,\mu\text{m}$, $L = 5\Lambda$, $\delta_{z,\text{ac}} = \delta_{x,\text{ac}} = 5\,\mu\text{m}$, $W = 50\,\mu\text{m}$, and $\Lambda = 500, 1000$ and $1500\,\mu\text{m}$. The writing energy was set to $100\,\text{nJ}$ per pulse, and the polarization was kept perpendicular to the writing direction.

The results after 453 min, presented on the left in Figure 3.15, of etching with KOH suggest that this approach approximates the etching dynamics of KOH to those of HF. This results both in a greater etching velocity, assuring expeditious fabrication, and in an improvement on the tapering effect which was verified with HF. We further note that the range of tested Λ is larger than the tested range for HF, meaning that the number of access ports required to efficiently etch the same structure is reduced by changing the etchant and the access scheme, again contributing to the reproducibility and fidelity of the fabrication method.

Sample name	$W^0_{\text{top}}/\mu\text{m}$	$W_{\text{top}}/\mu\text{m}$	$W_{\text{bottom}}/\mu\text{m}$	$H_{\text{prof}}/\mu\text{m}$	AR	$\theta/^\circ$
`HF10`	10.79 ± 1.32	20.42 ± 1.00	14.05 ± 1.00	11.22 ± 0.18	0.65 ± 0.04	15.85 ± 3.35
`HF20`	21.65 ± 1.90	33.04 ± 1.00	25.01 ± 1.00	23.24 ± 0.18	0.80 ± 0.03	9.80 ± 1.69
`HF50`	50.87 ± 2.48	65.31 ± 1.00	55.36 ± 1.00	53.59 ± 0.29	0.89 ± 0.02	5.30 ± 0.75
`KOH10`	11.06 ± 0.10	14.29 ± 1.00	14.97 ± 1.00	10.91 ± 0.50	0.75 ± 0.06	-1.78 ± 3.71
`KOH20`	19.88 ± 0.10	22.14 ± 1.82	21.61 ± 1.00	19.72 ± 0.32	0.90 ± 0.04	0.76 ± 2.05
`KOH50`	48.12 ± 0.10	50.93 ± 1.82	50.69 ± 1.00	47.96 ± 0.60	0.94 ± 0.02	0.14 ± 0.84

Table 3.2: Comparison between programmed and effective channel transverse dimensions, after writing (superscript 0) and after etching (no superscript). The name of the sample is a reference to the etchant used and programmed width and height of the microchannel. AR means aspect ratio (height divided by the average width), and θ is the tilt angle of the walls of the micro-channel relatively to the vertical.

3.6 Fabrication of channels for tests

After optimizing fabrication of straight channels, it was possible to proceed with tests, in order to evaluate the preponderance of defects in the fluid dynamics. Three channels were produced with the common parameters $\epsilon = 50\,\text{nJ}$ per pulse, $\delta_{x,z} = 2$, $v_{\text{w}} = 500\,\mu\text{m}\,\text{s}^{-1}$, and $L = 1\,\text{cm}$. Further, the width of those channels were varied, and programmed in SCA to be 10, 20, and 50 µm. After the fabrication, the channels were inspected for defects, which were not found.

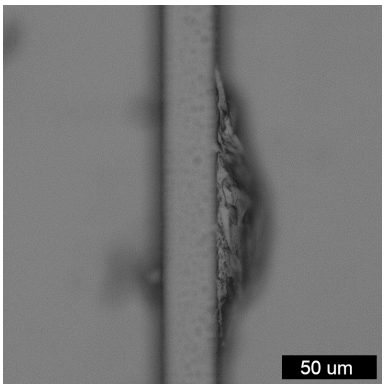

Figure 3.16: Microscope images of a defect occuring in a etched from top microchannel after using a spatula for cleaning of PDMS debris on the surface.

With the aid of microscopic visualizations right after the writing, the widths of the channels, defined as the distance between the leftmost and rightmost edges of the laser scans, were determined and are presented in Table 3.2. Heights were estimated by twenty measurements with a profilometer along the perpendicular at different points in the channels, and taken with an uncertainty equal to one standard deviation.

The hollow micro-channels were bonded to PDMS with the aid of a plasma gun. The alignment of the pierced inlet and outlet with the structure was performed by visual inspection, which was increasingly difficult for smaller micro-channels.

During the experiments with μPIV, some of the samples were debonded from the PDMS. When that occurs, in order to use the same sample, it is necessary to clean the glass substrate from all PDMS residues. For that, it was verified that using a spatula

for peeling, although efficient, caused defects in the etched channels (Figure 3.16), due to the application of shear stress near the limits of the micro-channels. Therefore, it is advised perform cleaning with immersion in acetone over night, followed by isopropyl alcohol cleaning in a clean room environment.

3.6.1 Effect of the interrogation area in μPIV quality

For this study, the sample KOH50 was used. The test fluid chosen was a 2 µm particle aqueous solution with a concentration of 120 parts per million (ppm). After acquiring 100 μPIV images with $t_F = 60\,\mu s$, $\delta t = 1/7.5\,s$, using the 20x objective, while keeping $Q = 180\,\mu l\,h^{-1}$ at the inlet, different post-processing was carried out using the same analysis sequence but varying the width of the IA.

The analysis sequence chosen comprised the following post-processing commands. First, the mask previously defined is applied to the image sequence. Then, an image mean was taken from the ensemble of pictures taken by the software, with the objective of averaging out the contributions of moving particles, and highlighting the positions of stationary particles (stuck to the top PDMS wall of the microchannel). Finally, using this image mean as a subtractive, a difference operation was carried out, thus eliminating the contributions of stationary particles to the final computation of the velocity map.

The resulting set of images was then ready for an average correlation. Considering the geometry of the device, the predicted analytic value for the maximum velocity is $0.042\,m\,s^{-1}$, resulting in theoretical maximum times between frames t_F which is of 17.44 µs for an IA length of 16 pixels, and growing linearly with that length (note that the possibilities for the cross correlation allowed by Dynamic Studio are of 16, 32, 64, 128, and 256 pixels only).

With the experimental data as an array of vectors at equispaced points in the microchannel, and assuming that the flow was fully developed at the tested region, the standard deviation in the velocity component u for points at the same y coordinate was understood as a measurement of the uncertainty associated with the measurement at that given streamline. Dividing this standard deviation by the average of u alongside the streamline, one obtains a metric that can be used to evaluate the quality of the μPIV. By computing the average over all streamlines of this metric, the heatmap in Figure 3.17 was produced. Information contained in that Figure is merely qualitative, but shows how larger IAs provide a more accurate sampling of the velocity field.

Inside each of the squares in the heatmap is the time delay, in microseconds, between the time that should have been used for the satisfying of Equation 2.6 and t_F, where positive values mean that the requirement was indeed satisfied. In fact, the cases where

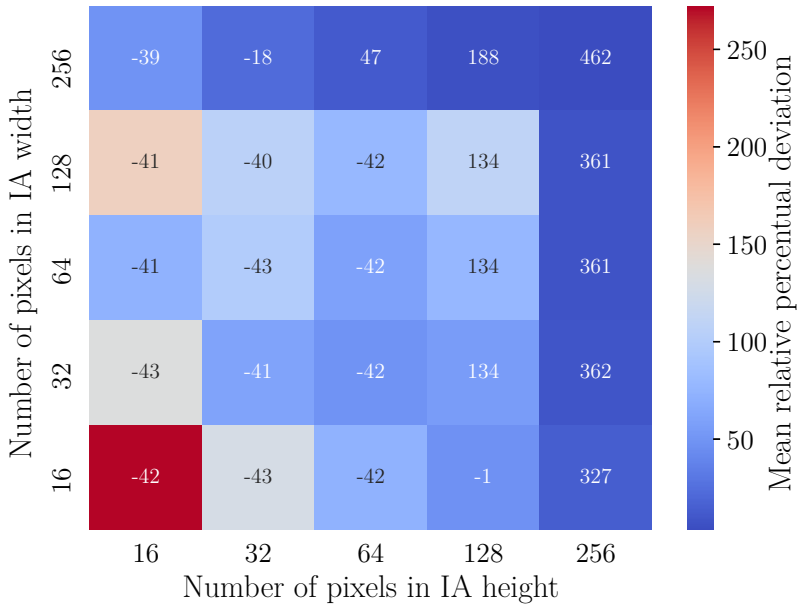

Figure 3.17: Representation of the experimental error in obtaining the velocity profile for a fully developed Newtonian fluid flow using different IA lengths (values in pixels).

the determination of the velocity had larger error were those where the requirement in Equation 2.6 was not satisfied.

3.7 Conclusions

Micro-channels were produced by FLAE, aiming an optimization of writing parameters and meshing scheme for etch rate maximization and optical damage mitigation. A new sort of meshing, characterized by closer laser scans near the edges of the devices, is proposed and evaluated for four 20 µm wide, and eight 50 µm wide micro-channels, with laser scan spacing ranging from 1 µm to 8 µm, and written at 500 µm s^{-1} and 100 nJ per pulse. By comparison with quasi-uniformly meshed channels, the channel cross section was not significantly improved, and the etchant did not enter act uniformly, resulting in a preferential etch which was correlated with the distance to neighbouring laser scans, albeit not in a inversely proportional tendency like uniform meshes. The threshold fluence per unit length was computed using a nearest neighbour model for the laser scan interactions in the focal volume, and found to be 8 J m^{-1}.

Uniformly meshed micro-channels were etched with KOH from the side, and the etching process was monitored by visualizing cross sections. The impact of writing parameters in the quality of the etched channels was characterized; the most impactful parameters in fabrication are ϵ and δ, meaning that buried fabrications are possible at velocities until at

least $800\,\mu m\,s^{-1}$. The safe operation fluence per unit length regime was found to be below $5\,J\,m^{-1}$.

Uniformly meshed 50 µm-wide micro-channels were fabricated integrated in the substrate (with square 10 µm-wide access ports for the etchant), at a depth of $z_w = 100\,\mu m$, with $\epsilon = 100\,nJ$ per pulse, and subject to HF and KOH for the comparison between different access separations. The separations were varied from 100 µm to 1000 µm. With HF as etchant, the maximum access separation without significant tapering effect towards the mid-access region was found to be 300 µm. The dynamics of KOH etching were different, so access ports were remodelled to span the full width of the micro-channels, and separations of up to 1500 µm were successfully tested, resulting in a comparatively smaller tapering effect.

Six channels etched from the top (half with HF, half with KOH) were fabricated with optimum parameters $\delta = 2\,\mu m$, $\epsilon = 52.5\,nJ$ per pulse, and $W \in \{10, 20, 50\}\mu m$, and polarization perpendicular to scanning direction. μPIV tests were possible for the 50 µm-wide channel, and a procedure to take into account noise from particles within the depth of correlation was applied to correct data, having been verified an agreement between experimental and analytical solutions. The effect of roughness modelled by up to second order perturbation theory could not be resolved by the μPIV apparatus available, since the uncertainty is correlation depth exceeds the perturbation contribution.

Chapter 4

Testing the limits of FLAE: the OSCER device

This chapter describes the fabrication of an optimized cross slot device for extensional rheometry purposes. Two laser scanning methods are presented, alongside the Python module created to apply one of them, and compared in terms of the quality of the final device. The uniform meshing scheme is evaluated experimentally, after being etched with KOH and HF, while limitations of this method for embedded fabrication are discussed.

4.1 OSCER device description and fabrication

Cross-slot devices, represented in Figure 4.1, occupy a very important place in MFs, due to the nature of the associated extensional flow. In fact, the central point of the standard cross-slot structure is a stagnation point, where the velocity locally vanishes, and an homogeneous extension rate around that stagnation point. Theoretically, this region should be large in length for a perfect standard cross-slot; however, the limitations in similitude associated to the fabrication methods impose that a small region of constant extension rate is formed, which is still useful in the sense that it allows for applications in extensional rheometry and biomolecule stretching.

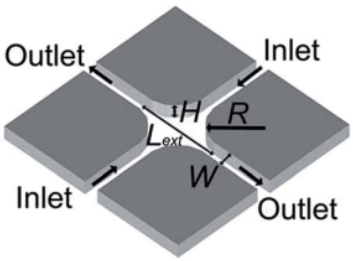

FIGURE 4.1: Sketch of one cross slot device, comprising two inlets and two outlets meeting at 90°. L_{ext} means the extensional length discussed in the text [58].

The most notable hindrance concerns the length of the extensional region, and was the object of a numerical optimization study [7], aiming for an alteration of the shape of the standard cross-slot, iteratively, in order to approximate the associated velocity profile near the stagnation point to a target one. The final

design, baptized as optimized shape cross-slot extensional rheometer (OSCER), was produced by wire-electrical discharge machining in a stainless steel substrate, and successfully tested. Rapidly other tests were conducted with different OSCERs, designed to circumvent the cost of stainless steel machining, while using a vastly disseminated material for MFs (PDMS), which is known to have limitations regarding the aspect ratio of the final devices [58], when it is much larger than unity.

The possibility of three-dimensional micro-machining is one very unique feature of the FLAE technique. Although this was successfully tested with the previous system, the fabrication of more complex designs was, at the time, challenging due to the lack of an adequate user interface for the definition of the pattern to be exposed. In fact, the slicing of the structures was highly mistake prone and exhaustive in those more complex cases. Fortunately, the new femtosecond writing system allows to import of several computer aided designs formats.

As a first attempt to test those features, the OSCER geometry was chosen, due to the degree of complexity involved in the fabrication. Even though PDMS-based fabrication was used for the fabrication of the original devices as explained in [58], the downscaling is a limitation of that sort of fabrication, as well as the fabrication with moderately high aspect ratios.

Using data provided by the authors of [58], it was possible to extract, using QCAD, a list of coordinates describing one quadrant of the device (from which all others could be computed). From that list, the method of slicing for the device had to be chosen. The simplest approach involves importing the respective drawing exchange files (DXFs) drawing to SCA directly, and choosing to fill it with parallel scans oriented along a defined direction.

Another possibility, however, was suggested by the observation of structures produced with the FLAE technique with HF. The smoothness increment due to following the desired contour motivated the development of a Python code for a new manner of object slicing for fabrication. This type of slicing, hereinafter designated as inwards slicing, therefore accompanies the contour of the device, and is obtained by offsetting inwardly such contour, that is, mapping each point of the original curve a fixed distance along the normal direction.

4.2 Algorithm for the OSCER device fabrication with FLAE

The Python module, designated `inwards_slicing`, started with a core definition, to which were added further refinements to deal with some issues of the method. The basic concept

of the algorithm, mathematically speaking, is the mapping of the point at $\mathbf{r}$ to another location, $\mathbf{r}'$, related, in the 2D case, by

$$\mathbf{r} \mapsto \mathbf{r}' = \mathbf{r} + \delta_r \mathbf{e_n}(\mathbf{r}), \text{where } \mathbf{e_n} = (1 + f'(x))^{-1/2}(-f'(x)\mathbf{e_x} + \mathbf{e_y}) \tag{4.1}$$

This continuous case definitions can be extended to a discretized curve via finite differences, in which case the new coordinates can be found by offsetting the midpoint between two points in the original curve, and approximating the derivative accordingly:

$$\mathbf{r'_N} = \frac{1}{2}(\mathbf{r_N} + \mathbf{r_{N+1}}) + (1 + m_N^2)^{-1/2}\delta_r(\sigma_N m_N \mathbf{e_x} + \mathbf{e_y}), \tag{4.2}$$

where m_N is, as usual in first order finite differences, the approximation for the slope of the curve, $m_N = (y_{N+1} - y_N)/(x_{N+1} - x_N)$, and the factor σ_N is a correction to the direction of the normal so as to point correctly, and equals the sign of $x_{N+1} - x_N$. Equation 4.2 was used in the `get_unprocessed_offseted_curve` function; however, in order to obtain good results, the initial raw curve had to be preprocessed after being imported, the reason being that the points in the raw curve are part of a reticulate with a resolution such that it is common to find, amongst consecutive points, those which share at least one coordinate – thus causing problems in evaluating derivatives and offsetting the curve in angulate joints.

After importing the raw curve, a second, preprocessed, version is obtained by computing a moving average of a length which was optimized and found to be five for most sufficiently 'well-behaved' curves. Then, the algorithm described above could be used for the computation of an unprocessed offsetted curve, given the offset δ_r. However, an artefact can occur if the offset is 'sufficiently' large, and which results in the offsetted curve not accompanying perfectly the original one. In Figure 4.2, it is possible to check what happens if a continuous parabola is simply offsetted, for different values of the offset. The occurrence of loops is a consequence of the offset being larger than the distance between the original point and the intersection of the normals at the original point and at the special, derivative sign-inversion point of the parabola ($x = 0$, naturally). Extending this concept to the problem of offsetting an arbitrary curve, it was necessary to eliminate these regions. The process used to do so involved, sequentially:

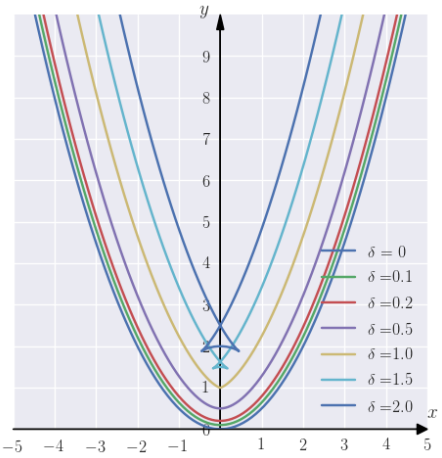

Figure 4.2: Representation, using 4.1, of the mapping of the $y = 0.5x^2$ parabola into other lines, the correspondence being characterized by the associated offsets δ_r.

1. selecting one point of the curve at a time;

2. finding all the points contained within a neighbourhood of radius δ_r of that point;

3. defining segments whose extrema are consecutive points of the curve, if both are within the neighbourhood defined above;

4. finding all intersections (tipically just one) between those segments, while saving the coordinates of the points involved;

5. remove all points between the leftmost and the rightmost point of the list above.

This processing is accomplished with the `smoothen_curve_with_KDTree`, which involves using a binary search tree for an increase in the search efficiency for finding the nearest neighbours of a point with built-in methods[1].

For the check of intersections between segments, an implementation [88] of the Bentley-Ottmann sweep-line algorithm, which was freely available and benchmarked, was used after some tests. It should be noted that, sometimes, the algorithm failed in the finding of intersections for some edge cases, but the exception was already reported, and so another version of the source code was downloaded and properly used.

Afterwards, another sort of numerical artefact was relatively common in the curve, also also a consequence of the geometrical premise discussed in the previous paragraphs: localized one-off inversions in the orientation towards which the curve was heading. For the removal of these events, the routine recursively `remove_nasty_points` verifies the sign of the x-component of the displacement vector between consecutive points, and flags whenever an inversion is produced, provided this inversion is local – that is, another inversion follows within the next ten points (this was also an optimized value based on the tested curves).

Finally, in order to trim the curve and limit it to the first quadrant, so that all others can follow from symmetry without the risk of superposition, another function was coded, `fix_the_edges`, which creates the clipping of the data and adds an additional point at the beginning and end of the curve so that those extrema are contained either in the x or in the y axis. Following this clipping, the remaining curve can be computed using the symmetry in both those axes, and the final curve is then returned to the user as a $2 \times N$ array for further computations and/or storage.

After testing this algorithm for the inwards slicing, a script was run in order to slice each of the OSCERs inwardly, with a starting offset and an increment both of 1 μm, with a final offset left as an exaggerated value, which is handled with a stopping condition for whenever the new offsetted curve contains no point whatsoever, meaning that the center of

[1]The `KDTree` class was implemented as a member of `Scipy`'s spatial algorithms and data structures, `scipy.spatial`. For more information, consult https://docs.scipy.org/doc/scipy-0.14.0/reference/generated/scipy.spatial.KDTree.html (accessed in June 2019).

the structure has been reached. By running this script, and with the help of the `dxfwrite` Python module, we could produce the necessary DXFs for further importing onto SCA.

The reader may wonder why the stereolithography (STL) format was not the chosen one, since it is far more common for three-dimensional micro-machining. The reasons for that are that SCA would not accept either binary or ASCII STL files generated with Blender, obtained by starting with the imported curve, extruding it along the z-axis, and applying to it the Solidify modifier (while it should be noted that this firstly attempted solution, before the coding of the `slice_inwards` module, produced only 'clean', in the sense that was discussed in the previous paragraphs, curves if the offset was positive, that is, the slicing occurred outwardly, which did not serve our purposes) nor would it be possible to accurately control polarization during the writing of one slice if it were considered to be one single piece fabrication-wise.

The control of polarization is important inasmuch as the orientation of nano-gratings alongside one particular direction is directly related to the velocity at which the etchant substance penetrates in modified material, as previously discussed. Thus, when selecting the polarization direction for writing with inwards slicing, it was of interest to compute the average normal direction to the curve, which was incorporated in the script that called the `slice_inwards` function. It should be noted that this polarization is, extending the average to the whole device, zero (due to symmetry along both axes), so the computation was done for one quadrant and symmetries were thus exploited, requiring a change in polarization whenever the writing of one of the slice's quadrants was written.

In order to reduce the time associated with changes in energy and polarization, the fabrication itself was devised in the following manner: firstly, the first quadrant was written, starting from the outermost slice and progressing to the innermost one; then, the fabrication progressed to the next quadrant, counter-clockwise, with the same slicing order. Finally, if the innermost slice was such that the space inside it was not negligible, a final slicing was added, only in the central region, with the SCA-uniform procedure.

4.3 Implementation of complex trajectories in SCA

The software provided by Altechna® has remarkable characteristics for the fabrication of complex geometries. However, one of the most challenging aspects in implementing slicing schemes other than SCA uniform or SCA-built-in ones, was precisely the importing of several drawing format files, without some de-formatting of previously imported ones.

The first approach used to implement the pseudo-code algorithm for fabrication consisted in using a Python task automation module, `pyautogui`, to write, using SCA's GUI, a sequence of commands for the importing of several DXFs, intercalated with commands

for polarization and attenuator changes. All of these three basic commands were encapsulated in a for loop, with a number of counts controlled by an external array imported into SCA, together with the values of rotation angle and new energy for the direct control of parameters for each slice. This first solution, resulted in a very long fabrication file, which, together with the fact that it contained commands that were not actually necessary for a given fabrication, became too heavy and dysfunctional in terms of memory required from the computer. As a result, memory errors occurred which prevented the fabrication of the device with this method.

After corresponding with Altechna®, a different approach was used, using the undocumented command `tarray` to import string variables from a text file. This would, in principle, solve the problem of importing multiple DXFs; however, it turned out that the importing mechanism was bugged for the specific case of keeping the original position of the imported drawings. The use of a patch did not solve the problem, since a problem of code compilation for the launch of SCA would then occur; hence, this second solution using a text file with the paths to all DXFs was abandoned as well.

The final approach for the fabrication of devices with accurate slicewise tunable polarization and energy consisted in reverse engineering the fabrication files, in order to understand the sequence of commands required to achieve:

- the importing of a fabrication file from inside another, including the case where variables must be passed to the imported one;
- the importing of a DXF from inside a fabrication file;
- the definition of variables;
- the addition of a polarization rotation command, including the angle of rotation;
- the addition of an attenuator setting command.

With the Python coded module `auxsca`, the writing of files from scratch was automated, and since it was verified that, if multiple DXFs were imported each from their own fabrication file, there would be no de-formatting of the full fabrication, the adopted procedure was to write a routine that would, sequentially, create a new directory for the fabrication, place all DXFs within a subdirectory, place all associated .fab files within another subdirectory, write a text file containing fabrication high level programming language for one quadrant, and another similar one for the full fabrication.

The creation of the full device, through the `fabrication_full_device.fab` file, in this case in particular, required the importing of the `fabrication_one_quadrant.fab`, fourfold repeated and intercalated with a `Transform` command. It should be noted that

all four quadrants are equivalent only in their local reference frame, whereas polarization is defined relatively to the global reference frame coinciding with the first quadrant's. For that reason, a polarization rotation angle of θ in either the first or third quadrant – recalling that polarization is orientation-independent – translates into an adjusted angle of $\pi - \alpha$ in the other two quadrants. For this reason, `fabrication_one_quadrant.fab` was imported with auxiliary variables for the conversion $\theta \to \pi - \theta$, whenever necessary.

4.4 Fabrication with SCA hatching and slicing

The control application for the FLDWU offers the possibility of controlling the linear stage motion using an STL file. After settling an issue regarding the preview of STLs generated by SCA, it was finally possible to start importing that file format onto SCA, and proceed with two fabrication commands, named slicing and hatching, in order to fill the device with lines representing the path of the laser. Slicing refers to the procedure of cutting the device into layers, parallel to the xy plane; each of these layers can either be simply outlined, by drawing the contour, or filled with laser scans along a predefined direction (this is called hatching).

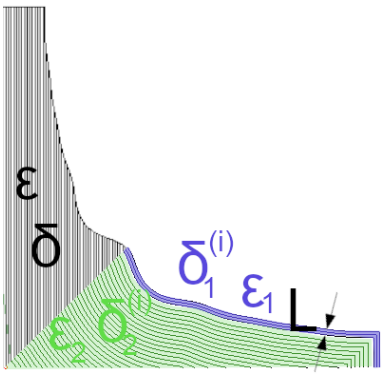

Figure 4.3: Characteristic parameters and preview of a hybrid slicing inwards (lower right) method and of a SCA uniform method (upper left).

In order to test the fidelity obtained by using this meshing scheme, the OSCER was fabricated. The point list corresponding to the contour of the OSCER was imported to Blender, forming the bottom of the device, which was extruded in the z direction and exported as an STL file. Fabrication with this file is relatively simple, and requires only importing, setting the hatching direction, the slicing interval (space between consecutive slices), the hatching interval (space between each laser scan within a slice), and the writing velocity. These fabrication parameters were 2 µm, 2 µm, and 500 µm s^{-1}. The sample thus obtained is named `SCAuni2` and a preview of its laser scans, in comparison with the slicing inwards method, is depicted in Figure 4.3.

4.5 Fabrications with different meshing schemes

Using the `slice_inwards` module, several meshing schemes were tested, using the possibility of changing polarization between quadrants. In order to reduce the time associated with changing polarization, it was chosen to write one quadrant fully, from the outermost slice to the innermost one, and only then change polarization and start the next quadrant.

Sample name	δ_z/µm	$\delta_1^{(i)}$/µm	$\delta_2^{(i)}$/µm	ϵ_1/(nJ per pulse)	ϵ_2/(nJ per pulse)
`uni2_cteps`	2	2	2	52.5	52.5
`uni2_vareps`	2	2	2	52.5	100
`bi23_cteps`	2	2	3	52.5	52.5
`bi23_vareps`	2	2	3	52.5	100

Table 4.1: Samples of the OSCER fabricated for evaluation of the effect of meshing schemes in the post-etching quality.

In Table 4.1, the fabricated devices and respective meshing schemes are listed. The subscripts next to the δ and ϵ parameters refer to the region of the device, as depicted in Figure 4.3. The value of the distance between inter-region separation and outer contour was chosen to be $L = 50\,\mu\text{m}$ for all fabricated devices.

Figure 4.4 shows a composition of four quadrants, each belonging to a different optimized cross-slot, extracted from photographs taken after writing. Considering the writing process described above, and given the necessity to stop the laser after contouring one quadrant, to skip to the next offset, there exist regions with accumulated stress inside the device, by the two axes of symmetry, where two consecutive quadrants meet. It is also pointed out that no cracks are visible at this point.

After the fabrication, the side facet of the substrate was polished in order to reach closer to one of the OSCER arm's transverse section. For that, the polishing had to be especially controlled in order to avoid reaching the OSCER arm, since it was intended to etch from the top.

The visualization of the etching process through the transverse section can be performed in two ways, with the etchant either entering through the polished side (and visualization is direct) or with the etchant entering somewhere else (and the visualization occurs through a small volume of unmodified silica. The first method was applied to the micro-channels, whereas the second method was applied to the OSCER devices. With the etchant entering from the substrate surface, the only possibility for visualization without disturbing the process is by polishing one of the sides of the substrate, while making sure one of the cross-slot's arms is sufficiently close to that side (but without creating a connection between the modified arm region and the outside).

Two approaches could have been followed: either the substrate is polished prior to writing, or after it. When writing microchannels for the etch rate computation, as in Chapter 3, the polishing was done after writing. In this case, it could have and should

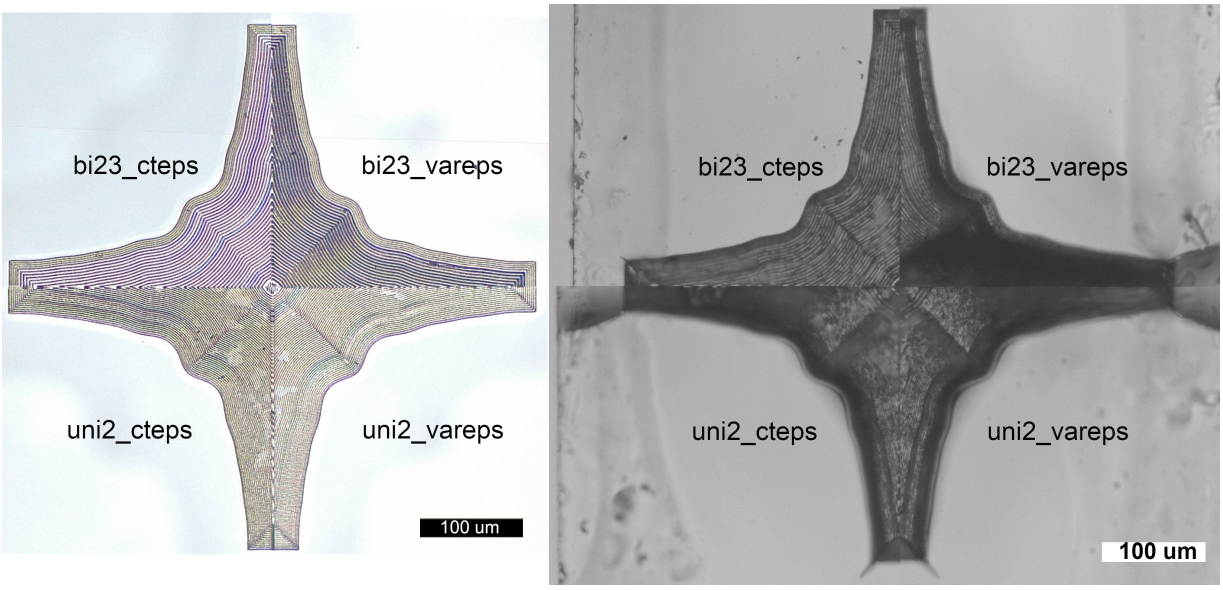

Figure 4.4: Images composed from photographs of quadrants of the four different devices described in Table 4.1, taken ater laser engraving (left) and after 5 h of etching with KOH (right).

have been done prior to writing, because one does not wish to connect the modified area to the air. Instead, the same approach as for microchannels was followed.

Polishing had to be monitored using the setup in Figure 2.6, visualizing periodically the substrate from the top and recording the positions with a cell phone camera. In every polishing plate, it was verified that the removal of material only started after an initial latency due to an initial rectification of the section, which lasted for about 20, 30, and 60 min in the first, second, and third polishing plates, respectively.

The removal rate, or distance variation, $\dot{d}$, after the initial rising period, stabilized in the following values, measured for the presented angular velocities of the polishing plates (in rotations per minute, RPM): $\dot{d}_{\substack{\text{stage 1}\\ 18\text{ RPM}}} = 12.1\,\mu\text{m}\,\text{min}^{-1}$, $\dot{d}_{\substack{\text{stage 2}\\ 15\text{ RPM}}} = 4.6\,\mu\text{m}\,\text{min}^{-1}$, $\dot{d}_{\substack{\text{stage 3}\\ 12\text{ RPM}}} = 0.2\,\mu\text{m}\,\text{min}^{-1}$. An accurate control of the amount of removed material should be primarily directed to the first and second polishing plates, as the third polishing plate's objective is mostly the smoothing of the facet, rather than the removal of material.

By comparison between the transverse profile after finishing at all of the polishing plates, it was verified that the wax excess was removed and the interfacial layer's size was reduced. The removal rates determined above are subject to the condition that the substrate must be sufficiently lowered in the jig – by unscrewing the appropriate lateral screw depicted in Figure 2.6 – in order to be adequately polished; otherwise lower removal rates are to be expected.

After polishing it was verified that samples `uni2_cteps`, `uni2_vareps`, and `bi23_vareps` showed fractures in the corner regions of at least one of the cross slot's arms, as represented

in Figure 4.5. No correlation could be established between the occurrence of these fractures and the outermost writing energy, or the final distance between the device and the substrate's surface, hence they are attributed to the action of compressive forces originating in the successive polishing plates. The only two damaged arms of the cross slot were those perpendicular to the substrate polished side. These polishing induced microfractures may suggest that some of the micro-channel parameter combinations represented in Table 4.1 do not cause optical damage *per se*.

Next, the samples were etched in KOH for a 15.5 h interrupted period. After the first five continuous hours of etching the devices were removed, placed in a goblet with room temperature water, and observed after cleaning in a clean-room environment. The recorded images, shown in Figure 4.4 to the right, show that the etching dynamics, although agreeing with previously observed images of simple channels, is now accompanying the contour of the device, resulting in a smoothing of the interface with pristine material. In Figure 4.5, taken after the full etching period, it is observed that new fractures appear, namely in the two arms which showed no fracture after polishing. This had already been observed in straight channels, and deserves now a more detailed discussion.

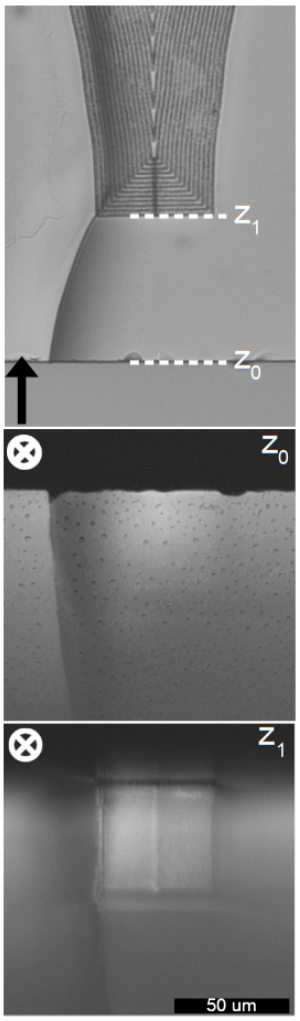

Figure 4.5: Top and side views of microfracture in sample `uni2_cteps` after polishing (arrows indicate the laser beam's wave-vector).

The procedure for KOH etching involves removing the substrate from the etchant at 85 °C and placing it in a glass goblet with room temperature water. At this stage, the interplay between the accumulation of tension (which is greater in corner regions where the laser is forced to accelerate) due to material modifications and the thermal shock. Silica has a remarkably low thermal expansion coefficient of the order of $\approx 10^{-6}\,\mathrm{K}^{-1}$, reflecting into dislocations of the order of the micrometer for a silica substrate. In the context of a Burgers model, these dislocations are propagated along a Burgers circuit reaching regions where optically induced stress is high, are suggested as the cause of the microfractures observed.

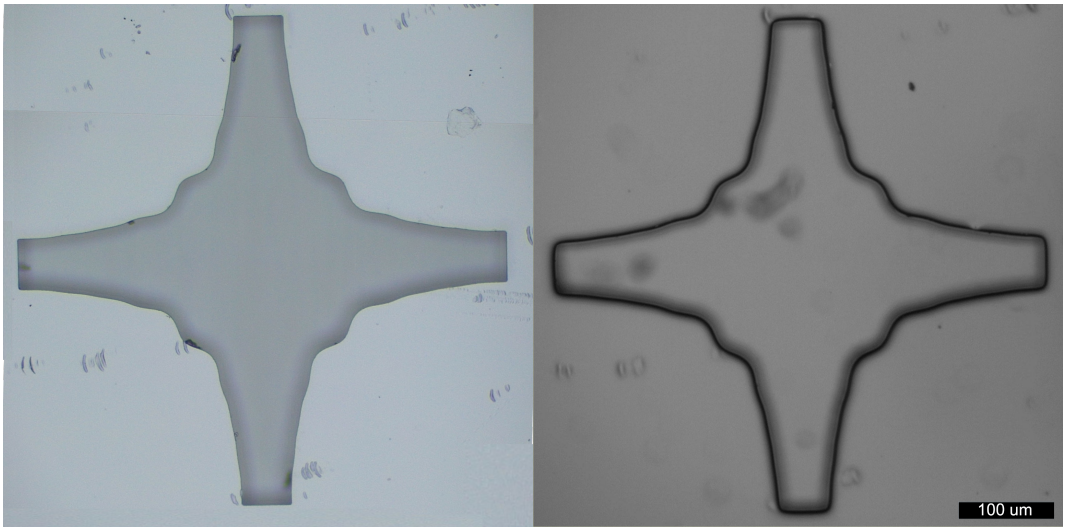

Figure 4.6: Microscope images of the `SCAuni2` after 345 min KOH etching (left) and after subsequent thermal annealing and cleaning with ultrasonics (right). Right image was manipulated to overlap perfectly with another post-annealing image.

4.6 Effect of thermal annealing

Post-thermal annealing is a mandatory stage for the enhancement of selectivity due to the photochemical processes occurring upon femtosecond laser irradiation of Foturan glass [89], resulting in an important contribution for surface roughness reduction. On the other hand, the photophysical nature of the refractive index modifications by femtosecond laser irradiation in fused silica dispenses with post-annealing [70].

Nevertheless, the suggestion of thermal post-annealing was suggested by He *et al.* [90] as a method to improve the micrometric surface roughness in fused silica. Although the exact mechanisms surrounding the smoothing in this amorphous material are not yet understood completely, this method has been used and studied in specialized literature. One simple explanation [91] suggests surface tension overcoming thermally decreasing viscosity forces, accompanied of material redistribution in an energetically favourable configuration of smaller roughness.

The nature of this material redistribution is attributed by the Mullins' model to the preponderant action of either viscous flow, evaporation-condensation, volume diffusion and/or evaporation-condensation or surface diffusion [92]. Finally, the major contribution at an annealing temperature of 1200 °C was empirically related by Osawa *et al.* [93] to the viscous flow, at the micrometric scale of roughness.

With these considerations in mind, and in order to verify the effects of thermal annealing in the device outline, the `SCAuni2` sample was subjected to a thermal treatment for a period of 10 hours, 5 of which with a time varying temperature with slope 15 °C min^{-1}, followed by another 5 hours with the temperature fixed at 1250 °C.

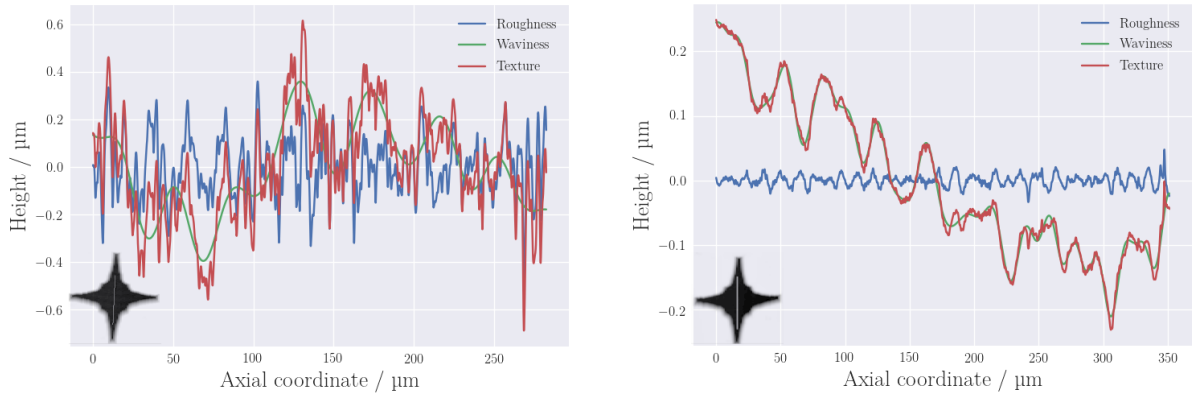

Figure 4.7: Profilometer scans along the paths shown in the lower left corner insets of the `SCAuni2` device (left) after 480 minutes of etching, and (right) after 480 minutes of etching plus thermal annealing.

In Figure 4.6, two top photographs are shown of the sample right before and right after thermal annealing, from which it is inferred that the annealing caused rounding of corners, as well as diffuseness in the microscopic image boundary. The areas of the cross-slots section (seen from top) were computed, resulting in $82\,640 \pm 363\,\mu m^2$ before annealing and $85\,546 \pm 2158\,\mu m^2$ after annealing. The uncertainties arise from the diffusiveness in the contour seen in the microscopic images. From these values, an increase of 3.4 % was observed in the size of the optimized cross-slot, so it is inferred that the thermal annealing causes an increase in the hollowness of the structure.

During the etching process, the device was scanned periodically in order to verify if the desired depth had been reached. After 480 min, etching was definitely interrupted, and the device was 3D mapped by a succession of high resolution profilometer scans. As post-processing, one segment of the map was extracted and Gwyddion was used for a computation of roughness, admitting a model where long period contributions for the texture are separated of the short period contributions by a cut-off frequency. This cut-off frequency was chosen in a way to minimize the skewness of the resulting roughness, admitting that it must be direction independent [94].

The resulting roughness profile and the profilometer tip path are represented in Figure 4.7, which also depicts the same information for the annealed device. By direct comparison, it is verified that, as desired, the thermal treatment enabled a reduction of the root mean square (RMS) roughness from 127 nm to 8 nm, and a reduction of 151 nm to 115 nm in RMS waviness.

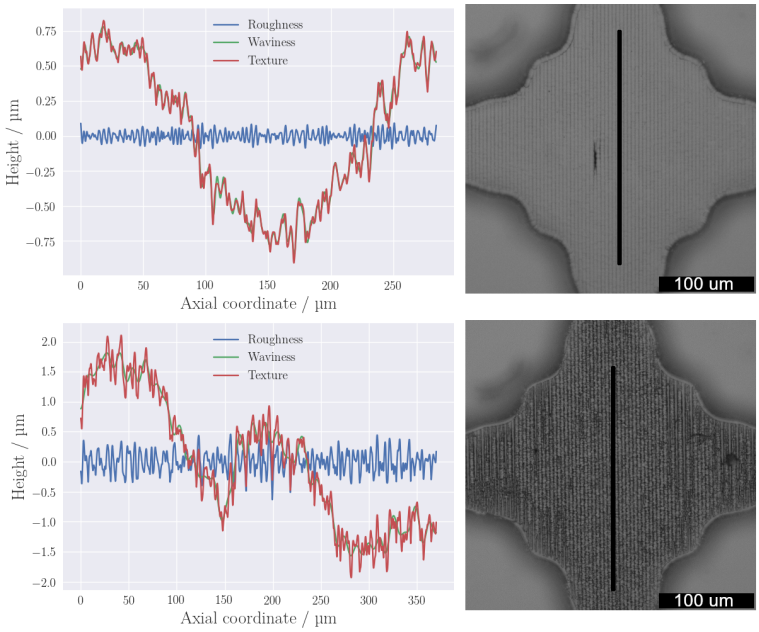

Figure 4.8: Profilometer scanning results for the OSCERs etched from the top with HF (top figures) and KOH (bottom figures). To the right of each plot, a microscope image of the respective device is shown, along with the scanning line.

4.7 OSCER fabrication with and without access ports

Four identical OSCERs were written in the same silica substrate, using also the same laser scan filling. All of these OSCERs were similar to sample `SCAuni2`, only with $\delta = 4\,\mu m$. Two were fabricated embedded in the silica substrate, with access ports, and two were fabricated at the surface.

The OSCERs fabricated with access ports were inspected upon writing, and no defect was found, including fractures. One of those devices was etched with HF for a period of 1 h and the other with KOH for a period of 22 h.

Profilometer scans for KOH and HF etching are represented in Figure 4.8. A first look shows that the expected periodic zero-averaged texture is in fact only present in short wavelengths contributions below the periodicity of laser scans, whereas a modulation by longer period contributions can be explained by a tilt of the scanning direction and the normal direction to the laser scans. A direct comparison between HF and KOH shows that HF is a more effective etchant for the removal of superficial roughness in the bottom of the cross-slot. Still, the existence of RMS waviness of 502 nm (HF) and 1.05 µm (KOH) constitutes a perturbation whose effect has to be verified in the fluid flow. The RMS roughness values provide further confirmation, being of 35 nm for HF and 176 nm for KOH, whereas the RMS period of the perturbations, determined with an FFT analysis, was determined to be larger for KOH (4.84 µm) than for HF (3.27 µm). These spatial wavelength measurements could be expected to reflect laser scan periodicity; however, the

scanning direction parallel to laser scans affects negatively the accuracy and confidence of the measurement.

After scanning the cross slots, they were cleaned again with an ultrasound ethanol bath for 5 min, followed by deionized water and compressed air jet. A piece of PDMS was pierced with the two inlets and two outlets of the device, using a visual estimation of the distance between accesses, and the bonding surface was cleaned with compressed air jet. Both the sample and the PDMS were treated with a plasma gun, for surface activation, for a period of 5 min, and the alignment of the PDMS accesses with the etched OSCER was performed visually. After verifying the alignment with a microscope, the assembly was pressed together using tweezers and stored until the next day, for bonding enforcement.

Figure 4.9 represents the cross-slot devices produced with accesses. Neither KOH nor HF were effective in etching in an homogeneous manner, due to the fact that the vertical direction (along $\mathbf{e_y}$) was preferential for etching. This happens as a consequence of how nanogratings are oriented relatively to the laser polarization and the path of the laser scans, discussed in Section 3.3.

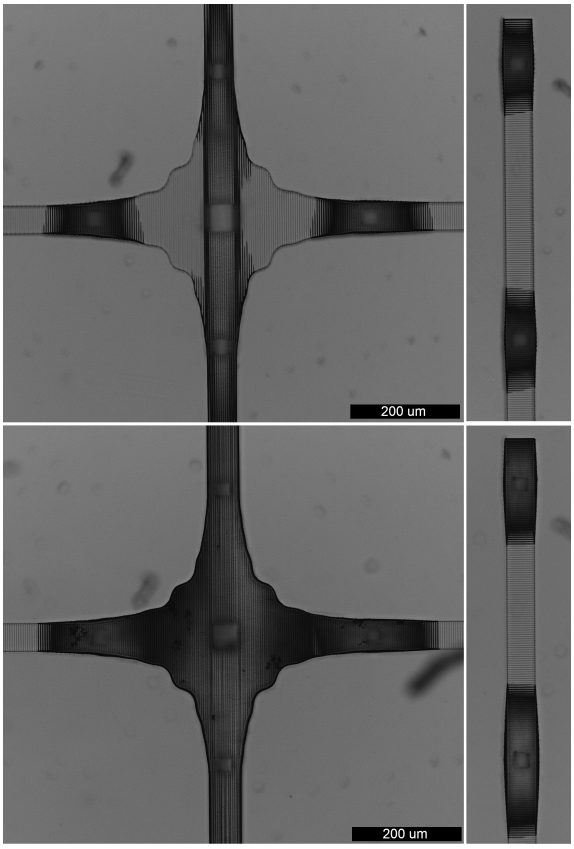

Figure 4.9: Microscope images of two OSCER devices etched from the top with HF after 90 min (top images) and with KOH after 22 h (bottom images).

The devices fabricated with etching from the top were cleaned with a sequence of ethanol, acetone, and isopropyl alcohol, followed by ultrasonics cleaning with deionized water. After 5 min exposure to a high frequency plasma generator, the devices were bonded with PDMS, and the alignment was verified with a microscope, similarly to the protocol followed for simple channels.

The sample etched with HF was not tested with μPIV. This happened due to the debonding of the PDMS from the substrate, which happened for not yet understood reasons. After trying the same protocol described above, but not in a clean room environment, subsequent microscope observations allowed to conclude that the presence of debris next to the regions of the PDMS accesses could become problematic in future experiments. This was indeed verified when connecting the MFD to the syringes and starting the fluid flow, since the fluid was not confined to the path in the

glass substrate, rather it was leaking through the area with the debris, causing another debonding. Further attempts to test this device should include bonding in a clean room environment, or alternatively a higher reactive plasma, with an increased percentage of oxygen, instead of room air plasma.

The sample etched with KOH was tested for different flow rates, in the μPIV apparatus described in Chapter 2. The device was connected to three syringes, two serving as inlets, and the other serving as outlet. The outlet syringe is used because, due to micrometric defects in the cross-slot, and imperfect PDMS piercing, the flow rates through both outlets may not be perfectly balanced; if the outlet syringe imposes a constant, symmetric flow rate to that of each of the inlet syringes, it is guaranteed that both outlets exhibit the same flow rate. The protocol followed for the connection in this multi-inlet device was as follows: first, the outlet without syringe was connected, then the device was filled with tracer fluid, and the two inlets syringes were connected with the respective Tygon pipes, followed by the outlet syringe connected (the respective pipe and a few millimetres of the syringe filled with tracer fluid).

The μPIV tests were performed with a 20x objective lens, with a variable time between frames considering the Re. The post-processing consisted of masking the data to account for the presence of walls, taking one average correlation with variable IA (the areas tested were squares 16 and 32 pixels of width), followed by another average correlation. The second correlation is prescribed in the μPIV software user manual, and uses the option to import the first correlation an offset vector map to improve the results of the second, by mimicking a dynamic search for the particles in a broader area than the usual IA. Finally, a moving average filter is applied in order to smooth the results, before presenting the velocity vector map.

Data was processed with a Python script which performs the following tasks:

- masking the data according to the mask which had already been defined in Dynamic Studio;
- finding the column of data which corresponds to the smallest absolute mean value of the U_x component of the velocity vector (should be the outlets' centre line of the cross slot if the flow rates are balanced between the outlets);
- detecting the centre of the extensional region, in that row of data, which corresponds to the point of U_y component inversion (computed by linear interpolation);
- detecting the extensional region, which corresponds to a linear variation of the U_y component of the velocity vector with the streamwise coordinate, which is accomplished by starting with the inversion point, and adding neighbours to the left and right until the r^2 of the fit to a straight line goes below a given threshold);

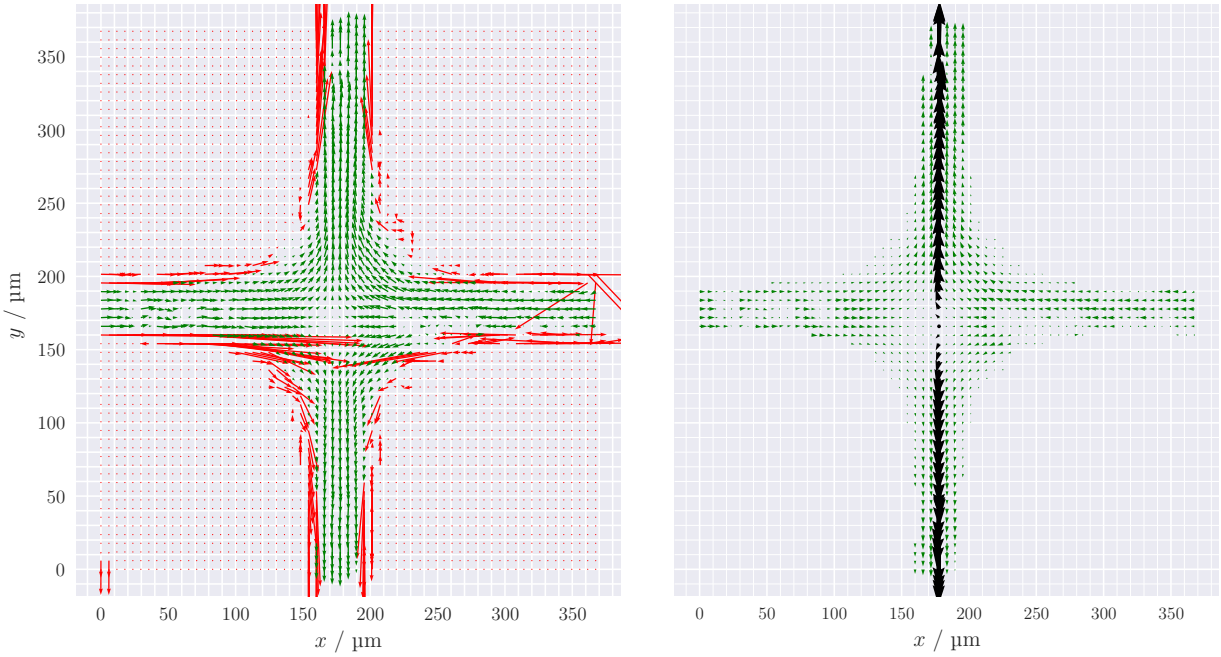

Figure 4.10: Application of the processing algorithm provided by Dynamic Studio for the masking of data near the micro-channel walls (left, vectors in red), and of our algorithm for the determination of the centre stream line in the outlet (right, vectors in black). Vector sizes are normalized to the maximum magnitude in both images.

- performing a fit of the velocity profile in the extensional region to the function

$$u = [1/(ax)^p + 1/b^p]^{-1/p}\,, \tag{4.3}$$

  where a, b, and p are parameters to be optimized on a least squared differences scheme for the experimental data. This is a procedure suggested in [58] in order to mitigate the occurrence of high spatial frequency noise in the computation of strain rate. The initial guesses for those variables are, respectively, the slope near the stagnation point, the maximum of velocity within the extensional region, and 2;

- returning the degree of accuracy of the fit (quantified with the r^2 of the least-squares fitting), and the optimum parameters, one of which (a) corresponds to the experimental strain rate.

Figure 4.10 shows one example of the application of the masking to remove the velocity vectors obtained next to the micro-channel walls, as well as the determination of the centre outlet streamline by the method above described. The frame of reference assumed for the following discussion is that suggested by the axes labels in Figure 4.10.

It was ensured that the time between frames was compatible, in terms of the discussion presented in Chapter 2, with using both tested IA lengths. The fit with the expression

in Equation 4.3 allowed the estimation of two quantities, which are the strain rate in the central region, and the length of the extensional area.

From the estimation of the strain rate, the plot in Figure 4.13 was obtained. For the several tested Re, it was verified that the IA length had decisive influence in the computed strain rate. It is documented that this quantity should increase with increasing flow rate; this is verified if 16 pixels IA length is used, but not for 32 pixels, which precludes the hypothesis of having wrongly chosen the time between frames.

Nevertheless, the observed anomaly in the strain rate is apparently reserved to low Re. Even though the device fabricated in the course of this work corresponds to a global reduction of the PDMS device to one half in all dimensions, the fact that the fluid used is Newtonian means that the variation of the normalized velocity as a function of the normalized position should be exactly the same as long as the Re is small. While studying the same Re with a 50% size reduction, the average velocity in the entrance profile should increase by a factor of 2, meaning that the dimensional strain rate, computed as the slope of the curve relating the velocity along the position, should rise to a factor of four. By correcting data to account for this factor, the strain rate variation with the Re is close to that reported in [58], as represented in Figure 4.13.

The first comparison note between all-PDMS fabrication and FLAE-aided fabrication concerns the shape of the $v(y)$ dependence, which is significantly different from the numerical simulations prediction. This may suggest that either the data processing routine is selecting data wrongfully, the average correlation performed in Dynamic Studio might be affected by noisy frames, or that the effect is purely due to the fabrication method used.

The first hypothesis was discarded by monitoring carefully the data selection and processing, being verified that, even in the cases where the stagnation point is not exactly at the centre of the cross slot (this may occur as a consequence of the geometry of the device itself, and may be mitigated by playing with the suction flow rate in the outlet syringe). The algorithm for processing is thus validated, which can be verified by the fact that all velocity profiles pass through the origin of the frame of reference, certifying the process of identifying the stagnation zone.

The second hypothesis cannot be discarded. Considering that the device in PDMS was twice as large in all dimensions, and having been characterized with the same setup, meaning the same IAs for average correlation were available, it can be inferred that larger areas could be used, resulting in the same number of experimental points for statistical significance. Having been established, in the previous Chapter, that the inclusion of larger IAs, by permitting larger freedom in the time between frames, and in the estimation of the largest velocity in the particle ensemble, results in lesser noise and average correlation

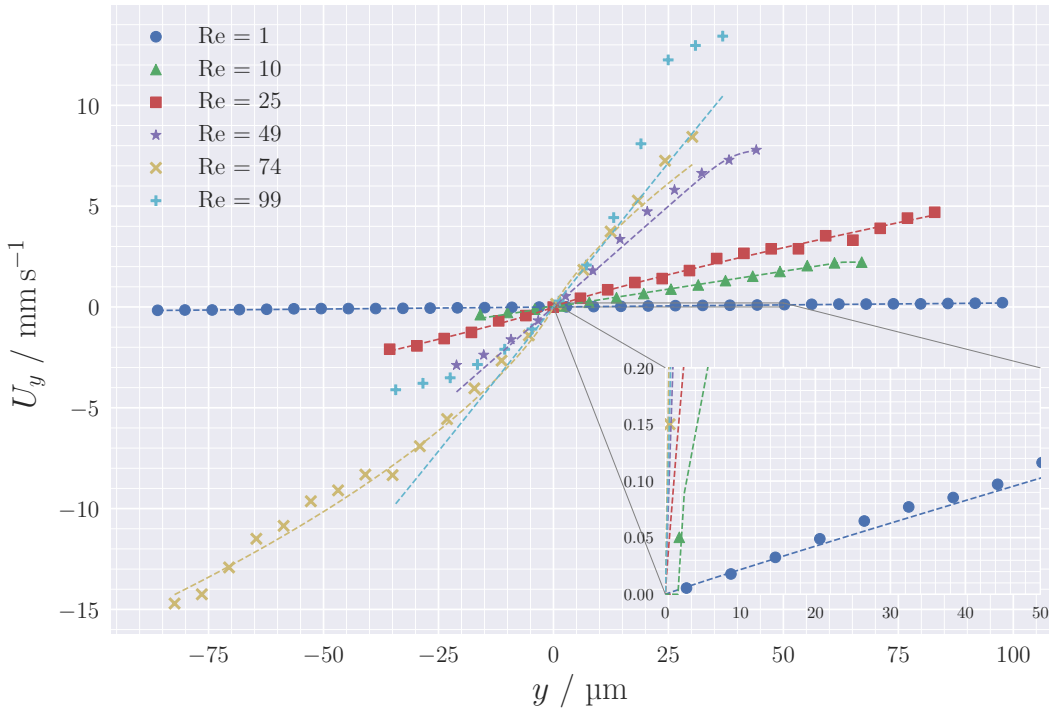

(A)

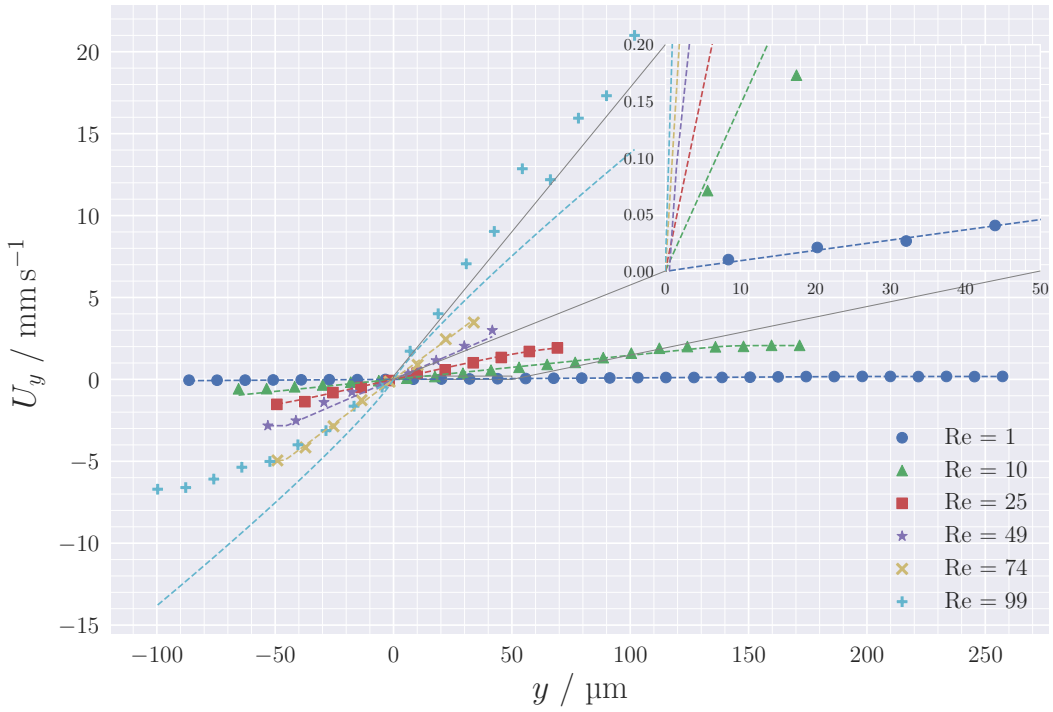

(B)

Figure 4.11: Velocity profiles for the central region of the cross-slot, obtained after data processing (see text), with an average correlation area length of (A) 16 pixels and (B) 32 pixels. Dashed lines represent the fitted function of Equation 4.3.

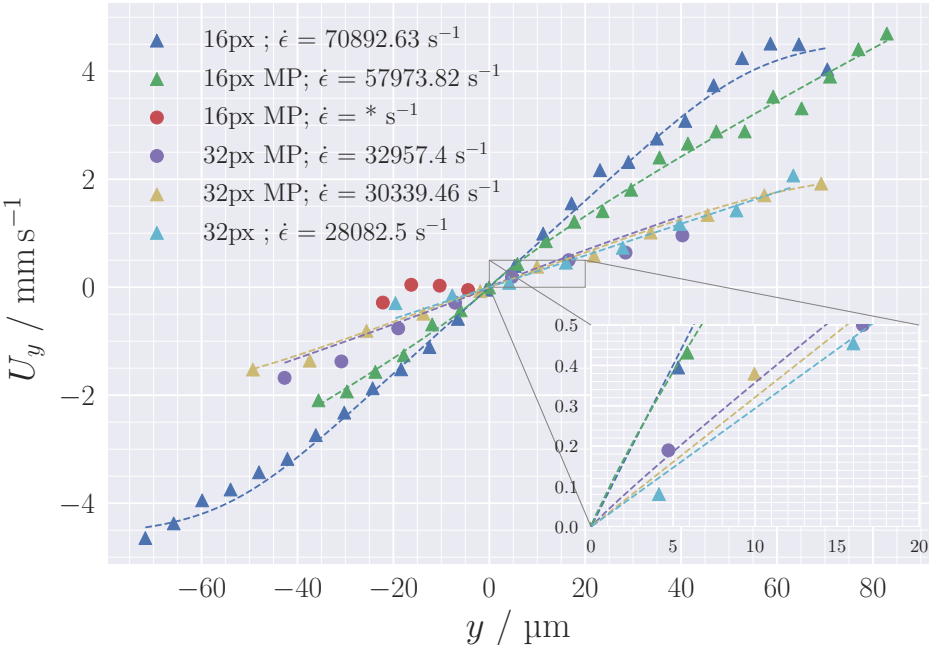

Figure 4.12: Influence of a slight defocus off the middle plane of the cross-slot, and of masking data frames containing bubbles and foam, on computed strain rate (triangles represent masked frames, MP means middle plane measurement, * represents a failure in the computation algorithm).

standard deviation, it is proposed that our characterization may have been affected by the dimension reduction.

On another note, in order to assess the influence of measurement errors in the μPIV experiments, it is presented, in Figure 4.12, data obtained with the processing algorithm of the flow profile in the centre outlet line at the same Re, equal to 25. There, the influence of two experimental variables is represented: data with the label MP was acquired with the focusing plane estimated to be the mid-plane of the device, whereas data without that label was extracted at a deviation of only 7.5 µm from that mid-plane. It can be seen that an error was introduced in the computed strain rate for the 32 pixel case (the 16 pixel case could not be handled by the routine developed). The largest contribution, nonetheless, to uncertainty, was the presence of defective image frames in the dataset. The number of defective frames, which were removed after visual inspection of the ensemble, was of 34 for the 16 pixel case, but of only one image which contained a few bubbles in the 32 pixel case. The fact that only one frame could cause such a difference in the evaluation of the strain rate, along with the fact that 100 images were taken per trial, points to the possibility that some of the experimental correlations were affected by defective frames.

Finally, it is possible that the lack of correspondence between the PDMS and FLAE cross-slots could be due to the fabrication method. For that to be verified, the OSCER

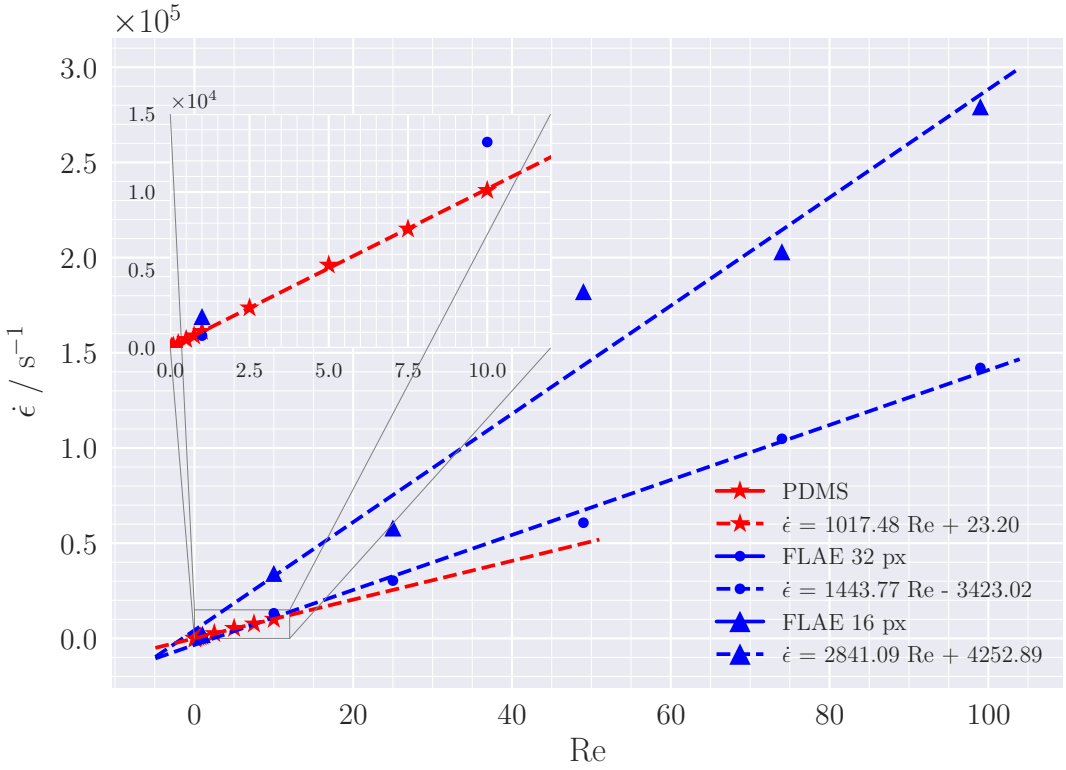

Figure 4.13: Comparison between PDMS based cross slot (data provided by the authors of [58], and FLAE based cross-slot.

fabricated with HF requires testing and verification if the reduction of the perturbation in the bottom of the device results in an approximation towards the numerical profile. It should be noted that the device was placed in such a way that the fully developed flow in the two inlets exhibits streamlines which are parallel to the laser scans paths from the fabrication step.

In Figure 4.13, strain rate data from the fabricated device was computed and compared to the same device fabricated in PDMS. It can be seen that the results from both OSCERs show a 67% agreement (relatively to their mean value), if considering the IA with a side of 32 pixels. In order to obtain better resolution and accurate results, two post-processing sequences could have been performed, one with an elongated IA in the x direction, and the other in the y direction, selecting data from both sequences accordingly (for the inlet and outlet regions, respectively, where the fully developed flow is known to be independent of the local streamwise coordinate).

4.8 Conclusions

A Python `slice_inwards` module was devised to produce the inwards slicing (accompanying the contour) of a complex extensional rheometer. This module was extensively

debugged in order to deal with requirements in the fabrication procedure. Another module was created for the interface between the `slice_inwards` module and the fabrication software SCA, due to inadequacy of the software in changing polarization in mid-fabrication.

The created module was tested in four different OSCER devices, selectively changing polarization to keep it perpendicular to the average dislocation vector along each quadrant. The energy used in the outermost and innermost layers of the device was varied (outermost 52.2 nJ per pulse plus innermost 100 nJ per pulse versus uniform 52.5 nJ per pulse all over), as well as spacing (closer scans with $\delta_r = 2\,\mu m$ adjacent to walls and $\delta_r = 3\,\mu m$ in the inner volume). By writing near the substrate edge and polishing, the visualization of the cross section was possible, having been registered the occurrence of cracks from the corners of the devices towards the side facet, probably due to cumulative shear tension arising from polishing and laser exposure, which were probably aggravated by thermal shock upon substrate removal from the hot KOH.

For comparison, the same device was fabricated using SCA uniform mesh (laser scan filling parallel to a given direction and perpendicular to the polarization), the same writing velocity and $\epsilon = 52.5\,nJ$ per pulse. No cracks were verified either after fabrication or after etching completion. Profilometer scanning resulted in a determined RMS 127 nm bottom roughness. This roughness was improved by thermal annealing at 1250 °C for 10 h, resulting in a 94 % decrease in RMS roughness. The conclusions show that uniform scanning is sufficient for etching from the surface if scans are sufficiently packed together (in the case, separated of 2 µm).

For μPIV characterization, two OSCERs with accesses and two OSCERs without accesses were fabricated, using the SCA uniform mesh with $\delta = 4\,\mu m$; one of each pair was etched with KOH and the other with HF. Etching saturation and strong tapering effect were observed for access separations of $\Lambda = 500\,\mu m$, when the scanning direction was orthogonal to the etching diffusion direction, hindering embedded fabrication. Top etching was achieved after 20 h with KOH and 60 min with HF, with resulting bottom RMS roughness (waviness) thrice (twice) as large when KOH is used.

The finished devices were experimentally tested with μPIV, and the results were processed with a home-made routine for central streamline detection and least square fitting with a function suggested in literature. The experimental strain rate shows order of magnitude agreement with literature values. The impact of experimental mid-plane measurement uncertainty is assessed as a strain-rate deviation of ≈ 10 %, and the presence of sporadic bubbles and foam shows even greater maximum contribution of ≈ 20 %. The final hypothesis for the fluctuations are the presence of the quantified roughness, and the multi-uniform size reduction to one half relatively to the reference OSCER.

Chapter 5

Concluding remarks and future work

The present work concerns the application of selective femtosecond laser induced etching to the fabrication of devices for applications in microfluidics. The straight microfluidic channel is studied as a starting point for understanding the etching dynamics under different etching configurations, and followed by a comparative fabrication of an optimized shape extensional rheometer.

Microfluidic channels were fabricated at different writing velocities, writing depths, energies per laser pulse, and spacing between laser scans, with the objective of optimizing the etching rate with KOH, while ensuring integrity of the produced structures. The assessment of the low influence of the first two parameters is understood as the possibility for (almost entirely) embedded fabrication in silica substrates, in a range of velocities which is compatible with time-efficient investigation. The preponderant contribution of the latter two parameters is quantified by means of a theoretical first-neighbour interaction model between laser scans to yield the threshold fluence per unit length for optical damage in the material, within the interval of 5 to 8 $\mathrm{J\,m^{-1}}$. This model is applied to two different slicing schemes, one characterized by a constant scans spacing and another by a geometric chirp rate near walls. The qualitative comparison, established by means of transverse section visualization, conveyed the low influence of the various graded meshes in the reduction of section corner rounding, while demonstrating that no direct correlation could be drawn from the relation between neighbouring scan distance, and etch rate. The resulting etching, faster by the walls of the graded micro-channels, was deemed inadequate for the establishment of one etch rate for each scheme, culminating in the abandonment of this approach due to the lack of practical advantages.

The group dynamics of the etchant penetration through the zones modified by each individual laser scans holds a strong dependence on the used etchant and on the etching scheme adopted. With the side-etched fabricated channels for parameter optimization, it was verified that larger values of unitary pulse energy resulted in retarded etching

saturation, its maximization constituting a priority whenever below the damage threshold fluence. These dynamics are different from those of access-aided etched micro-channels, which are divided into two mechanisms depending on the etchant.

Micro-channels with variable separations between accesses of up to 1 mm were etched with HF and KOH. Etching with HF in the mid access which revealed the constitution of an etching wavefront spread through the channel width penetrating the inter-access region, with the former, and the almost exclusive etching through the laser scans immediately below the etchant entry point, while using the latter.

For HF, the interplay between selectivity and access separation determined that the tapering effect is more pronounced from a separation of 200 µm onwards. The redimension of etchant entry area to span the full width of the channel translated into high fidelity fabrication within the tested range of $500-1500$µm, reducing by a factor of ten the number of accesses required for embedded fabrications, with significantly lesser tapering effect.

μPIV validation of results predicted analytically, and confirmed numerically is seen to depend on more than simply the possibility of accurate three-dimensional micro-machining. Namely, the accumulation of debris, tracer particle clogging the channels, and weak PDMS to glass bonding are reported to severely encumber practicality of smaller (10.20 µm wide) channels in broader microfluidic applications. The only tested micro-channel was fabricated by top-etching with HF, with a cross section of 50 µm, and was tested in μPIV, showing agreement with numerical and analytic predictions. The experimental verification of the comparison between the fluid flow performance of KOH and HF etched devices was limited by the PDMS debonding from the substrate; it is therefore left as future work the optimization of this process, as well as of the process for piercing holes and aligning with the microstructure, perhaps with a motorized linear xy stage for PDMS positioning.

The transition between a simple device, whose fabrication is possible within a few stage command lines, to a complex device such as an OSCER, demands software capabilities in terms of external geometry importing, and automatic slicing. Albeit these possibilities are made real with the fabrication software available, obstacles raised by importing certain STL files, and the impossibility of controlling polarization expeditiously between laser scans, entailed the development of a home-made Python module. The contour-mimicking hatching scheme was applied with smaller energy and scan spacing in the outermost contours versus their global uniformity, having been verified the existence of polishing-induced stress, aggravated by thermal contrast between KOH etching temperature and room temperature, with smaller prevalence whenever both spacing and pulse energy are lowered next to the edges of the device. This method is yet to be tested for embedded fabrication, where it is predicted to be of relevance.

The OSCER device was also fabricated with a uniform hatching and slicing with optimized scan separation of 2 µm, allowing adequate etchant penetration and recirculation, and absence of thermal shock damage (albeit polishing was not performed). The high selectivity of KOH becomes disfavourable in the issue of surface roughness at the bottom of the OSCER, which is improved by thermal annealing in viscous-flow dominated temperature regimes. The impact of roughness as a source of fluid flow disturbance is yet to be fully understood, as the intended comparison between etchant performance was not successful, due to improper bonding of the HF-etched cross-slot. Nonetheless, the device etched with KOH was characterized in a regime of Reynolds number between 1 and 100, having been found discrepancies between determined velocity profiles, and results presented in the literature, in the region far from the constant strain rate region, and agreement in determined strain rates. Future work in varying the interrogation areas' shapes, and monitoring of the velocity profile in the development region are suggested for accuracy improvement. Furthermore, the unsuccessful tests with the HF OSCER, conjointly with the possibility for further annealing of the KOH OSCER, represent future work pointing towards further clarification of the reported fluid flow.

In-depth fabrication of these devices, by regular software-aided slicing, demonstrated the limitations of the simple parallel scan slicing in terms of fast saturation when access separation vector is normal to laser scan vector. It is proposed, based on the experiments, that etching with tuned polarization inwards slicing may be a valid approach for solving this issue, in alternative to two other possibilities, them being writing the same device twice (first with vertical laser scans and horizontal polarization, followed by horizontal laser scans and vertical polarization) and trying another type of polarization, such as circular polarization. These approaches were not pursued in the present thesis, and are left for future work.

The main conclusion is that FLAE is an alternative to traditional microfluidic fabrication methods based on PDMS, allowing monolithic fabrication of complex geometries in a broad range of dimensions.

Appendix A

The microfluidic contraction: from simulations to fabrication

In this appendix, the reader is presented with instructions on how to set up a case in OpenFOAM® from the geometry to the time parameters of the simulation. The `fvSchemes` and `fvSolutions` are only briefly referred to, since this is not an exhaustive description of OpenFOAM® discretization methods.

A.1 Case structuring in OpenFOAM®

The following text describes how code must be structured inside the so-called text folder. Each problem to be numerically solved with OF must have a dedicated folder, referred to as case folder. It is advised to keep the case folder's name clear and short, without spaces and non-alphanumeric characters. Inside this folder, several others must be included, as outlined in Figure A.1.

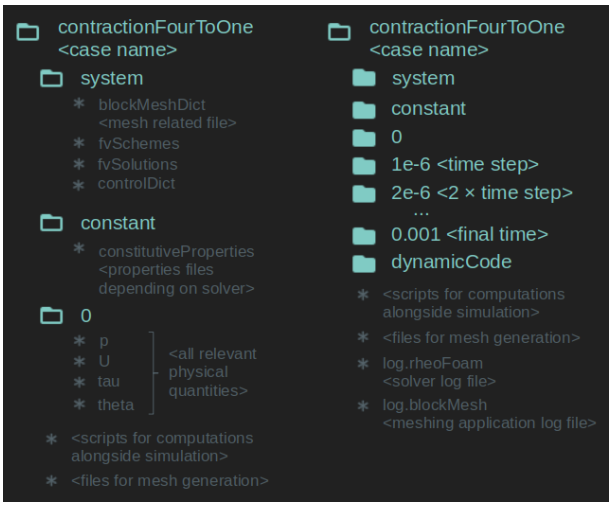

FIGURE A.1: Structure of a typical OF case, prior to (left) and after (right) the numerical simulation.

Regarding the types of files contained in all those directories, the following bullet points apply:

- the folder named '0' is mandatory and contains files with the name of all applicable vector and scalar fields, e.g. pressure and velocity for a laminar flow of a Newtonian fluid, which constitute the problem's initial conditions, specified for all the computational domain.

- the folder named 'system' is also mandatory and contains the information regarding the discretization procedure, the time step and other simulation time-related parameters. Inside this folder, the following files must be present: 'controlDict' (where the parameters for the time evolution of the system are set), a mesh-related file (where the mesh parameters are defined), an 'fvSchemes' file (where the discretization schemes for the terms in the governing differential equations are defined), and an 'fvSolutions' file (where the algorithms for the integrations of those equations must also be customized by the user);

- a folder named 'constant', mandatory as well, which contains all information regarding constitutive properties for the physical modelling of the studied phenomena;

- other files inside the case folder are optional and may include bash scripts (to clean the time directories, run a given solver using several CPU cores in parallel, if needed, or engage post processing procedures) and C++ header and main files with functions which can be called from within OF files;

- the 'dynamicCode' folder is created after the beginning of the simulation and results from the compilation of user defined functions and the solving process itself – including the mesh generation, and is usually of no greater interest for the fluid dynamicist; and

- as an OF solver is called from the terminal to integrate the differential equations and evolve the flow, directories are created in succession inside the case folder, named with the time at which the several fields inside them are sampled; this becomes evident in the right side of Figure A.1.

A.2 Preprocessing: generating the mesh and setting the simulation

Generating a mesh can be a hard work; fortunately, there is a wide variety of resources available, some of them as open-source, such as `cfMesh` or `snappyHexMeshGrid`, which allow mesh generation from a given input file, such as a stereolithography (STL) file.

Some of the simulations carried out assume a two-dimensional (2D) flow; as will be seen, there are specific keywords that OF must receive from the programmer, in order to assume this specific type of simulation. What we mean by 2D is the following: if one of the characteristic dimensions of the computational mesh is much larger (at least ten times larger [7]) than the other two, so that the flow quantities can be assumed translation invariant in that direction.

The condition above can be stated in an equivalent manner: supposing a cut is made in the computational domain perpendicularly to that 'neutral' direction, it must be exactly the same, no matter where that cut occurs. This means that a 2D domain can be seen as a ribbon, like in Figure A.2, to the left, where the two empty faces represent the fact that they much more apart than any other two faces.

However, in this introductory case, the discretization of the physical system was done by hand, that is, the mesh was entirely set by the user. When that is the case, the meshing file inside the 'system' folder is named `blockMeshDict`. It consists of a set of dictionaries, each identified by a keyword, and cascaded in a way that information in the bottom may be computed using information in the top, so the user must be aware of any fault in this sequence.

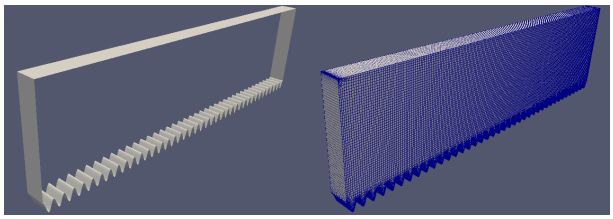

Figure A.2: Mesh generation (right) from a ribbon (left), using the `cartesian2DMesh` utility of `cfMesh`.

The first attempts of a simulation showed physically unreasonable results, which were interpreted as a consequence of incorrect block definition (see Section A.2.0.2) and solved accordingly.

An intermediate alternative was pursued, in order to be able to refine the mesh in two different high resolution demanding areas of the three cells described above: the wall of the channel, if applicable, and the corner regions, i.e., those near the edges contained in the plane of the lateral walls of the short channel and in the one of the plane separation between channels. The reason for this special care is due to the precision required, considering that those are regions where the larger gradients are expected to occur, which requires higher spatial resolution to be resolved with higher accuracy.

However, this intermediate approach was rapidly dismissed and replaced by a simpler formulation with the same four cells, but with hybrid gradings in the mesh. This feature complements the `simpleGrading` by allowing the user to define, for each of the Cartesian directions and within the same cell, regions with different grading behaviours – this was exploited for the generation of a mesh expansion from the wall towards the center of either

the bottom or top large channel cells, followed by a uniform grading and a contraction towards the prolongation of the short channel inside the large one.

A.2.0.1 Determination of the mesh parameter expansion ratio

Besides simple, linear meshes, it is possible to construct graded meshes. In order to define them, it is necessary to specify the direction of expansion and the expansion ratio ζ, that is, the ratio of the lengths of the final cell to the initial cell.

Knowing that the expansion is performed by means of a geometric series of the cell lengths, it is straightforward to define a relation between the ratio r of that progression and both the total length and that of the largest cell. Therefore, it is possible to determine the progression's ratio – from which the expansion ratio follows – from the sum of the lengths of all cells, and the starting cell length.

These calculations are carried out in Appendix B; since it is not possible to solve the analytic expression for the desired ratio, it was necessary to implement a bisection method to be called from inside the `blockMeshDict` file.

A.2.0.2 Anatomy of a `blockMeshDict` file

The reader may find, in the Listings below, a code sequence adapted from the case of the microfuluidic contraction. General aspects of the syntax involve ending every statement with a semicolon – beware of this when troubleshooting! – and precede comments by two slashes, as typically used in the C++ programming language.

When creating a `blockMeshDict`, the first step consists in defining relevant geometrical parameters, which may be important in further scripting for an optimization routine, for the verification of the device's sensitivity to variations in each of its geometrical features, or even for the sake of running a series of case studies with related topology but different applications. These definitions are presented between lines 4 and 8 of Listing A.1 and must be given by declaring the variable, leaving space and assigning the value, ending in a semicolon – in fact, just like every other entry in the dictionary. Eventual calculations requiring previous definitions are initiated with the keyword `#calc` followed by a string, between inverted commas, containing the mathematical expression to be computed, with all variables being preceded by a bash dollar sign ($).

As a side note, some keywords already have a definite meaning in OF, such as `scale`, which is interpreted as the conversion factor between the dimensions given and the meter. As such, these keywords should not be used as variable names.

After defining characteristic lengths for the problem, relevant vertices must be defined. After declaring the dictionary with the keyword `vertices`, the position vectors of all points are then listed, each being a 3-tuple of coordinates, and encapsulated between brackets.

This concludes the geometry parametrization and sets the key points which delimit the volume of interest for the simulation. In Figure 2.7, the vertices' numbering is shown, along with the axis orientation for the definition of coordinates (the centre of the frame is the centre of the face containing vertices 0, 3, 8, and 11).

```
scale 1e-6; //microns

// Geometry Parametrization
  L_large 1000;                  // half of the length large channel
  H_large 100;                   // half of the width large channel
  D       25;                      // half of the height
  Dneg    #calc "-$D";
  Llneg   #calc "-$L_large";       // skipping some variables...

vertices
(
  (  0.0       $Hsneg   $Dneg  ) // 0
  (  $L_short  $Hsneg   $Dneg  ) // 1
                  // ...
  ( $Llneg     $Hsneg     $D   )   // 18
  ( $Llneg     $H_short   $D   )   // 19
);
```

Listing A.1: Variable definitions in a `blockMeshDict` file.

After defining the volume, the discretization follows. Every mesh can be divided into its building blocks, quite literally. Considering the discussion in Section A.2, the mesh was divided into regions I to IV shown in Figure 2.7: one containing the narrow channel and the other three constituting the wider one. The idea behind delimiting blocks is to separate perfectly the nature of all their faces whenever required – for instance, if one block's face contains both a part of solid wall and a part which is not a wall, then it must be subdivided so that the ambiguity is solved.

These regions were discretized differently considering the direction. First, note that, because this is a 2D simulation, only one cell will be used along z, the 'special' direction. Now, along the direction of flow (x), different precisions are required considering the proximity to the interfacial region. For that reason, all regions were discretized with a simple grading expanding from the contraction plane towards the inlet (regions I to III) or outlet (region IV).

Perpendicularly to the direction of flow, along y, all regions were discretized with three types of grading, starting with a compressed mesh, next to the side wall of the shorter channel and to its projection onto the larger one, expanding further towards the center

of each region, where the grading is uniform, and finally, compressing again towards the other lateral wall. The ratio of the number of cells in each subregion was set equal to the ratio in lengths; these parameters can be interpreted from Listing A.2 (lines 7 and 8).

Finally, the reader should note, in lines 17 to 29, how to call a routine defined in another file, written in C++ , in order to compute a quantity to assign to a variable in the `blockMeshDict`. The `#codeInclude` directive allows for the importing of all functions from within the header file where the auxiliary functions are, whereas the `#codeOptions` are set to include (`-I`) the case's directory in the list of paths that OF will search the header file in. Finally, the code itself includes calling an external function, and assigning the output to the variable `erxs`, while outputting the value to the command line via the `Info` directive. The contents of the file `getDelta.H` are explained in Appendix B.

```
// Mesh parameters
Nxl 200;    // nmb of cells along x in each block of large ch.
Nyl 30;     // nmb of cells along y in each block of large ch.
Nys 30;     // must be equal to Nyl (consistency!)
Nz  1;      // 2D simulation

Nratio 0.2; // ratio of the channel cells to use compressed mesh (2*0.2)
Lratio 0.2; // ratio of channel length (idem)

dx 1;       // mesh size in the region near the corners

Nrem  #calc "1. - 2 * $Nratio";        // remainder of the channel N cells
Lrem  #calc "1. - 2 * $Lratio";        // remainder of the channel length
Ncys  #calc "$Nratio * $Nys";          // nmb cells compressed mesh (short ch.)
Lcys  #calc "$Lratio * 2 * $H_short";  // respective length

erxs    // expansion ratio for x direction short ch.
  #codeStream {
    codeInclude #{
      #include "getDelta.H"
  #};
  codeOptions #{
      -I$(FOAM_CASE)
  #};
  code #{
    os << getDelta($Nxs, $L_short, $dx) << endl;
    Info << "\n\nExp. ratio in x (short ch.): " << getDelta($Nxs, $L_short, $dx) <<
    endl;
  #};
  };
```

```
crxs #calc "1./$erxs"; // compression ratio x direction short ch.
```

Listing A.2: The parameters of the mesh for the contraction geometry.

In order to define the geometry from the vertices, one must use the `blocks` directive, and list sequentially all the blocks contained in the geometry. OF provides several types of block topologies, detailed in [95]; this example, however, uses the simplest one which fits the design, the hexahedral block, or simply put, the parallelepiped. In adding a block to the list, it is necessary to specify the type of block, here with the keyword `hex`, followed by the vertices of the block, identified by their number in the `vertices` dictionary. For reference, the definition of two of the four blocks for the contraction simulation is represented in Listing A.3, with the numbers in the comments referring to the regions in Figure 2.7.

The ordering of the vertices is not random; instead, using the example of a parallelepipedic cell, vertices at the same z coordinate are to be specified first, counter-clockwise, followed by the remaining vertices, starting with the one above the first vertex in the list.

After the vertices' numbers, the operator must define the number of cells for the discretization of the block, in all three directions, with a 3-tuple. Finally, it is necessary to instruct OF how to distribute the lengths of the block amongst the available cells in all directions. For that, usually one uses the directive `simpleGrading`, encapsulating three elements, one for each of the directions. For instance, lines 4 to 9 of Listing A.3 direct the `blockMesh` utility to use a mesh with the following properties:

- an expansion ratio of `erxs` for the x direction – recall that means the `Nxs`$^{\text{th}}$ cell will be `erxs` larger than the first in that direction;
- an expansion ratio of `ery` in a fraction (`Lratio`) region of the channel using a fraction (`Nratio`) of the number of cells in y, followed by a uniform mesh (analogous meanings of `Lrem` and `Nrem`), and then an expansion region with ration `cry`; and
- a completely uniform mesh in the z direction, which is irrelevant since only one cell was defined in that direction, but would be of interest in a three-dimensional simulation.

```
blocks
(
  hex (  0  1  2  3  8  9 10 11 ) ( $Nxs $Nys $Nz ) // short channel (IV)
4 simpleGrading
  (
    $erxs
    (($Lratio $Nratio $ery) ($Lrem $Nrem 1) ($Lratio $Nratio $cry))
    1
```

```
  )

  hex ( 17  3  6  7 19 11 14 15 ) ( $Nxl $Nyl $Nz ) // top large (I)
  simpleGrading
  (
    $crxl
    (($Lratio $Nratio $eryl) ($Lrem $Nrem 1) ($Lratio $Nratio $cryl))
    1
  )
);
```

Listing A.3: Definition of blocks from the corresponding vertices (Figure 2.7).

The final step is the definition of the boundary of the computational domain. For that, one must use the vertices' numbers to define all the limiting faces, making it possible to name them for future reference in setting the boundary conditions. The vertices must be enumerated in the order prescribed by the screwdriver rule in order to have the normal vector pointing outwards.

It is possible to declare a set of faces as a single region; that means that OF will treat all those faces as they were one, and apply the same boundary condition to them. As such, it is advised to only create a boundary region with multiple faces if they do share the boundary condition, as is the case of the three faces corresponding to all blocks which constitute the large channel in the contraction – see, for instance, the definition of the inlet in Listing A.4.

Similarly to the keywords and types of blocks available in OF, so can all the types of boundaries be found in official documentation [95]. We present only three of those types: the `patch`, which is used for locations like inlets and outlets, which are associated to the movement of fluid toward or from the device; the `wall`, which is used for almost all the MF channels' walls; and the `empty` type, which is a special type exclusively for two-dimensional simulations. The `empty` keyword informs the solver that the boundaries thus classified are in fact of an extent which is larger than the separation in between them (again, this is specific of a 2D simulation).

```
boundary (
  inlet {
    type patch;
  faces (
    ( 16  4 12 18 ) // bottom
    ( 16 18 19 17 ) // middle
    (  7 17 19 15 ) // top
  );
  }
```

```
    wall_lipdown {      // top side wall of the large channel
      type wall;
      faces (
        (  5  0  8 13 )
      );
    }

    frontAndBack {
    type empty;
    faces (
        (  3  2  1  0 )   // below (short channel)
      (  7  6  3 17 )   // below (long channel)
        ( 17  3  0 16 )
      ( 16  0  5  4 )
    );
    }
);
```

Listing A.4: Definition of the geometric boundaries of the contraction.

A.2.0.3 Setting the `controlDict` file

The `controlDict` file contains a number of entries which help define the time parameters of the simulation. The most important entries are `startTime` (time at which the simulation starts, tipically set to 0), the `endTime` (time at which the simulation terminates), and `deltaT` (the simulation time step).

The simulation time step is rather important in order to achieve good accuracy, and avoid non-physical results and even to assure that the simulations will run until `endTime` without any overflows. At this point, it is useful to remind the definition of the Courant dimensionless number, $\mathrm{Co} = \Delta t/\Delta x|\mathbf{U}|$, which takes a different value for every computational FVC. The temporal and spatial stability of the numerical simulations require that $\mathrm{Co} < 1$ everywhere in the computational domain.

An estimate for the maximum value of $|\mathbf{U}|$ in the computational mesh can be given by an order of magnitude above the average inlet velocity, which is fixed, $\mathbf{U}_{\mathrm{in}} = 0.1\,\mathrm{m\,s^{-1}}\mathbf{e_x}$. The minimum value of Δx is, by the structuring of the case, at the corners, and set to be $\Delta x = 1\,\mu\mathrm{m}$. With these estimates, and the requirement for Co, it is mandatory that $\Delta t < 10^{-6}$. In order to operate with a safety margin, the time step for the simulation is chosen to be two orders of magnitude below.

The last important keywords in the `controlDict` are `writeControl` and `writeInterval`: they control whenever the user intends to record the simulation data into files, instead

of just continuing the simulation. There are many options for the `writeControl`, but the most common are `timeStep` (data is written every `writeInterval` time steps) and `runTime` (data is written at simulation times multiple of the `writeInterval`).

Finally, the user should know that C++ code can be added to the `controlDict` file, in order to monitor the simulation in real time. An example is found on the 4:1 contraction tutorial available in `rheoFoam`, on which these simulations are partly based, where the vortex length is computed in real time by accessing the mesh whenever the operator demands so (again, the control of when these calculations are executed is performed via the `writeControl` and `writeInterval` keywords. Alternatively, of course, those computations can be performed *a posteriori*, but it is advised to keep an eye on certain flow quantities in order to avoid wasting time in ill posed problems.

A.3 Fabrication and characterization of a contraction

Having been simulated the planar microfluidic contraction in Chapter 2, it is of interest to fabricate such a device. Given the longer etching times expected for a planar device with large aspect ratios, it was decided to fabricate a 3D device, consisting of a length of 2 mm for each of its sides, a constant height of 5 µm and a small channel width of 50 µm (the large channel width is four times as large). Surface ablation was ensured in the end of the writing process. The fabrication parameters were $\epsilon = 30\,\mathrm{nJ}$ per pulse, $\delta = 4\,\mu\mathrm{m}$, and $v_\mathrm{w} = 500\,\mu\mathrm{m\,s^{-1}}$.

After 20 h of etching with KOH, the device was characterized with profilometer scans. Here, we point out an important difference between scanning the device alongside the laser scans, and orthogonally to the laser scans. Since the tip of the profilometer has a size comparable to the laser scan spacing and to the induced voxels, there is the possibility that the measured roughness spatial spectral components are not well determined whenever the device is scanned alongside laser scans. Uncertainty in measuring direction coupled with the aforementioned comparable length scales between measuring device and structure can cause the superposition of several laser-related irregularities.

The experimental μPIV results for this device are not shown. As will be seen, PDMS debonding was a problem throughout the experimental trials, and severely limited the possibilities of expedited μPIV tests, since rebonding without a clean-room environment was insufficient for further applications.

Appendix B

Computation of graded meshes using `blockMeshDict`

In this appendix, expressions are derived for the implementation of automated mesh creation in OF and in the fabrication of MF channels, by solving problems involving sums of terms in geometric progressions, either analytically or numerically. These problems are contextualized in the OF picture, by referencing the cases in which they helped the mesh creation and pre-processing.

B.1 Determination of the ratio of a geometric progression

Let us suppose the sum of terms in a geometric progression, with a ratio $0 < r < 1$, starting term l_M and final term $l_m = l_M r^{N-1}$, adding up to a defined total real number L. Considering that there are N terms in the geometric series, and manipulating the expression for the sum of terms, follows

$$\frac{L}{l_m} = \frac{r^{-N} - 1}{r^{-1} - 1}, \tag{B.1}$$

which allows to determine r for given N, l_m and L.

In practice, however, the solution must be sought using a numerical method for root finding, since an explicit formula can not be derived. When evaluating the denominator $1-r$ for r sufficiently close to one, division by zero may be a problem, while exponentiating r to a very large negative number can easily fall off the machine's representation window. For that reason, Equation B.1 may be rewritten and, upon taking logarithms in both sides, one can define

$$f_{l_m,L,N}(r) = \log\left(\frac{L}{l_m} + \frac{1}{r^{-1} - 1}\right) + N \log r + \log(r^{-1} - 1). \tag{B.2}$$

The method used for the numerical determination of the root of f in the interval $]0, 1[$ was the bisection method. This method may be explained as follows: from two initial guesses for r, say, a and b, we may compute $f(a)$ and $f(b)$ as defined above, and the method proceeds if, and only if, their signs are opposite.

The algorithm then proceeds to bisect the interval $[a, b]$, by finding the middle point c, and checks if there is a sign inversion in each of the subintervals $[a, c]$ and $[c, b]$, thereby determining where may the root of f be found (which is guaranteed by the intermediate value theorem, provided f satisfies properties concerning continuity, the proof of which we base in the physical argument that, from an initial and final term, and having only a certain number of terms at disposal, the total 'length' – if we regard the individual terms as little steps – is perfectly determined once the ratio r is known).

It is instructive to look at Listing B.1, in order to understand how to structure code to be later called from within an OF file (the call itself is found in Listing A.2).

```
using namespace Foam;
#include<bits/stdc++.h>
#include <cmath>

#define EPSILON 0.00001 //tolerance for root finding

double FuncForRatio(double r, int N, double coef) {
  double den = ((1./r) -1. );
  double y = N * std::log(r) + std::log(den) + std::log( coef + 1./den );

  //problems for "large" N (smaller than machine precision)
  //double y = ( (std::pow(r, -N) - 1.) / den - coef);

  return y;
}

// Main routine for the bisection method
double BisectForRatio(double a, double b, int N, double coef) {
  if (func(a, N, coef) * func(b, N, coef) >= 0) {
    cout << "You have not assumed right a and b\n";
    return 0.;
  }

  double c = a;
  while ((b-a) >= EPSILON) {
    c = (a+b)/2; // find middle point

    if (FuncForRatio(c, N, coef) == 0.0) // middle point is root?
      break;
```

```
    else if (FuncForRatio(c, N, coef)*FuncForRatio(a, N, coef) < 0)
      b = c;
    else
      a = c;
  }
  return c;
}

// Called from blockMeshDict
double getZeta(int N, double L, double lmin) {
  double coef = L/lmin;

  if (N * lmin >= L) { // too many cells or too small length
    cout << "Inconsistent number of cells and specified lmin\n";
    return 0.;
  }

  double a = EPSILON, b = 1. - EPSILON;  // initial values assumed
  return std::pow( BisectForRatio(a, b, N, coef), 1.-N );
}
```

Listing B.1: Abbreviated contents of the file getZeta.H for the implementation of a simple bisection after log conformation of the equation relating mesh parameters to the OF grading expansion ratio (cf. page U-153 of [95]).

Firstly, note the existence of the parameter `EPSILON`, which represents the degree of accuracy for the root determined with the algorithm. The first function implements the equation to solve, Equation B.2. This was done due to the possibility of obtaining very small numbers, compared to the machine epsilon, when computing r^N for a 'large' number of cells or for 'small' values of r, such as those which start the bisection loop – for reference, ϵ and $1-\epsilon$, where ϵ is the tolerance defined for the break of the loop. The second function corresponds to the implementation of a typical bisection method.

The third function parses the arguments from the `blockMeshDict` file and performs one additional check before initiating the bisection. If the number of cells is such that even the limiting case of a progression, starting from l_{min} and with $r = 1$ spans more than the length L, then no solution of the equation will be found, because there is no expansion factor causes the total cell length to match the required length.

After finding the progression's ratio r, the expansion ratio,

$$\zeta = \frac{l_M}{l_m}, \tag{B.3}$$

can be computed using $\zeta = r^{1-N}$, which is always greater than 1.

In this work, the method outlined above is used in the construction of a mesh for the 4-to-1 2D contraction studied in Section 2.2.3. There, the mesh resolution in the most problematic corner regions is predetermined, in order to add robustness to the numerical method, as well as the total length of each of the regions, imposed by the geometry one wishes to study, and the number of cells desired, in order to control the computational time, which quickly scales with the total number of cells. OF provides the graded meshing possibility, in which cell lengths are increased by means of a geometrical progression, hence the relevance of the problem discussed in this section.

B.2 Determination of the number of cells

Bearing in mind the scenario in the previous section, let us now suppose that the given parameters are now l_m, l_M, and L, and that we wish to determine the number of terms in the geometric series. This is a much less troublesome problem, since we can relate N to l_m, l_M and r, by using

$$N = \log_r \left(\frac{l_m}{l_M} \right) + 1, \tag{B.4}$$

whereas r can be determined by substituting the expression above for N in the one for the sum of terms, and rearranging the result, which gives

$$r = \frac{1 - l_M/L}{1 - l_m/L}. \tag{B.5}$$

Since there are closed forms for the value of N, what is left to answer the question is to either round the value of N to the nearest integer, or to determine its floor or ceil, in order to obtain an integer number of terms. The consequence of this last option is to, respectively, obtain an effective total sum L_{eff} which is either smaller than or larger than L – in any case, the difference is upper bounded by a half of l_M, which is negligible in the sensible assumption that $l_M/L \ll 1$.

This reasoning was useful in the study of the buried channel described in Chapter 3. For the directions transverse to that of the flow (for symmetry reasons, y and z were equivalent), it was decided to specify the resolution of the mesh near the walls and in the centre of the channel, as well as the length of the expansion region – recall that an expansion towards the center was followed by uniform mesh, and by a contraction with a reciprocal ratio towards the other wall. The total number of cells in the uniform region was not predetermined, and was computed *a posteriori* with the consideration that cells in that region would have the same size as the largest cell in the expansion region.

The implementation in C++ of the closed form expression derived above presents no difficulty other than the possibility of using an array to convey all details which may be relevant for post-processing from this geometry.

In Listing B.2, we implement the correction to the expansion length and the effective value of the expansion coefficient required by OF, keeping l_m constant. In order to do so, we simply use the handy expression

$$\sum_{i=M}^{N} r^i = \frac{1 - r^{N-M+1}}{1 - r}, \tag{B.6}$$

along with the consideration that the largest term in the sum is obtainable from the first one, which we wish to keep, and from both N and r, which one computes with Equations B.4 and B.5, respectively. The variables most useful for further manipulation are the number of elements in the series, `N`, the actual total sum of terms, `LeCorr` (due to the truncation/rounding error) and the ratio between last and first term in the progression, `zetaExp`.

When trying to pass more than one variable to the `blockMeshDict`, it useful to populate an array and return the respective pointer. This is performed in Listing B.2, in line 3, where the array is declared by allocating memory to it (a simple declaration does not suffice because it would then become a variable only in the stack of the function, and removed afterwards). The `malloc` instruction allocates memory, and must be cast as a pointer to a `double`, which is done by writing `(double*)`.

The array `out` is populated in lines 12 to 14 and the pointer is returned in line 16.

```
double* ExpUniConData( double L, double lmin, double lmax ) {

    double *out = (double*) malloc(3*sizeof(double))

    double ratio = ( 1. - lmax/L ) / ( 1. - lmin/L );  // 0 < ratio << 1
    double N = round ( std::log(lmin/lmax) / std::log(ratio) + 1 );

    double LmaxEff = lmin * std::pow(ratio, 1.-N);
    double zetaExp = LmaxEff / lmin;                  // zetaExp > 1
    double LeCorr = lmin * (1. - std::pow(ratio, -N))/(1. - 1./ratio);

    out[0] = N;
    out[1] = LeCorr;
    out[2] = zetaExp;

    return out;
```

```
}
```

Listing B.2: Implementation of the equations of this subsection, with three variables, which characterize the grading, populating the output array.

In the `blockMeshDict` file, an example of a call is given below, (the structure of a call is explained in Section A.2.0.2), with an array that can be accessed. After the variables are assigned, the memory that was reserved by the `malloc` can, and should be freed with the directive `free`.

```
#codeStream {
  // ...
  code #{

    double* meshDataY = ExpUniConData($wExp, $Lcory, $Lmidy);

    os << "Ncy "     << meshDataY[0] << ";" << endl;
    os << "LyCorr "  << meshDataY[1] << ";" << endl;
    os << "ery "     << meshDataY[2] << ";" << endl;

    free(meshDataY);
  #};
  };
```

Listing B.3: Accessing the array variables through the `blockMeshDict` and freeing up the memory.

B.3 Expansion followed by uniform mesh

Now, let us assume a sum of N_e terms in a geometric progression, the first of which is l_m and the last being l_M, as in the previous sections. Further, assume that, to this sum L_e, is added $L_u = N_u \times l_M$, resulting in the quantity L. Supposing that L, L_e, l_m are all known, as is the quantity $N = N_e + N_u$, we wish to determine N_u.

By expressing l_M as a function of L_u and N_u, and plucking into B.5 – noting that L must be replaced by L_e –, one may then insert the expression for r in B.4, finally resulting in

$$N_e = \log_{\frac{1-L_u/(N_u L_e)}{1-l_m/L_e}} \left(\frac{l_m N_u}{L_u} \right) + 1. \tag{B.7}$$

Upon recognising that $N_e = N - N_u$, again the bisection method can be used to determine the value of N_u. For that, we define again a function whose root one wishes to compute,

$$f_{l_m,N,L_e,L_u}(N_u) = (N - N_u - 1) - \frac{\log\left(l_m N_u / L_u\right)}{\log\left(\frac{1-L_u/(N_u L_e)}{1-l_m/L_e}\right)}, \tag{B.8}$$

where the base in the logarithm was changed to e. The conditions to be used as the initial guesses are as follows.

First, we note that the base of the logarithm may not be a negative number: while that is automatically assured for the denominator, it must be verified that $\frac{L_u}{N_u L_e} < 1$, which imposes a lower bound for N_u. Additionally, the same base may not be unity, which requires that $L_u/N_u \neq l_m$. In fact, if equality holds, it means $l_M = l_m$, so the ratio of the progression is unity (which corresponds to a very special scenario). In fact, the requirement is that $l_M > l_m$, which provides an upper bound for N_u. Further, it is reasonable to assume that N_u is also upper bounded by N, the total number of terms. The constraints (or initial guesses) for the bisection method are, thus,

$$\begin{aligned} N_u &> \frac{L_u}{L_e} \\ N_u &< \min\left\{\frac{L_u}{l_m}, N\right\}. \end{aligned} \tag{B.9}$$

The problem described arose in the context of the buried channel simulation case, this time for the meshing in the direction of the flow, and the constrain of the total number of cells was introduced to bound the time cost of the simulation, at least for the first ones, in order to gain sensitivity to the time step, at the exchange of freeing the parameter l_M, which is not critical if the length of the expansion region is reasonably chosen in terms of the total length of the channel. The resolution with the bisection method was entirely analogous, in formal aspect, to that presented in Listing B.1, with the exception that the `FuncForRatio` and `BisectForRatio` functions had to be altered to implement the expression in Equation B.8, as suggested.

Finally, it should be noted that, since the value obtained for N_u must be an integer, there is an operation of truncation or rounding involved before an output is given. For that reason, the effective sum of all terms may not equal the predetermined length. If one wishes to, nonetheless, maintain that length, it is possible to apply a correction to the length of the mesh in the uniform region, so that the total length is conserved.

The solution presented above can generate a problem in terms of the cell's aspect ratio. When running the `checkMesh` command, the user executes a series of verifications on the mesh, one of those concerning the ratio between the cells' dimensions in all directions.

It is advised to keep this AR below 10; for that, a refinement to the code above can be implemented, if one considers the same geometry (total length L divided into a cell expansion of size N_e followed by uniform mesh of size N_u, imposing that the largest cell length in the expansion is repeated N_u times in the uniform region), but keeping l_m and l_M decided by the user.

Under these conditions, one arrives at another function to find the zero of,

$$f_{l_m,l_M,N,N_e}(N_e) = \frac{L}{l_m} - (N - N_e)\zeta + \frac{1 - \zeta^{N_e/(N_e-1)}}{1 - \zeta^{1/(Ne-1)}}. \tag{B.10}$$

Again using the same procedure and truncation to integer methods described above, the solution can be found with another bisection method, and the mesh generation can be automated, while respecting basic principles to guarantee stability in the numeric simulations.

Bibliography

[1] Bureau Internationale des Poids et Mesures. Les unités de mesure: le si. URL: https://www.bipm.org/fr/measurement-units/ (visited on 07/20/2019).

[2] G. Whitesides. The origins and the future of microfluidics. *Nature*, 442(7101):368–373, July 2006. DOI: 10.1038/nature05058. URL: http://dx.doi.org/10.1038%5C%5C%2Fnature05058.
State-of-the-art of microfluidics, written elegantly by a specialist on the field.

[3] J.-W. Shangguan, Y. Liu, J.-B. Pan, B.-Y. Xu, J.-J. Xu, and H.-Y. Chen. Microfluidic pdms on paper (pop) devices. *Lab Chip*, 17:120–127, 1, 2017. DOI: 10.1039/C6LC01250G. URL: http://dx.doi.org/10.1039/C6LC01250G.

[4] V. Sahore M. Sonker R. Knob and A. Woolley. Integrated electrokinetically driven microfluidic devices with pH-mediated solid-phase extraction coupled to microchip electrophoresis for preterm birth biomarkers. *Electrophoresis*, 38(13-14):1743–1754, April 2017. DOI: 10.1002/elps.201700054. URL: https://doi.org/10.1002/elps.201700054.

[5] Mordor Intelligence. Global microfluidics market - growth, trends, and forecast (2019 - 2024). URL: https://research.mordorintelligence.com/reports/microfluidics-market (visited on 10/01/2019).

[6] C. Li, M. Boban, S. Snyder, P. Sai S. Kobaku, G. Kwon, G. Mehta, and A. Tuteja. Paper-based surfaces with extreme wettabilities for novel, open-channel microfluidic devices. *Advanced Functional Materials*, 26(33):6121–6131, 2016. DOI: 10.1002/adfm.201601821. eprint: https://onlinelibrary.wiley.com/doi/pdf/10.1002/adfm.201601821. URL: https://onlinelibrary.wiley.com/doi/abs/10.1002/adfm.201601821.

[7] S. Haward, M. Oliveira, M. Alves, and G. McKinley. Optimized cross-slot flow geometry for microfluidic extensional rheometry. *Physical Review Letters*, 109(12), September 2012. DOI: 10.1103/physrevlett.109.128301. URL: https://doi.org/10.1103/physrevlett.109.128301.

[8] S. Bazaz, N. Kashaninejad, S. Azadi, K. Patel, M. Asadnia, D. Jin, and M. Warkiani. Rapid softlithography using 3d-printed molds. *Advanced Materials Technologies*:1900425, August 2019. DOI: 10.1002/admt.201900425. URL: https://doi.org/10.1002/admt.201900425.

[9] M. Abdelgawad, M. Watson, E. Young, J. Mudrik, M. Ungrin, and A. Wheeler. Soft lithography: masters on demand. *Lab on a Chip*, 8(8):1379, 2008. DOI: 10.1039/b804050h. URL: https://doi.org/10.1039/b804050h.

[10] A. Grimes, D. Breslauer, M. Long, J. Pegan, L. Lee, and M. Khine. Shrinky-dink microfluidics: rapid generation of deep and rounded patterns. *Lab Chip*, 8(1):170–172, 2008. DOI: 10.1039/b711622e. URL: https://doi.org/10.1039/b711622e. Definitely a different use for Shrinky Dinks, a recommended secondary read for its originality.

[11] Pennsylvania State University. Standard operating procedures of tools in quattrone nanofabrication facility – bonding methods. URL: https://www.seas.upenn.edu/~nanosop/Bonding_Methods.htm (visited on 05/12/2018).

[12] P. Sousa, F. Pinho, M. Oliveira, and M. Alves. Purely elastic flow instabilities in microscale cross-slot devices. *Soft Matter*, 11(45):8856–8862, 2015. DOI: 10.1039/c5sm01298h. URL: https://doi.org/10.1039/c5sm01298h.

[13] P. Salipante, S. Hudson, J. Schmidt, and J. Wright. Microparticle tracking velocimetry as a tool for microfluidic flow measurements. *Experiments in Fluids*, 58(7), June 2017. DOI: 10.1007/s00348-017-2362-6. URL: https://doi.org/10.1007/s00348-017-2362-6.

[14] K. Håkansson. Online determination of anisotropy during cellulose nanofibril assembly in a flow focusing device. *RSC Advances*, 5(24):18601–18608, 2015. DOI: 10.1039/c4ra12285b. URL: https://doi.org/10.1039/c4ra12285b.

[15] S. Haward, A. Jaishankar, M. Oliveira, M. Alves, and G. McKinley. Extensional flow of hyaluronic acid solutions in an optimized microfluidic cross-slot device. *Biomicrofluidics*, 7(4):044108, July 2013. DOI: 10.1063/1.4816708. URL: https://doi.org/10.1063/1.4816708.

[16] W. Schmidt, D. Quosdorf, S. Siewert, U. Hinze, B. Chichkov, M. Brede, A. Leder, R. Guthoff, and K.-P. Schmitz. Micro particle-image-velocimetry for characterization of a micro-mechanical valve in a glaucoma implant. *Biomedical Engineering / Biomedizinische Technik*, 57(SI-1 Track-S), January 2012. DOI: 10.1515/bmt-2012-4296. URL: https://doi.org/10.1515/bmt-2012-4296.

[17] Y. Xia and G. Whitesides. Soft lithography. *Annual Review of Materials Science*, 28(1):153–184, August 1998. DOI: 10.1146/annurev.matsci.28.1.153. URL: https://doi.org/10.1146/annurev.matsci.28.1.153.

[18] N. Nguyen. Micromixers based on molecular diffusion. In *Micromixers*, pages 163–194. Elsevier, 2012. DOI: 10.1016/b978-1-4377-3520-8.00005-x. URL: https://doi.org/10.1016/b978-1-4377-3520-8.00005-x.

[19] F. Sasoglu, A. Bohl, and B. Layton. Design and microfabrication of a high-aspect-ratio PDMS microbeam array for parallel nanonewton force measurement and protein printing. *Journal of Micromechanics and Microengineering*, 17(3):623–632, February 2007. DOI: 10.1088/0960-1317/17/3/027. URL: https://doi.org/10.1088/0960-1317/17/3/027.

[20] L. Aoun, P. Weiss, A. Laborde, B. Ducommun, V. Lobjois, and C. Vieu. Microdevice arrays of high aspect ratio poly(dimethylsiloxane) pillars for the investigation of multicellular tumour spheroid mechanical properties. *Lab Chip*, 14(13):2344–2353, 2014. DOI: 10.1039/c4lc00197d. URL: https://doi.org/10.1039/c4lc00197d.

[21] M. Li, J. Glawe, H. Green, D. Mills, M. McShane, and B. Gale. Effect of high-aspect-ratio microstructures on cell growth and attachment. In *1st Annual International IEEE-EMBS Special Topic Conference on Microtechnologies in Medicine and Biology. Proceedings (Cat. No.00EX451)*. IEEE. DOI: 10.1109/mmb.2000.893841. URL: https://doi.org/10.1109/mmb.2000.893841.

[22] A. Shields, B. Fiser, B. Evans, M. Falvo, S. Washburn, and R. Superfine. Biomimetic cilia arrays generate simultaneous pumping and mixing regimes. *Proceedings of the National Academy of Sciences*, 107(36):15670–15675, August 2010. DOI: 10.1073/pnas.1005127107. URL: https://doi.org/10.1073/pnas.1005127107.

[23] S. Martínez-Aranda, F. Galindo-Rosales, and L. Campo-Deaño. Complex flow dynamics around 3d microbot prototypes. *Soft Matter*, 12(8):2334–2347, 2016. DOI: 10.1039/c5sm02422f. URL: https://doi.org/10.1039/c5sm02422f.

[24] Z. Liu and Don L. DeVoe. Micromechanism fabrication using silicon fusion bonding. *Robotics and Computer-Integrated Manufacturing*, 17(1):131–137, 2001. ISSN: 0736-5845. DOI: https://doi.org/10.1016/S0736-5845(00)00046-6. URL: http://www.sciencedirect.com/science/article/pii/S0736584500000466. 10th International Conference on Flexible Automation and Intelligent.

[25] T. Rogers and J. Kowal. Selection of glass, anodic bonding conditions and material compatibility for silicon-glass capacitive sensors. *Sensors and Actuators A: Physical*, 46(1):113–120, 1995. ISSN: 0924-4247. DOI: https://doi.org/10.1016/0924-4247(94)00872-F. URL: http://www.sciencedirect.com/science/article/pii/092442479400872F.

[26] H. Wu, B. Huang, and R. Zare. Construction of microfluidic chips using polydimethylsiloxane for adhesive bonding. *Lab on a Chip*, 5(12):1393, 2005. DOI: 10.1039/b510494g. URL: https://doi.org/10.1039/b510494g.

[27] S. Satyanarayana, R. Karnik, and A. Majumdar. Stamp-and-stick room-temperature bonding technique for microdevices. *Journal of Microelectromechanical Systems*, 14(2):392–399, April 2005. DOI: 10.1109/jmems.2004.839334. URL: https://doi.org/10.1109/jmems.2004.839334.

[28] L. Shiroma, M. Piazzetta, G. Duarte-Junior, W. Coltro, E. Carrilho, A. Gobbi, and R. Lima. Self-regenerating and hybrid irreversible/reversible PDMS microfluidic devices. *Scientific Reports*, 6(1), May 2016. DOI: 10.1038/srep26032. URL: https://doi.org/10.1038/srep26032.

[29] O. Svelto. *Principles of Lasers*. Springer US, 2010. DOI: 10.1007/978-1-4419-1302-9. URL: https://doi.org/10.1007/978-1-4419-1302-9.

[30] J. Ye and S. T. Cundiff, editors. *Femtosecond Optical Frequency Comb: principle, operation, and applications*. Kluwer Academic Publishers, 2005. DOI: 10.1007/b102450. URL: https://doi.org/10.1007/b102450.

[31] D. Strickland and G. Mourou. Compression of amplified chirped optical pulses. *Optics Communications*, 56(3):219–221, 1985. ISSN: 0030-4018. DOI: https://doi.org/10.1016/0030-4018(85)90120-8. URL: http://www.sciencedirect.com/science/article/pii/0030401885901208.

[32] I. Coddington, N. Newbury, and W. Swann. Dual-comb spectroscopy. *Optica*, 3(4):414–426, April 2016. DOI: 10.1364/OPTICA.3.000414. URL: http://www.osapublishing.org/optica/abstract.cfm?URI=optica-3-4-414.

[33] G. Cerullo R. Osellame and R. Ramponi (Eds.) *Femtosecond Laser Micromachining – Photonic and Microfluidic Devices in Transparent Materials*. Springer, May 2012.

[34] Y. Cheng and K. Sugioka. *Femtosecond Laser 3D Micromachining for Microfluidic and Optofluidic Applications*. Springer series in applied sciences and technology. Springer, London, 2014. DOI: https://doi.org/10.1007/978-1-4471-5541-6.

[35] T. Hänsch. Nobel lecture: passion for precision. *Rev. Mod. Phys.*, 78:1297–1309, 4, November 2006. DOI: 10.1103/RevModPhys.78.1297. URL: https://link.aps.org/doi/10.1103/RevModPhys.78.1297.

[36] N. Ashcroft and N. Mermin. *Solid State Physics*. Saunders College Publishing (Harcourt College Publishers), 1976.

[37] A. Haug. *Theoretical Solid State Physics in two volumes (vol. I)*, volume 36 of *International Series of Monographs in Natural Philosophy*. Pergamon Press, 1972.

[38] M. Watanabe, H. Sun, S. Juodkazis, T. Takahashi, S. Matsuo, Y. Suzuki, J. Nishii, and H. Misawa. Three-dimensional optical data storage in vitreous silica. *Japanese Journal of Applied Physics*, 37(12B):L1527, 1998. URL: http://stacks.iop.org/1347-4065/37/i=12B/a=L1527.

[39] E. Glezer and E. Mazur. Ultrafast-laser driven micro-explosions in transparent materials. *Applied Physics Letters*, 71:882–884, August 1997. DOI: 10.1063/1.119677.

[40] G. New. *Introduction to Nonlinear Optics*. Cambridge University Press, 2011. DOI: 10.1017/CBO9780511975851.
Intuitive first contact with nonlinear optics, skipping ultimate formalism for better or worse.

[41] V. Stankevič and G. Račiukaitis. Formation of rectangular channels in fused silica by laser-induced chemical etching. *Lithuanian Journal of Physics*, 54(3), October 2014. DOI: 10.3952/physics.v54i3.2952. URL: https://doi.org/10.3952/physics.v54i3.2952.

[42] A. Marcinkevičius, S. Juodkazis, M. Watanabe, M. Miwa, S. Matsuo, H. Misawa, and J. Nishii. Femtosecond laser-assisted three-dimensional microfabrication in silica. *Opt. Lett.*, 26(5):277–279, March 2001. DOI: 10.1364/OL.26.000277. URL: http://ol.osa.org/abstract.cfm?URI=ol-26-5-277.
The article which started the FLAE technique is of interest for comparison for current work.

[43] L. Fernandes. *Birefringence and Bragg grating control in femtosecond laser written optical circuits*. eng. PhD thesis, Faculdade de Ciências da Universidade do Porto, 2012, page 158.

[44] L. Fernandes, J. Grenier, P. Herman, J. Aitchison, and P. Marques. Femtosecond laser writing of waveguide retarders in fused silica for polarization control in optical circuits. *Opt. Express*, 19(19):18294–18301, September 2011. DOI: 10.1364/OE.19.018294. URL: http://www.opticsexpress.org/abstract.cfm?URI=oe-19-19-18294.

[45] A. Yariv and P. Yeh. *Optical waves in crystals: propagation and control of laser radiation*, volume XI of *Wiley series in pure and applied optics*. John Wiley, 1984.
Very straight-to-the-point introductory text for crystal optics.

[46] H. Zhang, S. Eaton, and P. Herman. Single-step writing of bragg grating waveguides in fused silica with an externally modulated femtosecond fiber laser. *Opt. Lett.*, 32(17):2559–2561, September 2007. DOI: 10.1364/OL.32.002559. URL: http://ol.osa.org/abstract.cfm?URI=ol-32-17-2559.

[47] J. Maia. *FemtoEtch – Femtosecond Laser Micromachining and Applications in Microfluidics and Optofluidics*. Master's thesis, Faculdade de Ciências da Universidade do Porto, 2016.
The text on which my own work is partly based, a recommended read.

[48] K. Itoh, W. Watanabe, S. Nolte, and C. Schaffer. Ultrafast processes for bulk modification of transparent materials. *MRS bulletin*, 31, August 2006.
Pioneer work on the categorization, with references, of the three types of silica with non-linear radiation interactions.

[49] K. Kawakami and M. Pikal. Calorimetric investigation of the structural relaxation of amorphous materials: evaluating validity of the methodologies. *Journal of Pharmaceutical Sciences*, 94(5):948–965, 2005. ISSN: 0022-3549. DOI: https://doi.org/10.1002/jps.20298. URL: http://www.sciencedirect.com/science/article/pii/S0022354916317609.
Interesting contextualization of parameters characterizing glassy phase transitions.

[50] S. Kiyama, S. Matsuo, S. Hashimoto, and Y. Morihira. Examination of etching agent and etching mechanism on femotosecond laser microfabrication of channels inside vitreous silica substrates. *The Journal of Physical Chemistry C*, 113(27):11560–11566, 2009. DOI: 10.1021/jp900915r. URL: https://doi.org/10.1021/jp900915r.

[51] A. Agarwal and M. Tomozawa. Correlation of silica glass properties with the infrared spectra. *Journal of Non-Crystalline Solids*, 209(1):166–174, 1997. ISSN: 0022-3093. DOI: https://doi.org/10.1016/S0022-3093(96)00542-X. URL: http://www.sciencedirect.com/science/article/pii/S002230939600542X.

[52] A. Agarwal, K. Davis, and M. Tomozawa. A simple ir spectroscopic method for determining fictive temperature of silica glasses. *Journal of Non-Crystalline Solids*, 185(1):191–198, 1995. ISSN: 0022-3093. DOI: https://doi.org/10.1016/0022-3093(94)00676-8. URL: http://www.sciencedirect.com/science/article/pii/0022309394006768.

[53] D. Hand and P. Russell. Photoinduced refractive-index changes in germanosilicate fibers. *Opt. Lett.*, 15(2):102–104, January 1990. DOI: 10.1364/OL.15.000102. URL: http://ol.osa.org/abstract.cfm?URI=ol-15-2-102.

[54] Y. Bellouard, E. Barthel, A. A. Said, M. Dugan, and P. Bado. Scanning thermal microscopy and raman analysis of bulk fused silica exposed to low-energy femtosecond laser pulses. *Opt. Express*, 16(24):19520–19534, November 2008. DOI: 10.1364/OE.16.019520. URL: http://www.opticsexpress.org/abstract.cfm?URI=oe-16-24-19520.

[55] B. Poumellec, P. Niay, M. Douay, and J. Bayon. The uv-induced refractive index grating in ge:sio2 preforms: additional cw experiments and the macroscopic origin of the change in index. *Journal of Physics D: Applied Physics*, 29(7):1842, 1996. URL: http://stacks.iop.org/0022-3727/29/i=7/a=019.

[56] C. Hnatovsky, R. Taylor, E. Simova, P. Rajeev, D. Rayner, V. Bhardwaj, and P. Corkum. Fabrication of microchannels in glass using focused femtosecond laser radiation and selective chemical etching. *Applied Physics A*, 84(1-2):47–61, April 2006. DOI: 10.1007/s00339-006-3590-4. URL: https://doi.org/10.1007/s00339-006-3590-4.

[57] C. Ross, D. MacLachlan, D. Choudhury, and R. Thomson. Optimisation of ultrafast laser assisted etching in fused silica. *Optics Express*, 26(19):24343, September 2018. DOI: 10.1364/oe.26.024343. URL: https://doi.org/10.1364/oe.26.024343.
Very pertinent comparison article, further exploring variations in e.g. repetition rate for a comprehensive study of HF vs KOH.

[58] F. Galindo-Rosales, M. Oliveira, and M. Alves. Optimized cross-slot microdevices for homogeneous extension. *RSC Adv.*, 4:7799–7804, 15, 2014. DOI: 10.1039/C3RA47230B. URL: http://dx.doi.org/10.1039/C3RA47230B.

[59] J. Maia, V. Amorim, D. Alexandre, and P. Marques. Real-time optical monitoring of etching reaction of microfluidic channel fabricated by femtosecond laser direct writing. *Journal of Lightwave Technology*, 35(11):2291–2298, June 2017. ISSN: 0733-8724. DOI: 10.1109/JLT.2017.2678604.

[60] M. Born and E. Wolf. *Principles of Optics*. Cambridge University Press, 7th edition, 1999.
The ultimate Optics' book, with all classical subjects covered formally, albeit not didactically.

[61] L. Fernandes, J. Grenier, P. Herman, J. Aitchison, and P. Marques. Stress induced birefringence tuning in femtosecond laser fabricated waveguides in fused silica. *Opt. Express*, 20(22):24103–24114, October 2012. DOI: 10.1364/OE.20.024103. URL: http://www.opticsexpress.org/abstract.cfm?URI=oe-20-22-24103.

[62] Y. Li and S. Qu. Water-assisted femtosecond laser ablation for fabricating three-dimensional microfluidic chips. *Current Applied Physics*, 13(7):1292–1295, 2013. ISSN: 1567-1739. DOI: https://doi.org/10.1016/j.cap.2013.03.028. URL: http://www.sciencedirect.com/science/article/pii/S1567173913001508.

[63] Y. Li, K. Itoh, W. Watanabe, K. Yamada, D. Kuroda, J. Nishii, and Y. Jiang. Three-dimensional hole drilling of silica glass from the rear surface with femtosecond laser pulses. *Opt. Lett.*, 26(23):1912–1914, December 2001. DOI: 10.1364/OL.26.001912. URL: http://ol.osa.org/abstract.cfm?URI=ol-26-23-1912.
Pionnering work in liquid assisted femtosecond laser etching.

[64] E. Hasselbrink K. Ke and A. Hunt. Rapidly prototyped three-dimensional nanofluidic channel networks in glass substrates. *Analytical Chemistry*, 77(16):5083–5088, 2005. DOI: 10.1021/ac0505167. eprint: https://doi.org/10.1021/ac0505167. URL: https://doi.org/10.1021/ac0505167.
Features the fabrication of a jumper device, alongside other 3D structures.

[65] S. Qu Y. Li and Z. Guo. Fabrication of microfluidic devices in silica glass by water-assisted ablation with femtosecond laser pulses. *Journal of Micromechanics and Microengineering*, 21(7):075008, 2011. URL: http://stacks.iop.org/0960-1317/21/i=7/a=075008.

[66] J. Kaakkunen, M. Silvennoinen, K. Paivasaari, and P. Vahimaa. Water-assisted femtosecond laser pulse ablation of high aspect ratio holes. *Physics Procedia*, 12:89–93, 2011. ISSN: 1875-3892. DOI: https://doi.org/10.1016/j.phpro.2011.03.110. URL: http://www.sciencedirect.com/science/article/pii/S1875389211001891.
Lasers in Manufacturing 2011 - Proceedings of the Sixth International WLT Conference on Lasers in Manufacturing.

[67] D. Hwang, T. Choi, and C. Grigoropoulos. Liquid-assisted femtosecond laser drilling of straight and three-dimensional microchannels in glass. *Applied Physics A*, 79(3):605–612, August 2004. ISSN: 1432-0630. DOI: 10.1007/s00339-004-2547-8. URL: https://doi.org/10.1007/s00339-004-2547-8.

[68] A. Ben-Yakar, R. Byer, A. Harkin, J. Ashmore, H. Stone, M. Shen, and E. Mazur. Morphology of femtosecond-laser-ablated borosilicate glass surfaces. *Applied Physics Letters*, 83(15):3030–3032, 2003. DOI: 10.1063/1.1619560. eprint: https://doi.org/10.1063/1.1619560. URL: https://doi.org/10.1063/1.1619560.

[69] R. An, Y. Li, Y. Dou, D. Liu, H. Yang, and Q. Gong. Water-assisted drilling of microfluidic chambers inside silica glass with femtosecond laser pulses. *Applied Physics A*, 83(1):27–29, April 2006. ISSN: 1432-0630. DOI: 10.1007/s00339-005-3456-1. URL: https://doi.org/10.1007/s00339-005-3456-1.

[70] F. He, Y. Liao, J. Lin, J. Song, L. Qiao, Y. Cheng, and K. Sugioka. Femtosecond laser fabrication of monolithically integrated microfluidic sensors in glass. *Sensors*, 14(10):19402–19440, October 2014. DOI: 10.3390/s141019402. URL: https://doi.org/10.3390/s141019402.
Very comprehensive state-of-the-art for femtosecond laser micro-machining.

[71] *SCA micromachining software manual V2.1*. English. Workshop of Photonics. 2018. 104 pages.

[72] V. Maselli, R. Osellame, G. Cerullo, R. Ramponi, P. Laporta, L. Magagnin, and P. Cavallotti. Fabrication of long microchannels with circular cross section using astigmatically shaped femtosecond laser pulses and chemical etching. *Applied Physics Letters*, 88(19):191107, May 2006. DOI: 10.1063/1.2203335. URL: https://doi.org/10.1063/1.2203335.

[73] V. Amorim. *Fabrication of Integrated Optical Devices in Fused Silica by Femtosecond Laser Direct Writing*. Master's thesis, Faculdade de Ciências da Universidade do Porto, 2016.

[74] Logitech. Consumable product catalogue. URL: https://logitech.uk.com/wp-content/uploads/2016/07/consumables_brochure_april2.pdf (visited on 05/19/2019).

[75] F. Moukalled, L. Mangani, and M. Darwish. *The Finite Volume Method in Computational Fluid Dynamics: An Advanced Introduction with OpenFOAM® and Matlab®*. October 2015. ISBN: 978-3-319-16873-9. DOI: 10.1007/978-3-319-16874-6.
Very important reference for starting with OpenFOAM®, written with special care in terms of background knowledge.

[76] A. Kulkarni. *Non-Equispaced Fast Fourier Transforms in Turbulence Simulation*. Master's thesis, University of Massachusetts Amherst, 2017.

[77] H. Bruus. *Theoretical microfluidics*. English. Oxford University Press, United States, 2007. ISBN: 978-0-19-923509-4.
A pure and simple formal treaty on the subject; if related to microfluidics, it is explained in here.

[78] M. Raffel, C. Willert, and J. Kompenhans. *Particle Image Velocimetry: A Practical Guide*. January 1998. DOI: 10.1007/978-3-662-03637-2.

[79] L. Campo-Deaño, F. Galindo-Rosales, F. Pinho, M. Alves, and M. Oliveira. Flow of low viscosity boger fluids through a microfluidic hyperbolic contraction. *Journal of Non-Newtonian Fluid Mechanics*, 166(21-22):1286–1296, November 2011. DOI: 10.1016/j.jnnfm.2011.08.006. URL: https://doi.org/10.1016/j.jnnfm.2011.08.006.

[80] T. Niraula, S. Shah, S. Chatterjee, and A. Bhattarai. Effect of methanol on the surface tension and viscosity of sodiumdodecyl sulfate (SDS) in aqueous medium at 298.15–323.15k. *Karbala International Journal of Modern Science*, 4(1):26–34, March 2018. DOI: 10.1016/j.kijoms.2017.10.004. URL: https://doi.org/10.1016/j.kijoms.2017.10.004.

[81] F. White. *Viscous Fluid Flow*. McGraw-Hill Education, 3rd edition, 2006. Simple first approach to simple viscous flows in several pipe geometries.

[82] T. Fratrović and E. Marusic-Paloka. Boundary perturbation for the dirichlet boundary value problem. *Rad Hrvat. Akad. Znan. Umjet. Mat. Znan.*, 20:109–123, January 2016.

[83] Y. Zheng. Lecture no. 37 (wed., nov 27) – poisson equation in a rectangle. http://www.math.psu.edu/yzheng/m597k/m597kLVI8.pdf(accessed in January 2019). Part of the Lecture notes for MATH 597K 'Introduction to Applied Mathematics' graduate course at Pennsylvania State University.

[84] F. White. *Fluid mechanics*. McGraw-Hill Education (India), 7th edition, 2017. A treaty on Fluid Mechanics, while being balanced in difficulty anf formalism.

[85] R. Taylor, C. Hnatovsky, E. Simova, P. Rajeev, D. Rayner, and P. Corkum. Femtosecond laser erasing and rewriting of self-organized planar nanocracks in fused silica glass. *Optics Letters*, 32(19):2888, September 2007. DOI: 10.1364/ol.32.002888. URL: https://doi.org/10.1364/ol.32.002888.

[86] C. Hnatovsky, R. Taylor, E. Simova, V. Bhardwaj, D. Rayner, and P. Corkum. Polarization-selective etching in femtosecond laser-assisted microfluidic channel fabrication in fused silica. *Optics Letters*, 30(14):1867, July 2005. DOI: 10.1364/ol.30.001867. URL: https://doi.org/10.1364/ol.30.001867.

[87] Stephen Ho, Mi Li Ng, Shane M. Eaton, Peter R. Herman, and J. Stewart Aitchison. Single and multi-scan femtosecond laser writing for selective chemical etching of glass micro-channels. In *2007 Conference on Lasers and Electro-Optics (CLEO)*. IEEE, May 2007. DOI: 10.1109/cleo.2007.4452785. URL: https://doi.org/10.1109/cleo.2007.4452785.

[88] C. Barton. Bentleyottmann sweep-line implementation (for finding all intersections in a set of line segments). URL: https://github.com/ideasman42/isect_segments-bentley_ottmann (visited on 06/12/2018).

[89] K. Sugioka and Y. Cheng. Integrated microchips for biological analysis fabricated by femtosecond laser direct writing. *MRS Bulletin*, 36(12):1020–1027, December 2011. DOI: 10.1557/mrs.2011.274. URL: https://doi.org/10.1557/mrs.2011.274.

[90] F. He, J. Lin, and Y. Cheng. Fabrication of hollow optical waveguides in fused silica by three-dimensional femtosecond laser micromachining. *Applied Physics B*, 105(2):379–384, May 2011. DOI: 10.1007/s00340-011-4520-5. URL: https://doi.org/10.1007/s00340-011-4520-5.

[91] Y. Wang and A. M. Shkel. Study on surface roughness improvement of fused quartz after thermal and chemical post-processing. In *2016 IEEE International Symposium on Inertial Sensors and Systems*. IEEE, February 2016. DOI: 10.1109/isiss.2016.7435555. URL: https://doi.org/10.1109/isiss.2016.7435555.

[92] W. Mullins. Flattening of a nearly plane solid surface due to capillarity. *Journal of Applied Physics*, 30(1):77–83, January 1959. DOI: 10.1063/1.1734979. URL: https://doi.org/10.1063/1.1734979.

[93] K. Osawa, H. Inoue, A. Masuno, K. Katayama, Y. Zhang, F. Utsuno, Y. Sugahara, K. Koya, A. Fujinoki, H. Tawarayama, and H. Kawazoe. Smoothing of surface of silica glass by heat treatment in wet atmosphere. *Journal of Applied Physics*, 109(10):103520, May 2011. DOI: 10.1063/1.3587229. URL: https://doi.org/10.1063/1.3587229.

[94] P. DAntonio, M. Lasalvia, G. Perna, and V. Capozzi. Scale-independent roughness value of cell membranes studied by means of afm technique. *Biochimica et Biophysica Acta (BBA) - Biomembranes*, 1818(12):3141–3148, 2012. ISSN: 0005-2736. DOI: https://doi.org/10.1016/j.bbamem.2012.08.001. URL: http://www.sciencedirect.com/science/article/pii/S0005273612002659.

[95] C. Greenshields. *User Guide Version 6*. English. Version Version 6. The OpenFOAM Foundation. 237 pages. URL: http://foam.sourceforge.net/docs/Guides-a4/OpenFOAMUserGuide-A4.pdf.